Flow and Thermal Management Methods, and High Performance Microvalves for Highly Integrated Microscale Gas Chromatographs

by

Hsueh-Tsung Lu

A dissertation submitted in partial fulfillment
of the requirements for the degree of
Doctor of Philosophy
(Mechanical Engineering)
in the University of Michigan
2021

Doctoral Committee:

Professor Yogesh B. Gianchandani, Co-Chair
Dr. Yutao Qin, Co-Chair
Professor Katsuo Kurabayashi
Professor Kenn Oldham

Hsueh-Tsung Lu

leohtlu@umich.edu

ORCID iD: 0000-0001-6145-6771

© Hsueh-Tsung Lu

2021

To my parents, Tong-Chi and Jui-Feng, and my sister, Chi-Hsuan

Acknowledgements

I would like to express my deepest appreciation to my research advisor, Professor Yogesh Gianchandani, for giving me the opportunity to work with and learn from him. His enthusiasm in research, relentless pursuit of excellence, passion to technology, and vision in research direction have inspired me since the first day. Without his instruction and encouragement, I could not accomplish what I have done in my PhD studies.

I am especially grateful to my mentor Dr. Yutao Qin. I truly admire his critical thinking ability, diligence, and persistence. He listened to me, brainstormed with me, and provided me with valuable suggestions. I always remember how he encouraged and patiently guided me when I had failures, and to me, those were the essentials to my achievements. I would also like to thank my committee members Prof. Katsuo Kurabayashi and Prof. Kenn Oldham. Their valuable feedback and suggestions have polished this research work more than they thought. I also thank the LNF staff for providing such a nice facility for all the researchers, particularly Pilar Herrera-Fierro who has trained me on much equipment.

I genuinely thank everyone who I have had the honors to work with and have helped me in any possible way. Prof. Tao Li gave me guidance on microsystem integration and electronics. Dr. Scott Green gave me suggestions on computational modeling work. Dr. Alex Benken, who I have collaborated with on another two projects, trained me on cleanroom operations and helped me with PCB packaging. He was one of the people who I always enjoyed discussing technical challenges with. Partha, Johnny, and Daniel, who I have collaborated with on the project of wireless pharmaceutical analytical device, taught me a lot on hardware electronics and software. Weilin

and Daniel, who I have collaborated with on the microscale gas chromatography project, have been such nice colleagues and friends. I cannot overstate how much I cherish the opportunities to work with these two. The ups and downs we have been through together were the best memories in my PhD journey. I thank all the other members from our research group and my office mates, including Neeharika, Sajal, Ramprasad, Qisen, Jiqing, Tsenguun, Qu, Hanfei, Andy, Irene, Declan, Zeyu, Adrienne, Tao, Amin, Behnoush, Tal, Stacey, Farzad, Ester, Yi, and Ali.

Finally, and most importantly, I would like to express my most sincere gratitude to my family. My girlfriend, Hsin-To Hung, who decided to accept a job offer in Michigan and to stay with me, has provided me more tremendous moral support than she even realized, especially during the unexpected pandemic outbreak. My parents, Tong-Chi Lu and Jui-Feng Hsu, and my sister, Chi-Hsuan Lu have always supported me wholeheartedly and trusted every decision I made. Their unconditional love and support are the best things that have happened in my life.

Table of Contents

Dedication ii

Acknowledgements iii

List of Figures viii

List of Tables xiv

List of Appendices xv

Abstract xvi

Chapter 1: Introduction 1

1.1 Microscale Gas Chromatography 1

1.2 Progressive Cellular Architecture 3

1.3 Challenges and Requirements of µGC Microvalves 5

1.4 Thermal Management of Monolithic µGC Components 6

1.5 Motivation of This Work 7

1.6 Organization of This Thesis 9

Chapter 2: Monolithic Valve Modules with High Chemical Inertness and Embedded Flow Heating 12

2.1 Introduction 13

2.1.1 Overview of Microvalves 13

2.1.2 Goals 29

2.2 Monolithic Valve Modules – VM1 31

2.2.1 Design and Modeling 31

2.2.2 Fabrication and Assembly.. 40

2.2.3 Experimental Results 42

2.3 Enhanced Monolithic Valve Modules – VM2 49

2.3.1 Design 49

2.3.2 Fabrication and assembly.. 55

2.3.3 Experimental results.. 58

2.4 Discussion and Conclusion 65

Chapter 3: A Flow Management Method For A Microscale Gas Chromatograph Eliminating Sample Inlet Valve 68

3.1 Introduction 69

3.2 Concept Evaluation and System-level Demonstration.. 71

3.2.1 Concept Evaluation.. 71

3.2 2 System-level Demonstration.. 74

3.3 Experimental Results.. 84

3.4 Discussion and Conclusion 88

Chapter 4: Thermal Management of A Highly Integrated Microscale Gas Chromatograph 90

4.1 Introduction 91

4.1.1 Overview and challenges 91

4.1.2 Goals 92

4.2 Design and Modeling 95

4.3 Experimental Results.. 107

4.4 Discussion and Conclusion ... 110

Chapter 5: Conclusions And Future Work ... 113

5.1 Conclusions ... 113

5.2 Future Work ... 117

Appendix A: A Piezoelectric Hybrid Valve with Three-way Control ... 118

A.1 Design ... 119

A.2 Fabrication and Assembly ... 124

A.3 Experimental Results ... 125

A.4 Discussion and Conclusion ... 130

Appendix B: Additional Thermal Modeling Results of Monolithic Microscale Gas Chromatography Components ... 132

References ... 137

List of Figures

Fig. 1.1: (a) Sources of air pollution. (b) General fluidic architecture of a μGC system. 2

Fig. 1.2: A three-cell illustration of the progressive cellular architecture. 4

Fig. 2.1: Piezoelectrically actuated valves with different types of actuators. (a) A valve using PZT stack type actuator [Par08]. (b) A valve using bimorph disk type actuator [Gro15]. 18

Fig. 2.2: (a) An electromagnetically actuated microvalve combined with an external actuator [Ter79]. (b) An electromagnetically actuated microvalve using a micro-coil and a flexible beam [Cap00]. 21

Fig. 2.3: (a) An electrostatic valve with a three-electrode configuration [Rob94]. (b) An electrostatic valve incorporating a hydraulic chamber [Kim08]... 24

Fig. 2.4: Different types of thermally actuated valves. (a) A valve using SMA actuators [Bar12]. (b) A valve using thermopneumatic actuation [Pot12]. (c) A valve using a bimetallic diaphragm actuator [Jer94]. 28

Fig. 2.5: The architecture of the VM1. (a) The 2-valve VM1. The right valve is open, whereas the left valve is closed. (b) The 3-valve VM1. The valve on the right is in the open state, whereas the rest of the valves are in the closed state. (c) Top view of the fluidic die stack of the 2-valve VM1, showing the patterns of the fluidic microchannels and the embedded flow heater and thermistor. (d) Top view of the fluidic die stack of the 3-valve VM1, showing the patterns of the fluidic microchannels and the embedded flow heater and thermistor... 33

Fig. 2.6: The relationship between the distance and the force of the solenoid actuator. The closed state position has a net force exerting downward, whereas the open-state position has a net force exerting upward. 34

Fig. 2.7: The circuit schematic for controlling multiple electromagnetic solenoid actuators....... 35

Fig. 2.8: (a) The geometric model used in the simplified analytical model with 2D heat dissipation. (b) The equivalent thermal circuit of thermal flux transporting from the embedded heater to ambient.. 37

Fig. 2.9: (a) The geometric model and the thermal conductivity values (W/mK) used in the simulation. (b) The temperature distribution of fluidic die stack with a simulated heater power of 1.1 W. Close-up views of the valve inlets are shown in the insets. 39

Fig. 2.10: The pressure distribution along the flow path of the middle valve of the 3-valve VM1. 40

Fig. 2.11: The die stack fabrication process. The valve seats, fluidic microchannels, and through-holes are created by a two-mask sandblasting process. The Ti/Pt layer is patterned while using another mask. Three dies are bonded into a stack to form the fluidic die stack. 41

Fig. 2.12: (a) A photograph of the fluidic die stack of the 2-valve VM1. (b) Final view of the assembled 2-valve VM1. (c) Photographs of the fluidic die stack of the 3-valve VM1 prior to and following the assembly of the valve membrane and soft post. (d) Final view of the assembled 3-valve VM1. 42

Fig. 2.13: The test setup used to characterize the fluidic performance of the valve.................... 43

Fig. 2.14: (a) Flow characteristics for an open microvalve. (b) Leakage characteristics for a closed microvalve.. 44

Fig. 2.15: Dynamic response of the valve. (a) At 0 ms, the light emitting diode was turned on, confirming the passage of electric current. (b) At 90 ms, the plunger started to move. (c) At 120 ms, the plunger reached the end position... 45

Fig. 2.16: The energy and power consumption of the microvalve during heating. The microvalve was heated to and maintained at 75°C under servo control. 46

Fig. 2.17: The test setup of the chemical injection tests. The valve under test was connected to the flow path of a benchtop gas chromatograph (7890A, Agilent Technologies, Inc., Santa Clara, CA, USA). 48

Fig. 2.18: (a) Normalized and shifted peaks for 1-butanol. (b) Normalized and shifted peaks for diethyl methyl phosphonate. 48

Fig. 2.19: (a) The chromatogram of non-polar chemical analytes in Case 3. (b) The chromatogram of polar chemical analytes in Case 3.. 49

Fig. 2.20: (a) The unpredictable thermal deformation of the cured flowable adhesive that creates leakage. (b) The detachment of valve membrane when flow with negative pressure is supplied. 50

Fig. 2.21: The architecture of the VM2. (a) The 2-valve VM2. The right valve is open, whereas the left valve is closed. (b) The 3-valve VM2. The valve on the right is in the open state, whereas the rest of the valves are in the closed state. (c) Top view of the fluidic die stack of the 2-valve VM2, showing the patterns of the fluidic microchannels and the embedded flow heater and thermistor. (d) Top view of the fluidic die stack of the 3-valve VM2, showing the patterns of the fluidic microchannels and the embedded flow heater and thermistor. 52

Fig. 2.22: The equivalent fluidic circuit of the flow path of the VM2. 54

Fig. 2.23: (a) A photograph of the fluidic die stack of the 2-valve VM2. (b) A photograph of the fluidic die stack of the 3-valve VM2. 56

Fig. 2.24: (a) The laser-engraved upper polyimide membrane. (b) The CNC-machined plunger connector. 57

Fig. 2.25: (a) A photograph of the upper housing of the 2-valve VM2. (b) A photograph of the lower housing of the 2-valve VM2. (a) A photograph of the upper housing of the 3-valve VM2. (b) A photograph of the lower housing of the 3-valve VM2. 57

Fig. 2.26: Photographs of the assembled valve modules mounted onto custom PCBs. (a) The 2-valve VM2. (b) The 3-valve VM2. 58

Fig. 2.27: The test setup for evaluating the lifetime of the microvalve. 59

Fig. 2.28: Measured flow rates and temperatures of Microvalve1 in the preliminary lifetime results. (a) The supplied flow was in the positive pressure regime. (b) The supplied flow was in the negative pressure regime 60

Fig. 2.29: Measured flow rates and temperatures of Microvalve2 in the preliminary lifetime results. (a) The supplied flow was in the positive pressure regime. (b) The supplied flow was in the negative pressure regime 60

Fig. 2.30: Measured flow rates and temperatures of Microvalve3 in the preliminary lifetime results. (a) The supplied flow was in the positive pressure regime. (b) The supplied flow was in the negative pressure regime 60

Fig. 2.31: Cycling lifetime test of the microvalve. The sudden change of flow rate at t = 20 minute resulted from an imposed reversal of flow direction. 61

Fig. 2.32: (a) Architecture of MPCA1.0 μGC. (b) A photograph of the MPCA1.0 μGC. 63

Fig. 2.33: (a) The chromatograms generated by the AiPDs before the sample injection, showing the baseline of the signal. (b) The chromatograms generated by the AiPDs in Cell2 and Cell3. (c) The chromatograms generated by the AiPDs after the sample injection, showing the baseline of the signal. 64

Fig. 2.34: The chromatograms produced by the CapDetAs in Cell2 and Cell3. 65

Fig. 3.1: The DEMP peak generated by a FID when a heated microvalve and an unheated COTS valve were tested, respectively. 70

Fig. 3.2: (a) Conventional μGC architecture. (b) Flow management method that circulates the separation flow and replaces the sample inlet valve with a flow restrictor. 72

Fig. 3.3: (a) The test setup of the preliminary experimental evaluation. (b) The transient flow rates measured by FM1. 74

Fig. 3.4: (a) Dividing a single separation pump to two separation pumps. (b) Architecture of the MPCA1.1 μGC. 76

Fig. 3.5: The equivalent fluidic circuit and the flow resistances (kPa/sccm) of different flow paths in Cell3 separation. 78

Fig. 3.6: Portion of outgoing flow versus the flow resistance of the flow restrictor. 79

Fig. 3.7: Illustration of the cross section of the MPCA1 chip. 80

Fig. 3.8: A photograph of the (a) MPCA1 chip and (b) MPCA1.1 μGC. 83

Fig. 3.9: (a) The chromatograms of alkanes generated by the AiPDs in Cell2 and Cell3. (b) The chromatograms of BTEX and phosphonates generated by the AiPDs in Cell2 and Cell3. 87

Fig. 3.10: (a) The chromatograms of alkanes generated by the CapDetAs in Cell2 and Cell3. (b) The chromatograms of alkanes and phosphonates generated by the CapDetBs in Cell2 and Cell3. 87

Fig. 4.1: The 3D illustration of the MPCA1 chip, Ultem1010 substrate, and PCB. 95

Fig. 4.2: (a) The 3D illustration of Preconcentrator1, showing the sorbent chamber and heater pattern. (b) The 3D illustration showing the slits of the column heater. 97

Fig. 4.3: The simulated thermal characteristics of Preconcentrator1 in three different designs. (a) The simulated transient responses. (b) The simulated current consumptions. (c) The simulated temperature distributions after 4 s of heating. 100

Fig. 4.4: The simulated thermal characteristics of Preconcentrator2 in three different designs. (a) The simulated transient responses. (b) The simulated current consumptions. (c) The simulated temperature distributions after 2.5 s of heating. 102

Fig. 4.5: The simulated thermal characteristics of Preconcentrator3 in three different designs. (a) The simulated transient responses. (b) The simulated current consumptions. (c) The simulated temperature distributions after 1 s of heating. 103

Fig. 4.6: The simulated thermal characteristics of Column1 in three different designs. (a) The simulated transient responses. (b) The simulated current consumptions. (c) The simulated temperature distributions after 50 s of heating. 105

Fig. 4.7: The simulated transient responses of (a) Column2 and (b) Column3. 106

Fig. 4.8: The simulated temperature distributions and transient responses of the detectors in (a) the MPCA1 chip, and (b) the MPCA2-A chip. (c) Current consumptions of the detector heaters in the two designs 107

Fig. 4.9: The programmed temperature and heating duration of each component. 108

Fig. 4.10: The temperature distributions and heating ramp rates of Preconcentrator1 after 4 s of heating. (a) The thermography results. (b) The simulated results. (c) The transient thermal responses. 109

Fig. 4.11: The temperature distributions and heating ramp rates of Preconcentrator2 after 2.5 s of heating. (a) The thermography results. (b) The simulated results. (c) The transient thermal responses. 110

Fig. 5.1: A multi-dimensional benchmarking of microvalves in the context of μGC. The minimum desired level for μGC is indicated by the red line. The microvalve module in this work uniquely provides both embedded flow heating capability and superior chemical resistance, while only modestly compromising other metrics. 115

Fig. A.1: The architecture of the microvalve. The flow routing path from different perspective views are shown in the inset below. The top view and bottom view of each component are demonstrated at the right. 120

Fig. A.2: (a) The displacement generated by the bimorph actuator. (b) The waviness of the bimorph actuator. (c) 2D and 1D profile of the surface roughness of the bimorph actuator...... 121

Fig. A.3: (a) 3D demonstration of actuator assembly with a fixed-fixed boundary condition. (b) Analogous 2D demonstration of beam deflection with a fixed-fixed boundary condition. (c) 3D demonstration of actuator assembly with a simply-supported boundary condition. (d) Analogous 2D demonstration of beam deflection with a simply-supported boundary condition................ 123

Fig. A.4: (a) Surface profile of FEP membrane. (b) Surface profile of polyimide membrane... 124

Fig. A.5: Fabrication steps of the silicon fluidic dies (a) Front-side DRIE. (b) Back-side DRIE. 125

Fig. A.6: (a) The fluidic die stack is assembled from lithographically microfabricated silicon dies. (b) Partial assembly of the valve. (c) Final view of assembly. 125

Fig. A.7: The test setup used to characterize the fluidic performance of the valve. 126

Fig. A.8: The circuit schematic for the control of the piezoelectric bimorph actuators. 127

Fig. A.9: (a) Flow rates under various inlet pressure drops. The measurements were done for both outlets. While one port was tested, the other one remained closed. The actuated voltage was 70 V. (b) Leakage flow when the valve was fully closed. The valve was tested up to 10 kPa 128

Fig. A.10: (a) The change of flow rate at different applied voltages. (b) Flow conductance as a function of voltage when tested at a blocking pressure of 6.80 kPa, illustrating hysteresis from the piezoelectric actuator. 128

Fig. A.11: Continuous operation of the microvalve was tested by toggling one port at a period of 45 seconds while maintaining the other port to be closed. The actuation voltage was 80 V. The applied blocking pressure was 5.1 kPa. 129

Fig. A.12: The chromatogram of non-polar chemical analytes. (a) An overall chromatogram of four non-polar chemical analytes under two test cases. (b) Normalized and shifted nonane peak. 130

Fig. B.1: The simulated thermal characteristics of the carrier gas filter in three different designs. (a) The simulated transient responses. (b) The simulated current consumptions. (c) The simulated temperature distributions after 3 s of heating. 133

Fig. B.2: (a) The simulated current consumptions of Column2. (b) The simulated temperature distributions of Column2 after 50 s of heating. 134

Fig. B.3: (a) The simulated current consumptions of Column3. (b) The simulated temperature distributions of Column3 after 50 s of heating. 135

List of Tables

Table 2.1: Performances of different actuation schemes. 29

Table 2.2: The parameters used in the simplified analytical model and the resulting thermal resistances. 37

Table 2.3: The differences between the VM1 and VM2. 53

Table 2.4: Dimensions and calculated flow resistances of all the flow paths............................. 55

Table 2.5: List of 22 tested analytes and their Kovats RI. 64

Table 2.6: Comparison of some gas microvalves. 66

Table 3.1: Estimated flow resistances of all the components within the MPCA1 chip............... 77

Table 3.2: Flow rates through the preconcentrator and the column in each cell. 85

Table 4.1: Constraints and targets of the MPCA1 chip. 94

Table 4.2: Thermal conductivity values of the simulated components in FEA. 99

Table 4.3: Measured and simulated electrical resistances of the on-chip heaters. 99

Table 4.4: Heating power and thermal characteristics of Preconcentrator1 in 4 s. 101

Table 4.5: Heating power and thermal characteristics of Preconcentrator2 in 2.5 s. 101

Table 4.6: Heating power and thermal characteristics of Preconcentrator3 in 1 s. 104

Table 4.7: Heating power and thermal characteristics of Column1 in 50 s. 104

Table 5.1: The original values and scaled values for benchmarking the valves. 115

Table B.1: Heating power and thermal characteristics of the carrier gas filter in 3 s................ 133

Table B.2: Heating power and thermal characteristics of Column2 in 50 s. 134

Table B.3: Heating power and thermal characteristics of Column3 in 50 s. 136

List of Appendices

APPENDIX A: A Piezoelectric Hybrid Valve with Three-way Control.................................. 118

APPENDIX B: Additional Thermal Modeling Results of Monolithic Microscale Gas Chromatography Components 132

Abstract

Microscale gas chromatographs (μGCs) are being investigated and developed for homeland security, defense, and environmental monitoring applications, providing the capability to accumulate, separate, detect, and quantify volatile organic compounds (VOCs) from interferents. Precisely managing gas flow and controlling temperature of each component is essential to μGC advancement. In gas flow management, one fundamental challenge is the need of valves that can ideally provide superior chemical resistance and embedded flow heating. In thermal management, the temperature control of μGC components, including microfabricated preconcentrators, columns, and detectors, is critical. The heating of these components is commonly provided by on-chip joule heaters that are customized for rapid temperature ramping and uniform temperature distribution.

In this research, two methods for gas flow control are investigated. The first method is based upon the high performance microvalve modules. Multi-valve modules that monolithically integrate multiple valves into compact manifolds are designed, fabricated, tested, and ultimately integrated with μGCs. The volume of these multi-valve modules ranges from 23.2 to 32.6 cm^3. The microvalve permits a flow open-close ratio of 3.46×10^3 with open flow conductance of 4.15 sccm/kPa and closed leakage conductance of 0.0012 sccm/kPa. The chemical injection testing results reveal superior chemical resistance of the microvalve and the necessity of the embedded flow heating function. With the embedded flow heating, the microvalve provides virtually no distortion of chromatographic peaks, in stark contrast to a commercial off-the-shelf (unheated) valve that broadens the peaks by 240% or virtually eliminates them. Thorough lifetime tests show

that the time to failure exceeds 480 hours of operation. The multi-valve modules are ultimately integrated with a μGC chip and tested within a system against 22 analytes.

The second method of gas flow control takes the opposite approach of eliminating the use of valves located within the sampling path and the separation path by moving all valves downstream of the detectors and incorporating an additional pump. This approach eliminates the need of valves with embedded flow heating capability and the need for valve materials that do not retain target chemical molecules. A fluidic model is constructed to analyze how undesired flow can be minimized. This flow management method is conceptually validated in a preliminary evaluation, and experimentally implemented in an MPCA1.1 μGC, which demonstrates analysis of various VOCs, including alkanes, aromatics, and phosphonates.

Another fundamental μGC challenge addressed in this dissertation is the thermal management of a highly integrated μGC chip, which combines three preconcentrators, three columns, nine detectors, and a carrier gas filter. With such a high-level of integration, sophisticated thermal management is needed to manage the thermal isolation and crosstalk between elements, while concurrently providing the appropriate level of temperature ramping and heating uniformity for each component. High performance heater designs for all the co-planar components based on their heating requirements and sizes are identified. Based on the finite element model established in this work, the heaters are capable of providing a small temperature variation of <4°C in the preconcentrators and the separation columns, which is critical for the performance of the μGC. The heaters can also provide heating ramp rates of >50 °C/s for the preconcentrators, >1°C/s for the separation columns, and >4 °C/s for the detectors, all meeting the μGC requirements. This thermal management approach can be used in any μGC with substantial monolithic integration.

Chapter 1:

Introduction

1.1 Microscale Gas Chromatography

Gas phase analysis technologies have been developed for various applications such as health care, food analyses, homeland security, and air pollutant sensing (Fig. 1.1a) since 1950s. Three major types of instruments – gas chromatographs (GCs), mass spectrometers, and infrared spectroscopes – have been established since then. Among these instruments, GCs are particularly attractive for detecting and identifying volatile organic compounds (VOCs) in complex backgrounds. However, conventional benchtop GCs are bulky and labor-intensive in operation, which limits their usage in real-time field applications. Microscale gas chromatography (μGC) has been investigated for over 40 years [Ter79]. The rapid development of microfabrication technologies has enabled microfluidic structures to be implemented on chips in centimeter scale and assembled into portable devices, hence opening the path of μGC development.

Typical μGC systems include preconcentrators, separation columns, and detectors (Fig. 1.1b). These components are fluidically connected to provide sample collection and separation. The preconcentrator is a small chamber packed with sorbent materials to adsorb analytes during sampling and thermally desorb analytes during separation [Tia05, Seo12]. The separation column is a relatively long fluidic channel coated with stationary phase on the inner walls to separate analytes depending on its interaction with the stationary phase at the operating temperature [Aga05]. The detector generates an electrical signal response to analytes. Examples of the

detectors include chemicapacitive detectors, microdischarge-based detectors, and chemiresistive detectors [Mls06, Mit08, Ste11].

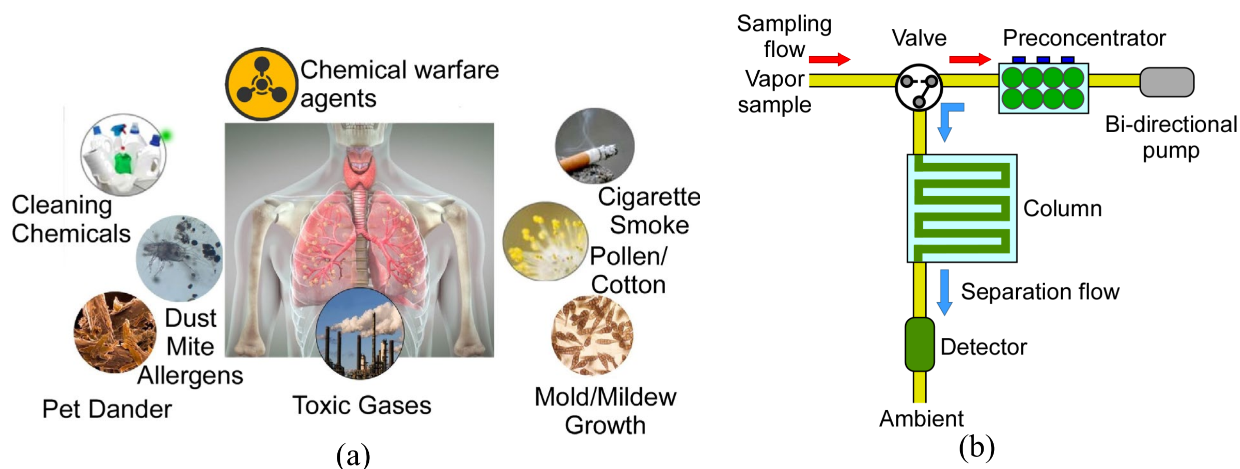

Fig. 1.1: (a) Sources of air pollution. (b) General fluidic architecture of a μGC system.

These μGC components are combined using either hybrid integration or monolithic integration. Hybrid integration has been more common hitherto, where individual components are interconnected by capillary tubing [Gor12, Col14, Gar15, Qin16, Wan18] or fluidic manifolds [Lew06, Kim11, Zho16]. Although hybrid integration has the benefit of simpler fabrication, the inevitable fluidic dead volumes and cold spots, and the assembly complexity prevent it from achieving a high level of integration. Compared to hybrid integration, monolithic integration enables highly-integrated μGC systems that have smaller form factors [Reg18]. Different levels of monolithic design have been reported. Multiple works have integrated two components, such as a column with a preconcentrator [Lia21a], a column with a thermal conductivity detector [Kaa10, Nar13], a column with a photoionization detector (PID) [Akb15], a column with a Fabry-Perot detector [Red13], or a preconcentrator with a thermal injector [Zha19]. A higher level of monolithic integration that incorporates three components, including a preconcentrator, a column, and a detector has also been reported [Bon08, Man11].

The gas flow in μGC systems is generated by pumps and navigated by valves [Lew06, See07, Zam09, Kim11, Gor12, Col14, Gar15, Lee16]. The pumps and valves are usually standalone devices. The pump utilizes actuation mechanisms such as electrostatic actuation, piezoelectric actuation, and thermal transpiration to provide flow to μGC systems [An15, Qin15, San16, Che17]. The valve, which combines the fluidic channel and valve seat with an external actuator, actively control the timing and direction of the flow [Yan04, Hes04, Sub06, Par08, Par09, Eva11]. Evident from the operation, the performance of a μGC system heavily depends on the management of gas flow and temperature in component and system levels.

1.2 Progressive Cellular Architecture

Progressive cellular architecture (PCA) has been reported as a novel μGC architecture intended for analyzing a broad range of analytes while achieving low power consumption [Lia21a]. The PCA comprised of a series of heterogeneous cells, each represents conventional μGC architectures where a single set of preconcentrator and column is utilized (Fig. 1.2). By using a tailored preconcentrator and a separation column in each cell and arranging the cells in a serial and progressive manner, coarse separation of analytes into different cells is achieved during sampling, and subsequently tailored full separation of each cell is completed during separation. Each cell is unexposed or minimally exposed to the VOCs outside its targeted volatility range. Because each cell is tailored for VOCs within a range of volatility, the temperature programming is less intensive and time-consuming, and thus the energy consumption is substantially reduced per measurement cycle when compared with the conventional μGC architecture.

Compared to the conventional μGC architecture (Fig. 1.1b), the PCA has a more complex fluidic architecture that requires proper flow management. In the PCA, the sampling and

separation flow are provided by a bi-directional pump module where two pumps and a three-way valve are incorporated. The timing and direction of the flow are controlled by different sets of valves that are located upstream of the preconcentrators in the sampling path (*i.e.*, sampling microvalve module) and downstream of the detectors in the separation path (*i.e.*, separation microvalve module). In a three-cell implementation, the sampling valve module incorporates two 2-way valves, whereas the separation valve module incorporates three 2-way valves. During sampling, Valve4 is opened whereas Valve1, Valve2, and Valve3 are closed to permit the analytes flowing through Valve4, Preconcentrator3, Preconcentrator2, Preconcentrator1, and the carrier gas filter. During separation, Valve4 is always closed whereas Valve1, Valve2, and Valve3 are sequentially opened, one at a time, to allow separation and analysis in the corresponding cell (*e.g.*, analytes flow through carrier gas filter, Preconcentrator1, Column1, Detector1, and Valve1 during Cell1 separation). Valve5 is normally closed, and only opened when emission of potential reference standard is needed.

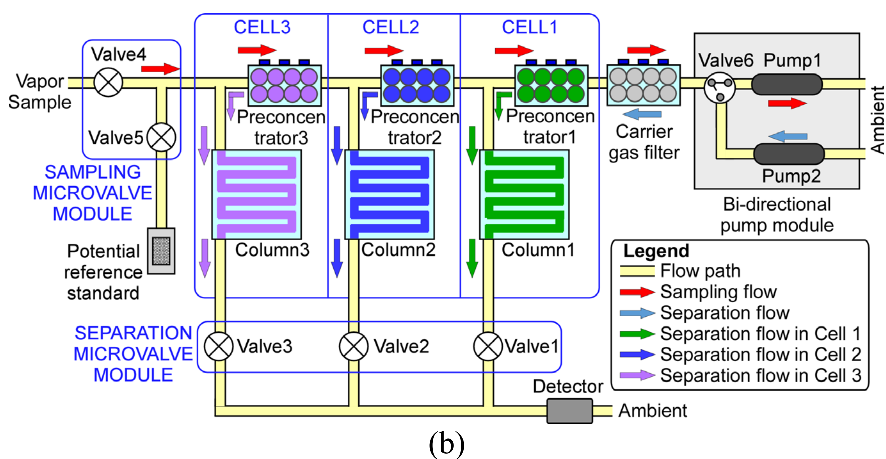

(b)

Fig. 1.2: A three-cell illustration of the progressive cellular architecture.

The flow routing between a sampling path and multiple separation paths is necessary in the PCA. As shown in Fig. 1.2, one optimistic solution is to utilize high performance microvalves to control both the sampling and the separation gas flow. These microvalves presented in the sample

inlet and separation flow paths are thus required to not interfere with the chemical analysis. The challenges and requirements of microvalves intended for μGC applications are described in Sec. 1.3.

1.3 Challenges and Requirements of μGC Microvalves

The microvalve is a critical component for μGC systems as it permits flexible arrangements and operational sequences of μGC components. General requirements of a microvalve include high flow modulation capability, low leakage, low power actuation, high reliability, and manufacturability with the intended application. For μGC applications, the additional requirements include: 1) superior chemical resistance to prevent analyte loss, 2) embedded flow heating in order to reduce surface adsorption of analytes, 3) low dead volume to reduce chromatographic peak distortion, and 4) monolithic integration of multiple valves to reduce overall device volume.

Among all the requirements, the chemical inertness and embedded flow heating are particularly important. Many analytes, such as organophosphorus compounds, pose technical challenges to μGC systems because they are extremely surface-adsorptive and easily retained by the chemically active sites or cold spots on the device inner surfaces [Pop09]. Such surface adsorption, in addition to any dead volume in the flow path, can lead to noticeable peak distortion and broadening effects. Microfabricated and commercial off-the-shelf (COTS) valves have both historically lacked embedded flow heaters, presenting challenges for the analysis of surface-adsorptive chemicals in μGC systems. Therefore, the flow routing in μGC systems would have benefited from the availability of microvalves with high chemical inertness, and embedded flow heating capability.

1.4 Thermal Management of Monolithic µGC Components

Temperature and heating control of µGC components are essential for any highly-integrated µGC system. When components that have different sizes and heating requirements are fabricated within a single chip, thermal management is required to ensure high heating performance of each component and to mitigate the undesired thermal crosstalk among the components. Thermal management mainly includes three aspects: 1) achieve sufficient heating ramp rate for each µGC component, 2) obtain high temperature uniformity within each heated component, and 3) provide thermal isolation among the components. The heating conditions, such as targeted temperatures, heating durations, and heating ramp rates vary significantly from component to component.

In general, a preconcentrator targets a high temperature (of 200-300°C) with a short heating duration (of tens of ms to a few s); a column requires a moderate temperature (of 20-60°C) that may sometimes be ramped up to 100-200°C over a longer duration (of a few minutes); whereas a detector may prefer an isothermal temperature to obtain a steady signal baseline. In addition to the heating ramp rates, uniform temperature distribution within each heated component is desired. Non-uniform temperature distribution can cause problems such as incomplete preconcentrator desorption and peak broadening. To prevent such issues, a small temperature variation across the sorbent area of the preconcentrator (*i.e.*, ideally <5°C) is favored [Lew05]. Because these components possess vastly different sizes and thermal masses, they require specific considerations when conducting the thermal management.

Among the components, thermal isolation is needed to mitigate the thermal crosstalk. This can be achieved by various methods, including using thermally insulating substrates, suspended components, physical cutouts, heatsinks, and forced convection [Bon08, Man11, Col16, Qin16].

Without effective thermal isolation, components can be overheated due to the undesired thermal crosstalk from the heating of a neighboring component. This could severely degrade the performance and repeatability of a μGC system. Moreover, the thermal crosstalk could damage some components that are not rated for high temperatures. Therefore, thermal isolation among the components is needed for a highly-integrated μGC system [Nav15].

1.5 Motivation of This Work

Microscale gas chromatographs have become more essential in gas sensing technology because they offer high selectivity and field portability for *in situ* and real time assessments. To achieve high analytical performance while maintaining low power consumption, many architectures have been investigated. Routing gas flow between the sampling path and the separation path without retaining analytes while permitting a high flow rate is challenging. Among different types of VOCs, organophosphorus compounds are ones with strong surface adsorption and can be easily retained by the chemically active sites or cold spots on surfaces along the flow path. These compounds can be highly toxic, and some used as chemical warfare agents (CWAs) and pesticides; others are used in fire retardants and fertilizers. Certain phosphonate esters, such as dimethyl methyl phosphonate (DMMP), diethyl methyl phosphonate (DEMP), and diisopropyl methyl phosphonate (DIMP), are typically used as simulants as they have similar molecular structures and chemical properties but are less hazardous [Mit97]. For a μGC system targeting these analytes, it is critical to minimize undesired surface adsorption by providing sufficient heating of various μGC components.

Previously reported μGC systems incorporated unheated COTS valves [Lew06, See07, Zam09, Kim11, Gor12, Col14, Gar15, Lee16] to control the gas flow. These μGC systems avoided

using the valves in the flow path of sample injection, separation, and detection. However, a sample inlet valve was still indispensable. In some μGC systems, the flow modulation was not directly provided by valves, but by a Deans switch combined with multiple valves [See07, Lee16]. Another approach has been to eliminate the usage of sample inlet valves. Some μGC systems, for instance, "Mercury" [Rob12] and *iGC* series [Qin14, Qin14, Qin15, Qin16] excluded the use of valves entirely. Mercury and *iGC1* adopted the simplest architecture where a uni-directional flow was supplied to a single flow path. In this architecture, multi-stage preconcentrators cannot be used, which limited the volatility range of analytes. In *iGC2* and *iGC3* where bi-directional flow was supplied to a single flow path, it remained a concern that the analyte samples were retained in the column and detector during sampling. In this work, two approaches have been investigated: 1) a microvalve with superior chemical inertness and embedded flow heating for μGC systems and 2) a flow management method that allows a μGC system to eliminate the usage of a valve at the sample inlet while being capable of analyzing highly surface-adsorptive analytes, such as phosphonate esters.

Monolithic integration shows a promising pathway to achieve high miniaturization. To permit a high analytical performance for a highly-integrated μGC system, the heating requirements of each μGC component must be met. To design custom monolithic heaters and thermal isolation cutouts for such a chip, several constraints need to be considered. First, the microfabricated monolithic heaters are typically made of thin film metals, which usually have relatively high electrical resistance because of the thin-film nature. To achieve high heating ramp rates, high heating powers are needed. However, from the electronics perspective, the heater voltages are limited. This implies that the heating powers are solely dependent on the electrical resistances of the heaters. To obtain low electrical resistances in these thin film heaters, the dimensions (*i.e.,*

width and length) of the heaters need to be carefully designed. Second, while thermally insulating substrates can be used to provide thermal isolation, the temperature uniformity becomes a challenge. The heater layout needs to be tailored to mitigate the hot spots and cold spots. Combing these two constraints, the dimensions and patterns of the heaters need to be customized based on the sizes, shapes, and heating requirements of the designated μGC components.

There are three major tasks in this work:

(i) Investigate monolithic multi-valve modules that have high flow modulation capability (*i.e.*, flow open-close ratio of >1000), superior chemical inertness, embedded flow heating, and extended lifetime.

(ii) Investigate a flow management method that permits the analysis of highly surface-adsorptive analytes without the need of a high performance microvalve at the sample inlet.

(iii) Investigate a thermal management method that identifies heating requirements of various monolithic μGC components and provides tailored on-chip heaters with high performance using a sophisticated computational model. A temperature variation of <5°C in the preconcentrators should be achieved. Heating ramp rates of >50 °C /s in the preconcentrators, >1 °C/s in the columns, and >4 °C /s in the detectors should be achieved.

1.6 Organization of This Thesis

Chapter 2 reports two monolithic valve modules – VM1 and VM2. Both valve modules combine a chemically inert microfabricated fluidic die stack with an embedded flow heater, prefabricated polyimide valve membranes, and solenoid actuators within a 3D printed housing. These valve modules, in their standalone forms, are tested with alkanes, alcohol, ketone, aromatic hydrocarbons, and phosphonates, demonstrating the low dead volume, superior chemical

resistance, and effectiveness of the embedded flow heater. VM2 is improved upon VM1 to demonstrate a lifetime of >480 hours. Both VM1 and VM2 are integrated within microscale gas chromatographs and permitted high analytical performances.

Prior to the monolithic valve modules, a piezoelectric microvalve with three-way control is designed, implemented, tested, and presented in Appendix A [Lu18]. The valve architecture and membrane material investigated in this work are later adopted by the VM1 and VM2. The piezoelectric microvalves have been tested comprehensively and repeatedly, under different pressure drops and actuated voltages for both outlets. Chemical injection tests are also performed to show the chemical resistance and low dead volume.

Chapter 3 introduces a flow management method that permits bi-directional flow in the preconcentrators without using the valve at the sample inlet. In preliminary development of this method, the separation flow is circulated by connecting the separation outlet to the separation inlet through a single pump. In the steady state, there is no flow presents in the path of sample inlet. A flow restrictor is incorporated at the sample inlet to mitigate any undesired flow. This concept is tested and validated using a setup that emulates a simplified μGC architecture. In an actual μGC implementation, the single separation pump is divided into two separation pumps. Using two pumps for separation avoids redirecting exhausts of the analytes back into the μGC system. The effectiveness of this implementation is investigated by both fluidic analysis and chemical tests. While this method is demonstrated in a PCA implementation, it is applicable to general μGC systems.

Chapter 4 describes a thermal management method on a highly-integrated μGC chip that includes preconcentrators, columns, and detectors. In this method, the targeted performances and constraints are firstly defined. Then, a sophisticated computational model is established to

thoroughly evaluate the heating ramp rates, temperature uniformities, and thermal isolation cutouts of a fabricated μGC chip. The thermography results of the fabricated chip are provided to validate the established model. Beyond the fabricated chip, two revised designs with higher heating ramp rates and temperature uniformities are reported. This thermal management method can be applied to other monolithic μGC chips that have different sizes, heating requirements, and constraints. Part of the modeling results are presented in Appendix B.

Chapter 5 concludes this dissertation and discusses future work.

Chapter 2:

Monolithic Valve Modules with High Chemical Inertness and Embedded Flow Heating

This chapter describes the first monolithically integrated multi-valve modules (VM1) with high chemical inertness and embedded flow heating for microscale gas chromatography (μGC) systems. Enhanced multi-valve modules (VM2) with high reliability and extended lifetime are presented as well. Electromagnetic solenoid actuators are selected to provide large displacement with small footprint. This not only assists the assembly process, but also facilitates the monolithic design where an array of valves can be integrated. Both VM1 and VM2 incorporate a monolithically microfabricated die stack, polyimide valve membranes, and solenoid actuators. The volumes of these multi-valve modules range from 23.2 to 32.6 cm^3, which are suitable for the small form factor of μGC systems. The die stack incorporates fused silica wafers and polyimide valve membranes that provide chemical inertness. The monolithic die stack requires only three lithographic masks to pattern fluidic microchannels, valve seats, and thin-film metal heaters and thermistors. Integration of microfabricated components and prefabricated components not only increases the structural robustness, but also allows repeating usage of microfabricated components. The performance of the multi-valve modules is compared to a commercial valve in tests using multiple volatile organic compounds (VOCs), including alkanes, alcohol, ketones, aromatic hydrocarbons, and phosphonate esters. The VM1 in standalone form shows almost no distortion of chromatographic peaks. The experimentally measured ratio of flow conductance is 3.46×10^3,

with 4.15 sccm/kPa in the open state and 0.0012 sccm/kPa in the closed state. The response time is <120 ms. The VM2 focuses on extending lifetime and integration with a microscale gas chromatograph while maintaining the superior chemical inertness and embedded flow heating. The VM2 demonstrates a lifetime of >480 hours. A microscale gas chromatograph that adopts multi-sensing progressive cellular architecture (MPCA) has successfully incorporated the VM2. This μGC system – MPCA1.0 μGC – is capable of detecting 22 chemicals known as typical indoor pollutants, breath markers, and chemical warfare agents.

2.1 Introduction

2.1.1 Overview of Microvalves

Microvalves are of great interest for many microsystem applications, such as microscale gas chromatography (μGC), cooling and refrigeration, fuel cells, lab-on-a-chip, and drug delivery [Ter79, Yan04, Hes04, Wan05, Sub06, Par08, Par09, Eva11]. The general requirements of microvalves include high flow modulation capability, low leakage, low power consumption, and manufacturability. The microsystem applications that are related to μGC, which is relevant to industrial pollution monitoring, breath analysis, and homeland security, impose additional requirements, including superior chemical inertness, low dead volume, and embedded heating capability.

Microvalves can generally be categorized into passive microvalves and active microvalves. Passive microvalves require no external power for operation, whereas active microvalves require an actuator.

Passive microvalves are typically composed of a fluidic channel and a mechanical structure that constrains the flow in a single direction. However, they are incapable of controlling the flow

actively and routing the flow in a relatively complex fluidic architecture. They are commonly used in biomedical applications and micropumps where flow rectification is needed.

Active microvalves consist of an actuator, fluidic channels, thin suspended valve membranes, and valve seats. Other than the actuator, the general structure of microvalves includes fluidic channels, thin suspended valve membranes, and valve seats, which are typically microfabricated on silicon, glass, or silicon-on-insulator substrates [Ter79, Esa89, Sho91, Bos93, Shi97, Rob98, Böh00, Rob03, Yan04, Bae07, Gro08, Par08, Par09, Eva11, Pot12, Gro15, Lu18, Lu21]. In these microvalves, the wetted materials include glass, silicon, and inorganic dielectric materials, which are chemically inert to many VOCs. However, such thin suspended inorganic valve membranes usually have challenges with complex fabrication, fragility, and low tolerance to dust particles. In some other microvalves, the valve membranes are made of polytetrafluoroethylene (PTFE) [Gro08], which eliminates the complex microfabrication steps for the valve membranes. However, the coupling to external actuators and the alignment during assembly remain challenging.

Compared to microfabricated valves, the commercial off-the-shelf (COTS) valves have similar internal structures; they include a solenoid actuator, flow paths, and a valve membrane *(e.g.,* NIV series from Clippard, Cincinnati, OH, USA, 075T series from Bio-Chem Fluidics, Inc., Boonton, NJ, USA, LFN series from The Lee. Co., Westbrook, CT, USA). Some other COTS valves do not use a valve membrane, but instead use an elastomer plunger head that is directly attached to the actuator (*e.g.*, LHL series from The Lee. Co., Westbrook, CT, USA); this approach can present chemical compatibility challenges and increase dead volume.

Active microvalves are usually categorized based on actuation mechanism [Oh06], such as piezoelectric actuation, electromagnetic actuation, electrostatic actuation, thermal actuation. This research primarily focuses on the literature that is related to active microvalves. The details of each actuation scheme are provided in the following subsections.

A. Piezoelectric actuation

The piezoelectric effect is a phenomenon that certain crystals can accumulate electric charges when subjected to mechanical force. Inverse piezoelectric effect is that these materials are mechanically deformed when subjected to an electric field. The inverse piezoelectric effect has been widely used in the micro-electro-mechanical system area to develop micro-actuators for applications like microvalves, micropumps, and micro-fuel injectors. Piezoelectric actuation not only provides fast response due to the nature of polarization, but also has low power consumption because it only consumes energy during charging [Esa89, Sho91, Rob03, Gro15]. Two modes of operation for piezoelectric actuators have been reported widely in literature: the thickness mode (d_{33}) and the planar mode (d_{31}). Actuators operating in the thickness mode generates the displacement in the direction of the applied electric field, whereas the actuators operating in the planar mode generates the displacement in the direction that is orthogonal to the applied electric field. Two types of piezoelectric actuators are commonly used: Lead zirconate titanium (PZT) stacks and piezoelectric bimorph disk actuators. PZT stacks operate in the thickness mode and typically provide large blocking forces (> 100 N) but small displacements (< 10 μm). In contrast, piezoelectric bimorph disk actuators operate in the planar mode, generating large displacements (50-500 μm) but mild blocking force (< 1 N).

Most piezoelectric microvalves reported to date consisted of microfabricated fluidic channels and valve membranes integrated with prefabricated piezoelectric actuators [Rob03, Par08,

Par09, Eva11, Gro15]. Challenges of such piezoelectric microvalves include the complexity in fabricating suspended thin valve membranes and the hermeticity when the valve is closed – particularly for gas phase analytes.

The first piezoelectric valve consists of a PZT stack actuator, a flow path, a thin suspended membrane, and a mesa structure with a device size of $20 \times 9 \times 10$ mm^3 [Esa89]. The microvalve is constructed by anodically bonding a machined silicon wafer and a machined glass wafer. The gas inlet, the fluidic channel, the suspended membrane and the mesa structure are implemented on the silicon wafer, whereas the fluidic channel, the valve seat, and the gas outlet are implemented on the glass wafer. The PZT stack actuator attached onto the silicon substrate generates a displacement of $\approx$7 μm and presses against the glass substrate when a high voltage is applied. With a pressure drop of 73.5 kPa, the microvalve delivers a flow rate of 85 ml/min and a leakage rate of rate of 0.1 ml/min.

While the small displacement from PZT stack actuator remains a challenge, the displacement can be increased by using hydraulic amplification [Rob03]. A piezoelectrically driven microvalve utilizing a drive piston structure and a hydraulic amplification chamber achieves 40-50x displacement amplification and generates $\approx$30 μm displacement. The valve consists of nine layers, including four glass substrates, three SOI substrates, and two silicon substrates with a device size of $\phi 8 \times 5$ mm^3. The valve permits a liquid flow rate of 12.6 ml/min at a pressure drop of 260 kPa.

Another solution to the small displacement from piezoelectric actuator is to increase flow area. A valve designed for cryogenic application adopts the serpentine valve seat design to increase flow area, and hence increases flow conductance [Par08] (Fig. 2.1a). The valve consists of a silicon substrate, a glass substrate, a PZT stack actuator, and a ceramic package with a device

size of 10 × 10 × 10 mm^3. With a displacement of 6 μm from the selected PZT stack actuator, the serpentine groove pattern substantially increases the perimeter of the valve seat, allows a larger flow area, and consequently maintains a high flow rate. The serpentine valve seat is fabricated on a silicon substrate serving as valve plate, which is suspended by four beams in crab-leg formation to reduce thermal stress and increase flexibility of the valve plate. The serpentine valve seat and crab-leg beams accommodate the reduction of piezoelectric coefficient and variation of coefficient of thermal expansion (CTE) for its intended application. However, such a structure does not separate the actuator from the flow path, which increases the dead volume and reduces the chemical resistance. The valve modulates gas flow from 980 sccm to 0 sccm with a pressure drop of 55 kPa at an applied voltage of 60 V. At cryogenic temperature of 80K, the valve modulates flow from 350 sccm to 20 sccm with a pressure drop of 104 kPa. The valve has a response time of 700 μs.

Other than the PZT stack type actuator, a valve using a piezoelectric bimorph disk actuator to achieve large out-of-plane displacement was presented [Gro15] (Fig. 2.1b). The valve consists of a piezoelectric bimorph disk actuator, a silicone ring support, a SOI substrate, and a glass substrate with dimensions of 17 × 17 × 1.9 mm^3. The SOI substrate, where the valve membrane is located, and the glass wafer, where the inlet and outlet are located, are assembled using an ultraviolet curable adhesive. To maintain the displacement of the actuator, the disk actuator is mounted onto the microfabricated SOI substrate through the flexible silicone ring support. The bimorph disk actuator, which is capable of providing a pre-assembly displacement of ≈19.1 μm, can generate a maximum displacement of 13 μm after assembly. The valve achieves proportional flow rate control by monitoring the capacitance of the piezoelectric actuator. At an applied voltage of 100 V, the valve modulates flow from 173 sccm to 0 sccm with a pressure drop of 50 kPa, but

suffers a leakage rate of 0.37 sccm with a pressure drop of 100 kPa. The overall flow open-close ratio can be increased by driving the actuator at its maximum voltage of 180 V. The response time of the valve is on the order of milliseconds. Piezoelectric actuation typically provides a fast response time (< 1 ms) and low power consumption. However, the small displacement usually leads to challenges in fabrication and assembly process. Although bimorph disk actuators provide a larger displacement than PZT stack actuators, their footprints are generally larger. This poses a challenge on the miniaturization of the device.

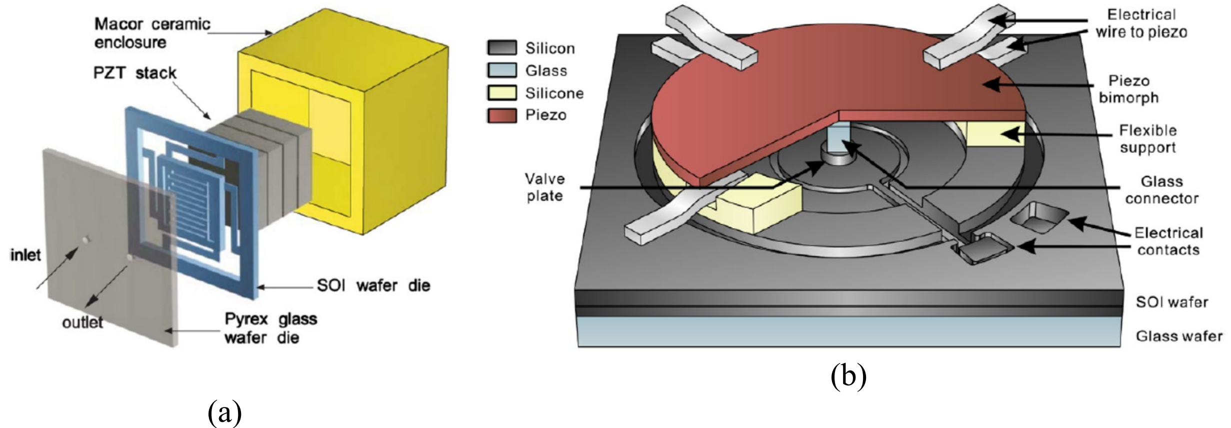

(a) (b)

Fig. 2.1: Piezoelectrically actuated valves with different types of actuators. (a) A valve using PZT stack type actuator [Par08]. (b) A valve using bimorph disk type actuator [Gro15].

B. Electromagnetic actuation

Electromagnetic actuation creates force by the interaction between magnetic field and electromagnetic field from the coil. The most common electromagnetic actuator is solenoid actuator, which consists of an electromagnetic coil and a ferromagnetic plunger. The magnetic field from the energized electromagnetic coil attracts the plunger, which is located at an off-center position in default, toward the center of the coil. The electromagnetic force generated by the solenoid actuator can be approximated as [Fur01]:

$$F_{EM} = \frac{B^2 A_{EM}}{2\mu_0} \tag{2.1}$$

where B is the magnetic field, A_{EM} is the overlapping area of the plunger, and μ_0 is the permeability in vacuum. Electromagnetic actuation has the advantage of high blocking force and large displacement at low applied voltage. But the downside is the difficulty in the miniaturization of solenoid actuators, because the magnitude of the force is proportional to the area. As the actuator scales down, the force and stroke are compromised. However, for centimeter scales, solenoid actuators maintain good performance and are popular applications in miniature valves [Shi97, Böh00, Fu03]. To reduce power consumption, latching solenoid actuators, which consume power only during switching hence saving substantial energy, have been developed.

The first reported microvalve that utilized electromagnetic solenoid actuation was developed by Terry *et al.* along with the first μGC system [Ter79] (Fig. 2.2a). The microvalve combines a solenoid actuator with a nickel diaphragm and a microfabricated silicon substrate, the latter of which consists of a valve seat and gas ports. The nickel diaphragm is normally held against the valve seat by the plunger of solenoid actuator. When the actuator is energized, the plunger is released to open the valve. The plunger assembly and the nickel diaphragm are removable to allow cleaning of the interior.

To reduce energy consumption, a valve incorporating a miniature bi-stable electromagnetic solenoid actuator was reported [Böh00]. The valve consists of two silicon substrates and a sandwiched flexible silicone diaphragm. The external solenoid actuator is seated on top of the silicon substrate, leading to a device size of $7 \times 7 \times 21$ mm^3. The top silicon substrate incorporates a boss structure to transmit actuation whereas the bottom silicon substrate incorporates two flow ports. The sandwiched flexible silicone diaphragm provides a soft contact surface to improve sealing. During valve operation, the plunger of the actuator normally presses against the valve

seat by a spring force (2.7 N) to maintain the closed state. When the current passes through the coil, the plunger is lifted (200 μm) by the electromagnetic force and stays at the latched position by the magnetic force to maintain the open state. The microvalve achieves a liquid flow rate of 6.84×10^{-2} ml/min and a leakage rate of 1.44×10^{-3} ml/min. The supplied electrical pulse has a current consumption of 500 mA and a response time of 100 ms.

Another bi-stable magnetically actuated valve uses a permanent magnet, a micro-coil, and an elastic cantilever beam to achieve the latching function [Cap00]. The valve incorporates two silicon substrates. The top one consists of a microfabricated electromagnetic coil, whereas the bottom one consists of a flexible cantilever beam and a rigid permanent magnet. The valve is normally maintained at closed state with the rigid magnet pressing against the orifice using the elastic energy from the undeformed flexible cantilever beam (Fig. 2.2b). When electric current passes through the coil, the rigid magnet is attracted, and thus bends the flexible cantilever beam to open the valve. The electromagnetic actuator provides a displacement of 150 μm and maintains the valve at open state by the magnetic force between the coil and the permanent magnet. Nonetheless, the flow path is not isolated from the cavity that is reserved for the actuator, which increases the dead volume. The valve delivers a flow conductance of 0.054 sccm/kPa. For air flow, the valve requires 2.48 mJ to be opened and 14.36 mJ to be closed with a response time of 5.3 ms and 16.4 ms respectively. For liquid flow of deionized water, the valve requires 10.09 mJ to be opened and 27.38 mJ to be closed the valve with a response time of 30 ms and 80 ms respectively. In general, electromagnetic actuation provides large blocking force and displacement. The major downside is power consumption, but latching actuators have demonstrated a sub-joule energy consumption per switch. The response time ranges from 5 ms to 100 ms.

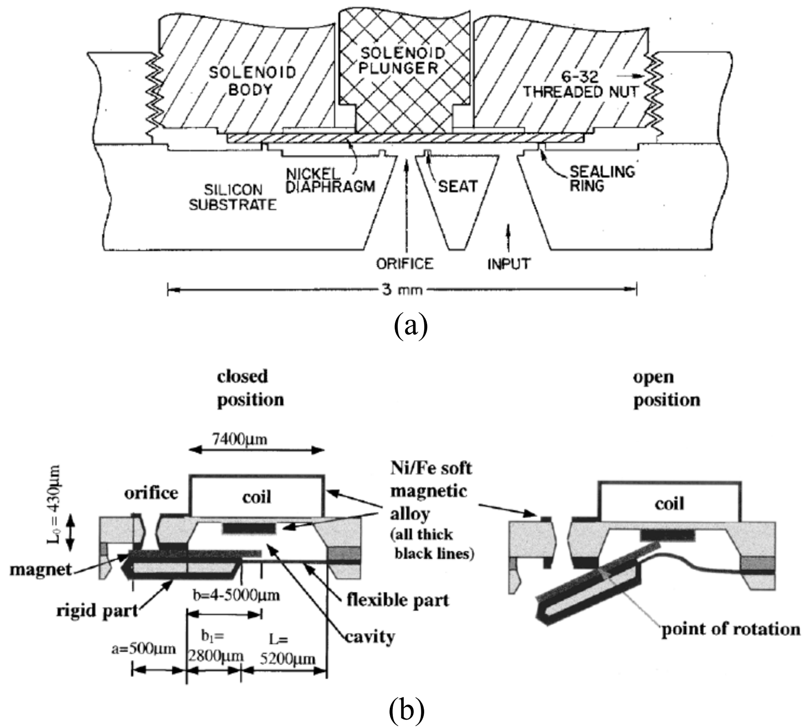

Fig. 2.2: (a) An electromagnetically actuated microvalve combined with an external actuator [Ter79]. (b) An electromagnetically actuated microvalve using a micro-coil and a flexible beam [Cap00].

C. Electrostatic actuation

Electrostatic actuation has been widely used for microvalves because of its ease of integration with microfabricated substrates. The force is generated by applying a high voltage (>100 V) across a pair of electrodes that are normally separated by <10 μm. When the voltage is applied to close the valve, the electrode seated on a thin membrane is pulled toward the other electrode seated on the substrate. The electrostatic force between the two parallel electrodes is:

$$F_{ES} = \frac{\varepsilon A_{ES} V^2}{2d^2} \tag{2.2}$$

where ε is the electric permittivity, A_{ES} is the electrode area, V is the applied voltage, and d is the distance between two electrodes. Electrostatic actuation has the benefit of fast response, low power consumption, and potential for large-scale integration [Rob98, Bos93, Tic13, Tic14, Bae07]. Nonetheless, the force is inversely proportional to the distance between the electrodes. Consequently, the blocking force is low if the distance is not small enough. This not only increases the difficulty of microfabrication, but also prevents electrostatic valves from being used for high-pressure flow applications. From equ. 2.2, with a membrane area of 1 mm^2 and an applied voltage of 100 V, 1 μm separation in air provides an electrostatic blocking force of 0.044 N.

A nested electrostatically actuated microvalve that integrates an on-chip pressure sensor with a footprint of <10 × 10 mm^2 was reported [Rob94] (Fig. 2.3a). The valve configures three sets of electrodes to actively maintain the valve at both open and close states. The electrodes are constructed on the silicon wafers, whereas the non-moving part is established on the glass substrate. The displacement of the actuator is below 12 μm, which leads to the challenge of stiction during fabrication. This is resolved by designing dimples on electrodes to reduce the contact area. The valve has a flow conductance of 7.5×10^{-2} sccm/kPa and a leakage conductance of $<7.5\times 10^{-3}$ sccm/kPa at an applied voltage of 45-60 V.

To increase the displacement, an S-shaped conductive film is introduced to replace conventional microfabricated thin membrane [Sat94]. The conductive film is sandwiched between the two electrodes and can be attracted to either side of the electrode depends on the applied voltage. One of the major benefits of the S-shaped film is that a large displacement can be obtained without compromising the blocking force, because the edge of the S-shaped film can maintain the electrostatic force effectively. The valve can sustain a pressure drop up to 100 kPa, and provides a flow conductance of 166.7 sccm/kPa while achieving a displacement of 2.0 mm. The response

time is <12.5 ms according to the membrane propagation speed and membrane size. The footprint of the valve is increased by the prefabricated membrane.

Another electrostatic microvalve exploits a hydraulic chamber to amplify the displacement and blocking force [Kim08] (Fig. 2.3b). The valve contains a hydraulic chamber that is encapsulated by flexible polymer and coated with electrodes on both sides. The valve has two outlets where the expanded hydraulic chamber can press its wall against each outlet separately to obtain three-way control. A pair of electrodes is assigned on each half (*i.e.,* left side and right side) of the hydraulic chamber. When the actuator on one side is energized, the electrodes are attracted toward each other, and thus compress the hydraulic chamber. The hydraulic fluid is then moved to the other side of the chamber, which results in the expansion on the other side, and consequently closes the outlet on the expanded side. The flow conductance of the valve is 2.03 sccm/kPa at an alternating current voltage of 120 V or a direct current (DC) voltage of >340 V. With the hydraulic amplification, the valve can be applied to high-pressure applications. Nonetheless, the response time and actuation DC voltage are larger than typical electrostatic microvalves due to the hydraulic mechanism.

Another electrostatic microvalve designed for gas fuel delivery has been developed by MIT [Yan04]. The valve is fabricated using three wafers and assembled by direct bonding. The valve is designed to withstand a temperature of 1100°C during fabrication. The flow conductance measures 0.05 sccm/kPa, and the leakage conductance measures 3.3×10^{-5} sccm/kPa. With an applied voltage of 136 V, the response time is estimated to be ≈20 ms. To demonstrate the large-scale integration of electrostatic microvalves, sixteen valves fabricated on one substrate using soft lithography and operated with portable electronics has also been implemented [Tic13]. These valves are made of polydimethylsiloxane (PDMS) and multi-walled carbon nanotubes. The valves

withstand a pressure drop of 3 kPa at an applied voltage of 217 ± 24 V. The capability of large-scale integration allows these valves to be used for applications such as pharmaceuticals, genomic analysis of cells, and antibiotic susceptibility screening of microbes.

Overall, the electrostatic microvalve provides low power consumption and fast response, nonetheless, it requires a very high actuation voltage. In addition, the distance between electrodes is a design dilemma, where small distance allows higher blocking force but limits the flow conductance.

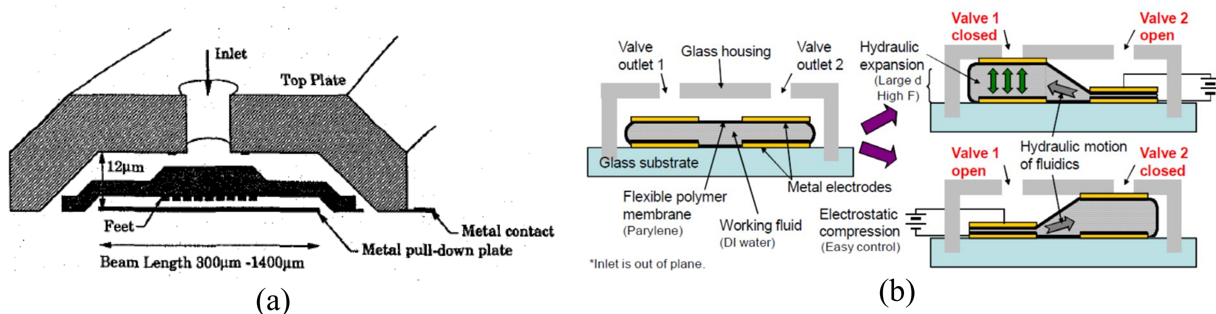

Fig. 2.3: (a) An electrostatic valve with a three-electrode configuration [Rob94]. (b) An electrostatic valve incorporating a hydraulic chamber [Kim08].

D. Thermal actuation

Thermal actuation has been utilized in different ways to form actuators for microdevices, such as shape memory alloy (SMA) actuators, thermopneumatic actuators, and bimetallic actuators. The general principle is that the formation of a substance, which can be metal, polymer, or fluid, changes when heat is applied, and returns to the original state after heat is removed. Thermal actuation generally provides large displacement but suffers from high power consumption and long response time.

SMA actuators rely on the thermally induced phase transformation of the material crystal structure. These actuators are usually fabricated from a thin binary metal sheet and tailored into a custom shape by laser-machining or micromachining [Koh99, Koh00, Bar12]. SMA actuators

produce high blocking force and large displacement with a small form factor. A microvalve integrating a SMA actuator with polyimide membrane, and polymethylmethacrylate (PMMA) substrate has been reported in the late 90s [Koh98]. The SMA actuator consists of multiple double-beam bending elements distributed in a circular arrangement. The SMA actuator and the polyimide valve membrane are bonded onto the PMMA substrate that contains the valve seat and flow ports to form the valve with a size of $6 \times 6 \times 2$ mm^3. The valve achieves a flow rate of 1600 sccm with a pressure drop of 120 kPa at an input power of 210 mW, while the SMA actuator provides a displacement of 70 μm. The response time is 0.5 - 2.5 s for opening and 1 - 2 s for closing. To reduce power consumption, an improved design incorporating hard-magnetic cylinder (*i.e.*, permanent magnet) has been established [Bar12] (Fig. 2.4a). The actuation components include two soft-magnetic layers, two SMA actuators, and a hard-magnetic cylinder. The hard-magnetic cylinder that is sandwiched between the two SMA actuators can be latched onto either soft-magnetic layer depending on the operation. Below the actuation component is a polysulfone valve membrane, a spherical plunger, and a seat valve housing. The microvalve has an overall size of $11 \times 6 \times 3$ mm^3 and a flow conductance of 7.33 sccm/kPa, while the SMA actuator provides a displacement of 40 μm at an input power of <500 mW. The switching time of the valve is 30 ms.

Thermopneumatic actuation relies on the increase of pressure within a sealed chamber that contains a working fluid with a high vapor pressure. The sealed chamber also incorporates the valve membrane, valve seat and embedded heaters. These valves are normally open valves. During the valve operation, the working fluid is heated by the embedded heater and vaporized to increase the pressure within the chamber. This results in the expansion of the chamber, and consequently exerts a force onto the valve membrane to close the valve. Thermopneumatic

actuation provides large displacement and high blocking force but requires high power consumption and long response time. Several efforts on thermopneumatic microactuator and microvalve have been reported by the Center for Wireless Integrated MicroSensing and Systems ($WIMS^2$) of the University of Michigan [Ji91, Ber95, Ric03, Pot05, Pot12]. Among them, the first reported microvalve, which has a footprint of 12×14 mm^2, employs heater grids and pressure sensors within the sealed chamber [Ric03]. The chamber incorporates a corrugated valve membrane to facilitate actuation. The valve demonstrates a flow rate of 400 sccm with a pressure drop of 133.3 kPa. An initial power of 350 mW is required for closing the valve, whereas a power of 30 mW is required for maintaining the closure. The response time of the microvalve is on the order of 10 s. A hybrid actuation scheme combining electrostatic actuation has been reported to reduce power consumption [Pot12] (Fig. 2.4b). The microvalve has a similar structure but with an additional electrostatic latch. The electrostatic latch also serves as a position sensor to monitor the displacement of the actuator. To maintain the closure of the valve, the heater grids do not need to be energized; instead, the electrostatic latch is energized. In the design, not only are the heater grids improved with a higher elevation and better arrangement to achieve better heating efficiency, but the corrugated valve membrane also has a lower spring constant to allow a larger displacement. The valve provides a flow conductance of 13.3 sccm/kPa, while constraining leakage conductance to be as low as 1.9×10^{-5} sccm/kPa. The microvalve can be closed in 430 ms with an input power of 250 mW and consumes nearly no power during the steady state due to the assistance of the electrostatic actuators. However, the response time for opening the valve, which solely depends on the cooling of the valve, takes a few seconds. Moreover, it requires a relatively high voltage of 140 V to maintain the closure.

Bimetallic actuators rely on the difference of coefficient of thermal expansion between two metals and are typically implemented by depositing a metal layer on a diaphragm, which can be made of silicon or inorganic dielectric materials [Jer94, Mes98, Lef13]. Such an actuation scheme provides a small form factor and a large stroke; however, it generates insufficient blocking force. The first bimetallically actuated microvalve combines two silicon substrates where the top substrate contains the actuator component, and the bottom substrate contains the non-moving parts [Jer94] (Fig. 2.4c). The top substrate has a circular silicon diaphragm with an annular aluminum layer, of which the diameter is 2.5 mm. Both the silicon diaphragm and aluminum layer serve as an individual resistor. In the center of the silicon diaphragm is a boss structure that is used to press against the valve seat on the bottom substrate. As the power dissipates into each resistor varies, the temperature of each component is different, which provides the actuation of the diaphragm. A displacement as large as 27.3 μm can be realized, whereas a flow conductance of 13.05 sccm/kPa is obtained. The power consumption depends on the required flow rate, but a minimum power of 150 mW is needed to open the valve. For a flow rate of ≈90 sccm with a pressure drop of 137.9 kPa, a power of 350 mW is required. The response time depends on several factors, such as the input electrical pulse to the resistors, the cooling time of the valve, and the targeted flow rate, but it generally takes a few hundred milliseconds to open and close the valve.

Another bimetallic microvalve incorporating three silicone substrates to achieve three-way control was developed [Mes98]. The top and bottom substrate has similar structure, which contains the valve seat and flow ports. The middle substrate serves as the actuator, which incorporates a bimetallic diaphragm, a central boss, and openings to allow gas travel through. The central boss on the middle substrate normally presses against the bottom valve seat, allowing gas to travel through the openings on the middle substrate and exit from the outlet on the top substrate.

When the diaphragm is actuated, the central boss presses against the top substrate, allowing the gas to exit from the outlet on the bottom substrate. The valve provides a displacement of 30 μm and demonstrates a flow conductance of 1.33 sccm/kPa with an input power of 1 W. Thermal actuation can be applied in different formations to provide large force and displacement, which makes it amenable to high-pressure application without compromising the flow conductance at open state. However, it consumes relatively high power and has a relatively slow response.

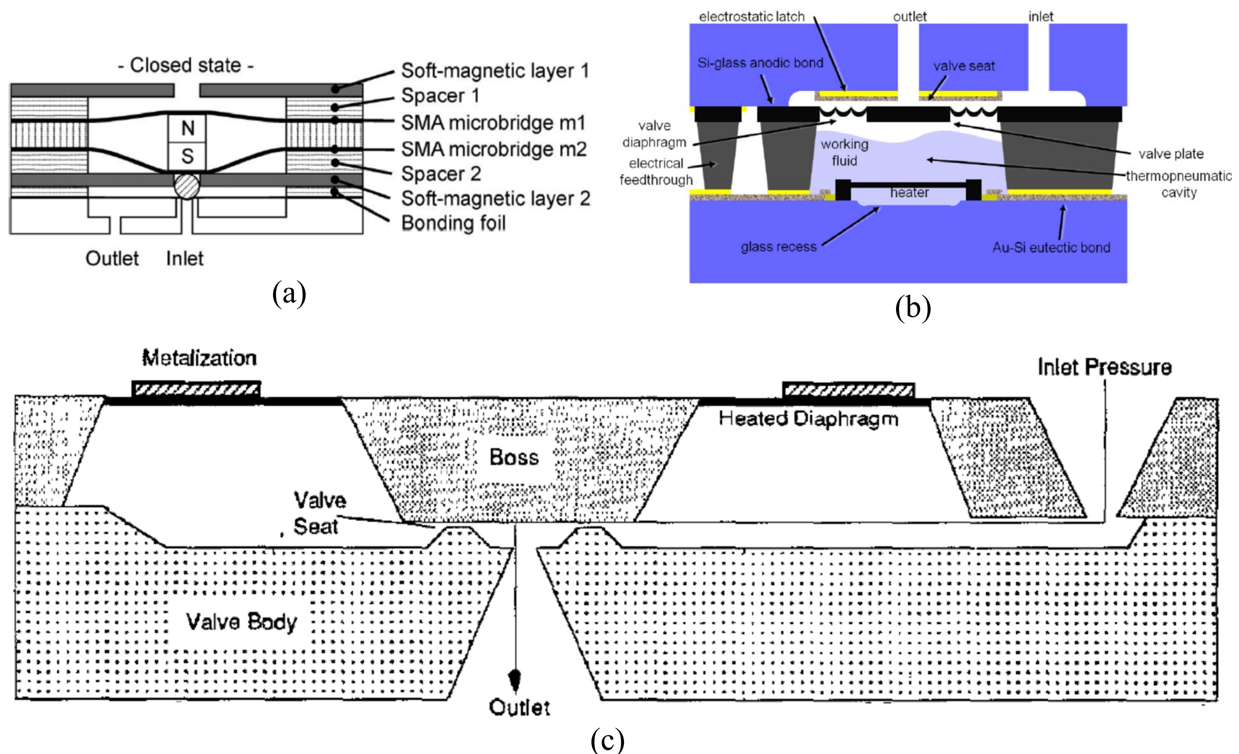

Fig. 2.4: Different types of thermally actuated valves. (a) A valve using SMA actuators [Bar12]. (b) A valve using thermopneumatic actuation [Pot12]. (c) A valve using a bimetallic diaphragm actuator [Jer94].

A table summarizing the mechanical and electrical performances of the actuation schemes is provided (Table 2.1). The chemical compatibility and dead volume are not related to actuation scheme; therefore, they are not compared in the table. Instead, they are determined by the structure and material of the valve. Microvalves that only have wetted materials of silicon, glass, and inorganic dielectric materials can be used for applications demanding stringent chemical

compatibility. Some other microvalves that utilize a prefabricated valve membrane, such as polyimide or PTFE, are also suitable for chemical applications. However, microvalves made of PDMS substrate would have issue because it tends to absorb many organic chemical species, which would lead to an inaccurate chemical analysis. The requirements of the microvalve are highly dependent on the application. In this research, the microvalves are primarily designed for gas chromatography. All the requirements are detailed in the following subsection.

Table 2.1: Performances of different actuation schemes.

Actuators	Form factor	Disp. (μm)	Force (N)	Power (mW)	Voltage (V)	Response (ms)
PZT stack	Medium	~1	~10^2	< 0.1	~10 -10^2	< 1
Piezo bimorph	Large	~10	~0.1-1	< 0.1	~10 -10^2	< 1
Electromagnetic	Medium	~10^2	~0.1-1	~10^3	~10	~10^2
Electrostatic	Small	~1	~0.01	< 0.1	~10^2	< 1
SMA	Small	~10	~0.1	~10^2	~1	~10 -10^2
Thermopneumatic	Small	~10	~0.1	~10^2	~1	~10^3
Bimetallic	Small	~10	~0.01	~10^2-10^3	~10	~10^2
*Form factor: Each level has an order of magnitude difference *Many electromagnetic microvalves are bi-stable, which only consume power during a short period of switching						

2.1.2 Goals

To develop a microvalve for μGC applications, high flow conductance, low leakage conductance, low power actuation, and facile fabrication are generally required. The microvalve needs to deliver a flow conductance of 4.0 sccm/kPa at open state while constraining the leakage conductance to below 4×10^{-3} sccm/kPa at close state (*i.e.*, an open-close ratio of >1000). This allows a μGC system to be integrated with a micropump or a COTS miniature pump while maintaining a reasonable flow rate and sampling period. In addition, the valve needs to be actively maintained in both open and closed states. This permits bi-directional flow to be used, and thus significantly increases the flexibility of μGC architecture design. Because the valve does not require frequent switching per measurement cycle, the goals of power consumption and time response are sub-Joule and sub-second per switch respectively. Furthermore, the microvalve must

create minimal impact to the chromatographic peaks. Surface-adsorptive polar analytes, such as phosphonates and phenols, tend to be adsorbed on surfaces with low temperatures or active adsorption sites. Certain organophosphorus compounds have high toxicity that can disrupt the nerve system, cause respiratory paralysis, and inflict death [Bro98]; these are used in chemical warfare agents (CWAs). Among the different classes of CWAs, nerve agents, such as sarin, soman, and tabun, are one of the most lethal. For general research, simulants, such as dimethyl methyl phosphonate (DMMP) and diethyl methyl phosphonate (DEMP), are commonly used [Mit97]. These possess similar molecular structures, volatilities, and chemical properties but are less hazardous. To admit accurate analysis of such analytes, superior chemical inertness, low dead volume, and embedded flow heating capability of the microvalve are extremely critical.

This chapter reports two electromagnetic valve modules that monolithically integrate multiple valves. These valve modules combine the fluidic die stack made of fused silica with polyimide valve membranes, solenoid actuators, and a custom two-part housing. The solenoid actuators are mechanically coupled to the valve membranes through a plunger that ends in a post of adhesive coated soft silicone or adhesive foam.

The VM1 demonstrates a high flow conductance, chemical inertness, and embedded flow heating capability. The power consumption and dynamic response are also sufficient for μGC applications. The VM2 improves the lifetime extensively while maintaining the high performance in other aspects. The VM2 is integrated with a microscale gas chromatograph that adopts the MPCA. A chromatogram of 22 chemicals is generated from a microscale gas chromatograph named MPCA1.0 μGC. MPCA1.0 μGC is capable of sampling, separating, and detecting chemicals with a wide range of volatility benefited from the superior chemical inertness and embedded flow heating of the VM2.

A hybrid piezoelectric microvalve that is investigated prior to the VM1 and VM2 is presented in Appendix A [Lu18]. The microvalve consists of a microfabricated die stack made of silicon, polyimide valve membranes, piezoelectric bimorph actuators, and rigid O-rings. These components are accommodated in a custom two-part housing that are clamped by two disk magnets. An optional heater die is incorporated into the microfabricated die stack but not tested. The piezoelectric valve provides a flow open-close ratio of 3.68×10^3, high chemical resistance, and low dead volume. The membrane material and overall valve architecture reported in this work are continued to be used in the VM1 and VM2.

In Chapter 2, the VM1 is presented in Section 2.2 whereas the VM2 is presented in Section 2.3. Both sections follow the structure of design and modeling, fabrication and assembly, and experimental results. The overall discussion and conclusion are provided in Section 2.4.

2.2 Monolithic Valve Modules – VM1

2.2.1 Design and Modeling

A. Architecture

The VM1 integrates multiple valves, which incorporate a monolithically microfabricated fluidic die stack, prefabricated valve membranes, solenoid actuators, and a customized 3D printed housing. Two modules, a 2-valve VM1 and a 3-valve VM1, are designed and fabricated. The 2-valve VM1 incorporates two valves and a 3-to-1 connector (Fig. 2.5a and c), whereas the 3-valve VM1 incorporates three valves (Fig. 2.5b and d). The fluidic die stack is made of fused silica, which contains lower metal content and, hence, provides higher chemical inertness than glass; the stack includes three microfabricated dies. The top die comprises valve seats and through-holes; each valve seat separates two through-holes (insets of Fig. 2.5a and b) and it is designed in a ring

shape in order to avoid corners that may create dead volume. The through-holes connect the flow paths of the top die to the middle die, which routes the flow to ports that are located on its perimeter. The ports are 600 μm wide and 450 μm deep for accommodating capillary tubing. All of the microchannels are 400 μm wide and 425 μm deep, with a sidewall taper of 22° off vertical. The total microchannel length of the three valves in each module ranges from 1.1 cm to 3.7 cm. The valve seats and fluidic microchannels on the top die and the middle die are created by two-sided sandblasting of a 700 μm thick fused silica wafer. The bottom die, which is comprised of a 500 μm thick fused silica substrate, incorporates a thin-film thermistor and a joule heater that follows the fluidic microchannels on the middle die; both the thermistor and heater are made of Ti/Pt.

An ideal valve membrane must provide a chemically inert surface, leak-free mating with the valve seat, flexibility for low force actuation, and infrangibility for assembly and repeated operations. A sufficiently flexible membrane that is can also accommodate the presence of dust particles. In VM1, a two-layer polyimide membrane is used as the valve membrane. Each layer is a self-adhesive polyimide film with adhesive on one side. The lower layer has a circular shape, and it is positioned above the valve seat with the adhesive side facing up, whereas the upper layer has a larger size and rectangular shape with the adhesive side facing down. Thus, the upper layer holds the lower layer on the valve seat and seals the perimeter of each valve seat. The three valves share one upper layer to simplify assembly. A disk spring at each of the three perimeters secures the membrane. With this structure, the membrane adhesive is not exposed to the flow path; the wetted materials are polyimide and fused silica, which are chemically inert to VOCs of interest in this work.

Each valve is actuated by a solenoid actuator (151082-234, Johnson Electric, Shatin, NT, Hong Kong), which consists of a magnet, an electromagnetic coil, a plunger, and a spring. Each

actuator is mechanically coupled to the valve membrane through a 3D printed plunger made of Ultem1010 polymer and a soft post made of silicone. The soft post is bonded to the plunger and the valve membrane using a flowable adhesive (Dow Corning® 734, Dow Corporate, Midland, MI, USA). This approach provides a conformable seal against the valve seat.

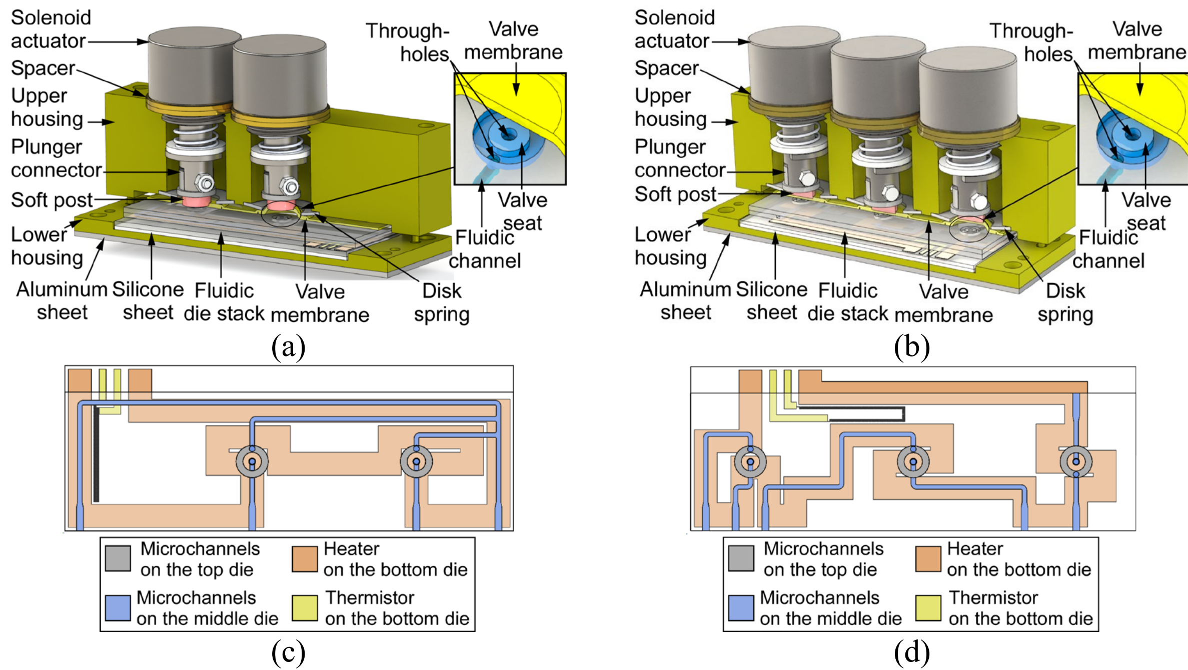

Fig. 2.5: The architecture of the VM1. (a) The 2-valve VM1. The right valve is open, whereas the left valve is closed. (b) The 3-valve VM1. The valve on the right is in the open state, whereas the rest of the valves are in the closed state. (c) Top view of the fluidic die stack of the 2-valve VM1, showing the patterns of the fluidic microchannels and the embedded flow heater and thermistor. (d) Top view of the fluidic die stack of the 3-valve VM1, showing the patterns of the fluidic microchannels and the embedded flow heater and thermistor.

A two-part housing is used in order to accommodate the components with precise alignment. It is 3D printed from Ultem1010® (provided by CIdeas Inc., Crystal Lake, IL, USA) because of the high printing resolution and thermal stability. The upper housing incorporates multiple chambers for the solenoid actuators and disk springs and jigs for alignment to the lower housing, which incorporates a cavity for the fluidic die stack and alignment holes. Nylon spacers are used to adjust the vertical position of the actuators and, consequently, the actuator displacement.

The fluidic die stack is seated within the cavity on a 500 μm- thick silicone cushion to absorb shock. In addition, a 1.5 mm-thick aluminum sheet is attached beneath the lower housing for mechanical rigidity and robustness. Screws and nuts are used to fasten the upper and lower housing.

B. Operation and force-displacement analysis

The operation of the microvalve can be explained by the separation between the plunger and the latching magnet, and by the compression of the spring (Fig. 2.6). When the microvalve is in its closed state, the spring is moderately compressed, and it maintains a spring force against the fluidic die stack. When the solenoid actuates the plunger, pulling it toward the magnet, the compression of the spring increases, but the attractive force from the latching magnet increases more rapidly. At the force transition position, the spring force and magnetic force are balanced. When the microvalve is in its open state, the magnetic force dominates over the spring force, and it latches the microvalve, even when the solenoid is turned off. To open the microvalve from the closed state, a positive 12 V, 0.9 A pulse is applied to the solenoid for 25 ms. A negative 12 V, 0.9 A pulse is applied for 25 ms in order to close the microvalve from the open state. The spring (CCF-0600-0013-M, The D.R. Templeman Co., Plainville, CT, USA) provides a displacement of 560 μm and a blocking force of 2.8 N.

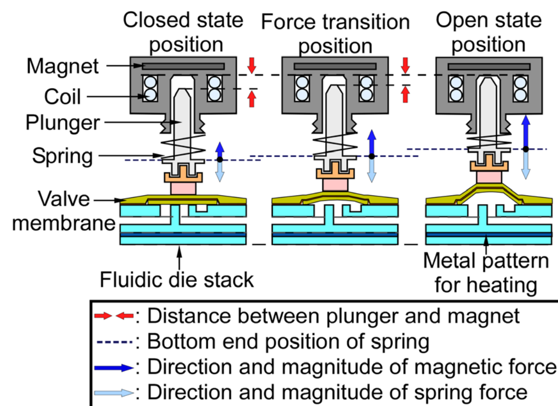

Fig. 2.6: The relationship between the distance and the force of the solenoid actuator. The closed state position has a net force exerting downward, whereas the open-state position has a net force exerting upward.

C. Control circuit

To control electromagnetically actuated valves, a control circuit is built (Fig. 2.7). Each solenoid actuator is connected to a relay on one end, serving as power, and connected to 12 V on the other end, serving as ground. Three stages of relay are used to provide either 24 V or 0 V to the power end, resulting in a voltage difference of +12 V or -12 V across each actuator. The first stage relay (*i.e.,* Relay A1-3) determines whether the power is connected to the valve. If the power is not connected to the actuator, the actuator consumes no power. The second relay (*i.e.,* Relay B) supplies either 24 V or 0 V to the first stage relay. The third stage relay (*i.e.,* Relay C) controls the second stage relay. With this configuration, the actuator can be maintained at three different states: +12V, -12V, and non-connected. Additionally, only ($N+1$) inputs were required to control N valves.

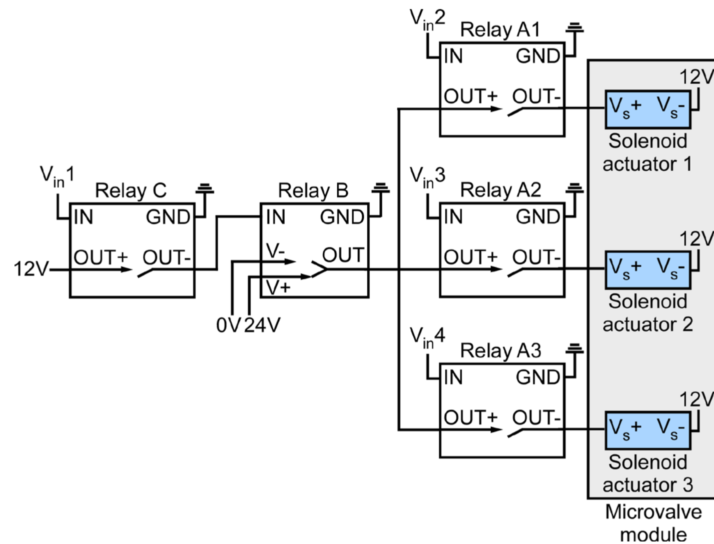

Fig. 2.7: The circuit schematic for controlling multiple electromagnetic solenoid actuators.

D. Simplified analytical thermal model

The microfabricated heater along with the thermistor is designed to heat the valve over 75°C for analyzing heavy chemical species. To calculate the required level of maintaining power

(P_{mnt}^{cal}), an equivalent thermal circuit of heat dissipation in a two-dimensional model is constructed (Fig. 2.8). The temperature of the heater surface is assumed to be isothermal at 75°C, whereas the room temperature (T_{rt}) is assumed to be 23°C. The analytical model incorporates the upper housing (UH), which is approximated as a block, and the whole bottom part of the monolithic valve module, including the polyimide valve membrane, fluidic die stack, silicone sheet, lower housing (LH), and the aluminum sheet. This model represents both sampling and separation valve modules. The heat is assumed to dissipate in both vertical (*i.e., z* axis in Fig. 2.8a) and lateral (*i.e., y* axis in Fig. 2.8a) directions. To determine P_{mnt}^{cal}, the conductive (R_{th}^{cd}) and convective (R_{th}^{cv}) thermal resistance of each component are obtained using the thermal transport equations [Inc07]

$$R_{th}^{cd} = \frac{t}{kA^{cd}} \tag{2.3}$$

$$R_{th}^{cv} = \frac{1}{h_{air}A^{cv}} \tag{2.4}$$

$$P_{mnt}^{cal} = \frac{\Delta T}{\Sigma R_{th}} \tag{2.5}$$

where t is thickness, k is thermal conductivity, and A^{cd} is heat conduction area; h_{air} is free convection coefficient of air, which typically has a range of 2-25 [Inc07], and A^{cv} is effective heat convection area; ΔT is the temperature difference, and ΣR_{th} is the total thermal resistance.

The resulting thermal resistance of each component and the parameters used for calculation are provided in Table 2.2. The valve module can be maintained at 75°C with a P_{mnt}^{cal} of 0.9 W. The calculated results show that the valve can be heated to 75°C with a moderate power, which meets the heating requirements. More detailed FEA is provided in the next section.

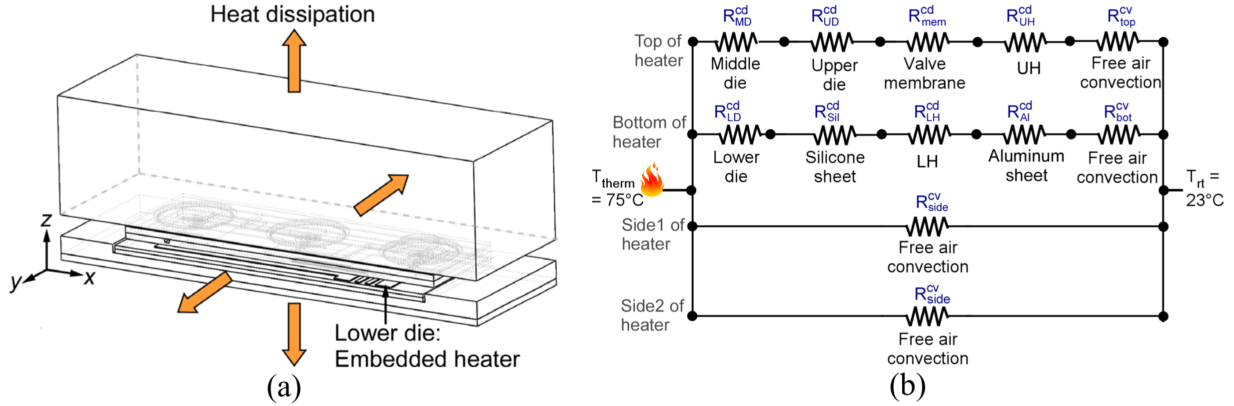

Fig. 2.8: (a) The geometric model used in the simplified analytical model with 2D heat dissipation. (b) The equivalent thermal circuit of thermal flux transporting from the embedded heater to ambient

Table 2.2: The parameters used in the simplified analytical model and the resulting thermal resistances.

Parameters			
k_{mem}	0.12 W/mK	t_{UH}	13.5 mm
k_{UD}, k_{MD}, k_{LD}	1.38 W/mK	t_{mem}	25 µm
k_{Sil}	0.20 W/mK	t_{UD}, t_{MD}	700 µm
k_{UH}, k_{LH}	0.12 W/mK	t_{LD}	500 µm
k_{Al}	205 W/mK	t_{Sil}	500 µm
A^{cd}	465.6 mm^2	t_{LH}	3.0 mm
$A^{cv}_{top}, A^{cv}_{bot}$	869.8 mm^2	t_{Al}	1.5 mm
A^{cv}_{side}	73.7 mm^2		
Calculated resistances (K/W)			
R^{cd}_{MD}	1.09	R^{cd}_{LD}	0.78
R^{cd}_{UD}	1.09	R^{cd}_{Sil}	5.37
R^{cd}_{mem}	0.45	R^{cd}_{LH}	53.69
R^{cd}_{UH}	241.62	R^{cd}_{Al}	0.02
$R^{cv}_{top}, R^{cv}_{bot}$	45.99 (h≈25)	R^{cv}_{side}	542.59
ΣR	60.32		

E. Thermal modeling

The thin-film heater and thermistor allow the microvalve to be compatible with surface-adsorptive chemical species. The thermal characteristics of the valve are simulated by finite element analysis (FEA) while using COMSOL Multiphysics® 5.3. The simulated structure (Fig. 2.9a) includes the entire lower housing and its contents, as well as the upper housing; for simplicity, the simulated structure excludes the actuators, plunger connectors, and soft posts, all of which

contribute to negligible heat conduction from the heated fluidic die stack because of the low thermal conductance and small contact area of the soft posts. The empty space in the microvalve module is modeled as air. Additionally, the microvalve module is assumed to be located on a suspended PCB, thus allowing natural air convection on all of the exterior surfaces. The convective heat transfer coefficients ae computed within COMSOL based on the configuration and characteristic lengths of the exterior surfaces.

The three valves are heated up simultaneously, as they share one embedded heater. With a heater power of 1.1 W, the temperature around the thermistor area (T_{therm}) rises from room temperature (23°C) to 75°C, whereas the lowest temperature in the fluidic microchannels rises from room temperature to 65°C (Fig. 2.9b). Each valve is assumed to have 10 sccm air flow rate at its inlet to mimic a μGC system in sampling mode. The temperature of the incoming flow rises from room temperature to 90% of steady-state temperature within a travel distance of 1.9 mm past the inlet. The resulting temperature distributions for the middle and right valves are shown in the insets of Fig. 2.9b. This simulation confirms that the thin-film heater can heat the valve to a temperature that is sufficient for analyzing surface-adsorptive analytes. It also shows that, even with high air flow supplied to the microvalve inlet, the incoming sample stream can be rapidly heated.

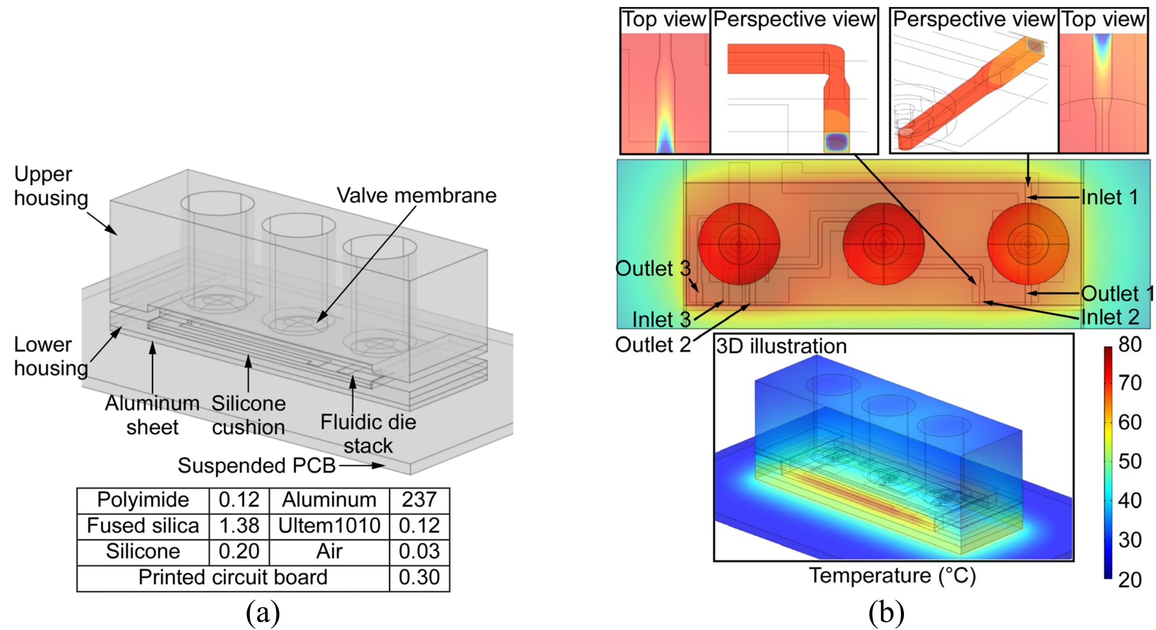

Polyimide	0.12	Aluminum	237
Fused silica	1.38	Ultem1010	0.12
Silicone	0.20	Air	0.03
Printed circuit board			0.30

Fig. 2.9: (a) The geometric model and the thermal conductivity values (W/mK) used in the simulation. (b) The temperature distribution of fluidic die stack with a simulated heater power of 1.1 W. Close-up views of the valve inlets are shown in the insets.

F. Flow resistance modeling

The flow resistance of the microvalve in the open state is estimated by FEA using COMSOL Multiphysics® 5.3. The simulated structure represents the gas flow path of the middle valve in Fig. 2.5b and d, *i.e.*, it includes two microchannels, the valve seat, and the valve membrane region. The height of the microchannels is assumed to be 425 µm, and the sidewall taper is represented. The height of the valve membrane region, which is determined by the actuator displacement, is assumed to be 560 µm.

The simulation assumes laminar flow. A flow rate of 10 sccm is supplied to the inlet, while the outlet is assumed to be at ambient pressure. The simulated pressure drop across the microvalve is 0.52 kPa (Fig. 2.10), with a pressure drop of 0.21 kPa in the fluidic microchannel upstream of the valve membrane region, 0.02 kPa in the valve membrane region, and 0.29 kPa in the fluidic microchannel downstream of the valve membrane region. The overall flow resistance of the

microvalve in the open state is 0.052 kPa/sccm. As evident from the pressure distribution, the flow resistance of the membrane region is negligible because of the large membrane displacement.

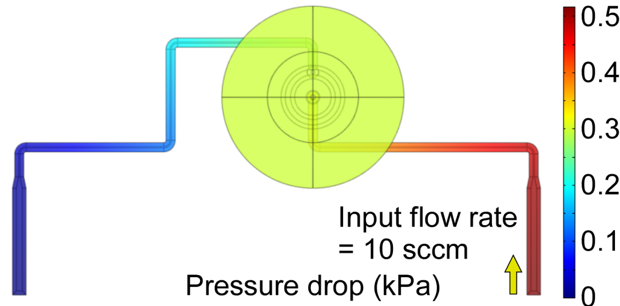

Fig. 2.10: The pressure distribution along the flow path of the middle valve of the 3-valve VM1.

2.2.2 Fabrication and Assembly

The fluidic die stack is lithographically fabricated[1] using a three-mask process. The valve seats and fluidic channels on the top die and the middle die are created by two-side sandblasting (provided by Ikonics® Corporation, Duluth, MN, USA) of a 700 µm thick fused-silica wafer. The heater and thermistor on the bottom die are formed by a layer of Ti/Pt deposited by electron-beam evaporation and patterned by a lift-off process on a 500 µm thick fused-silica wafer. The three dies are bonded by an epoxy (Epotek 377, Epoxy Technology, Inc., Billerica, MA, USA) (Fig. 2.11). The sizes of the fluidic die stack of 2-valve VM1 and 3-valve VM1 are $3.9 \times 1.4 \times 0.2$ cm^3 (Fig. 2.12a and Fig. 2.12c). On average, each valve has a footprint of 1.3×1.4 cm^2, which is 4.5x more compact than our previous work [Lu18].

During the assembly, capillary tubes are attached to the gas flow ports in the fluidic die stack using a high-viscosity epoxy (Stycast2850FT, Henkel, Düsseldorf, Germany). The valve membrane is attached to the fluidic die stack by the upper layer of the membrane, which is self-

[1] Part of the valve module fabrication was performed by Dr. Ramprasad Nambisan and Dr. Alexander Benken.

adhesive on one side. The adhesion between the soft posts, the plunger connector, and the valve membrane is provided by a flowable adhesive specific for silicone interface (Dow Corning® 734, Dow Corporate, Midland, MI, USA). All the components are assembled into the allocated positions in the two parts of the housing, which are combined and fastened by screws and nuts. The sizes of the assembled 2-valve VM1 and 3-valve VM1 are 5.3 ×1.7 × 4.5 cm^3 (Fig. 2.12b and Fig. 2.12d).

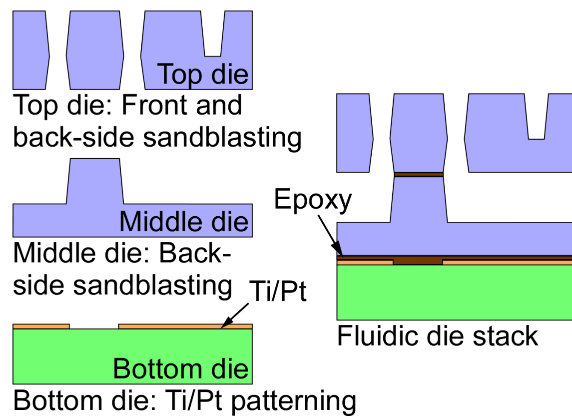

Fig. 2.11: The die stack fabrication process. The valve seats, fluidic microchannels, and through-holes are created by a two-mask sandblasting process. The Ti/Pt layer is patterned while using another mask. Three dies are bonded into a stack to form the fluidic die stack.

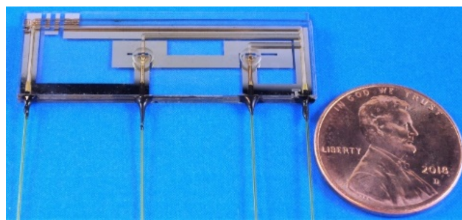

(a)

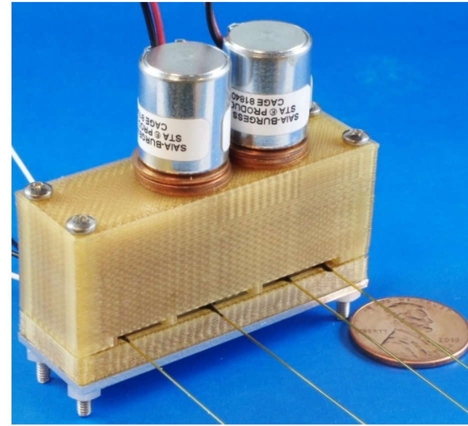

(b)

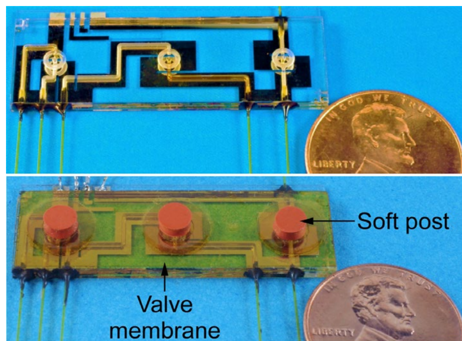

(c)

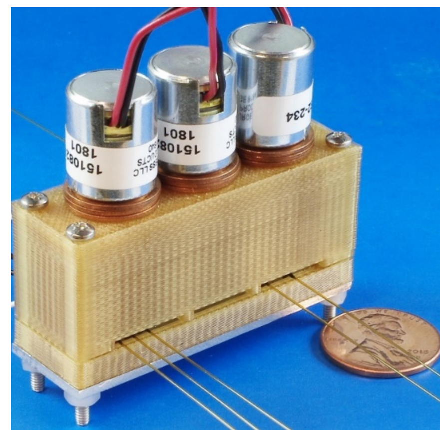

(d)

Fig. 2.12: (a) A photograph of the fluidic die stack of the 2-valve VM1. (b) Final view of the assembled 2-valve VM1. (c) Photographs of the fluidic die stack of the 3-valve VM1 prior to and following the assembly of the valve membrane and soft post. (d) Final view of the assembled 3-valve VM1.

2.2.3 Experimental Results

A. Flow conductance tests

To characterize the flow conductance of the valve, the flow rate through the microvalve was measured over a range of pressure drop. The test was conducted at room temperature using ambient air as the medium. The setup consisted of a pump (mp6, Bartels Mikrotechnik GmbH, Dortmund, Germany), a differential pressure sensor (MPXV5010DP, NXP, Austin, TX, USA), and flow meters (FMA 1603A & 1601A, Omega Engineering, Inc., Norwalk, CT, USA) (Fig. 2.13). The flow rates through the microvalve and the corresponding pressure drop across the

microvalve were measured while varying the blocking pressure of the COTS pump module. Air was supplied by the pump in one of two regimes of microvalve operation: positive pressure or negative pressure. In the positive pressure regime, the pressure within the valve membrane region was higher than the ambient pressure. This generated a force pushing against the valve membrane and counteracting the latching force in the closed state. In the negative pressure regime, the pressure within the valve membrane region was lower than the ambient pressure. Thus, this generated a force pulling down the valve membrane and counteracting the latching force in the open state.

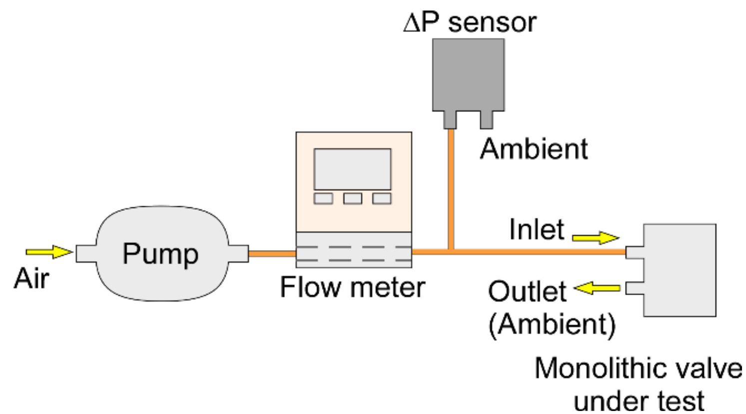

Fig. 2.13: The test setup used to characterize the fluidic performance of the valve.

In the open state, the measured flow rates increased proportionally with the measured pressure drops across the microvalve over a range of 0.66 kPa to 1.07 kPa (Fig. 2.14a). The slope of relationship between the flow rate and pressure drop indicated that the microvalve flow conductance was 4.15 sccm/kPa when open. When the microvalve was closed, the measured flow rate showed a linear relationship with the measured pressure drop over a range of 4.21 kPa to 9.72 kPa (Fig. 2.14b), with a leakage conductance of 0.0012 sccm/kPa. Based on these results, the typical open-close ratio of flow conductance of the microvalve was 3.46×10^3. The microvalve showed normal operation in both the positive pressure and negative pressure regimes. The

microvalve could withstand positive pressure of 9.72 kPa in the closed state and negative pressure of 0.66 kPa in the open state, respectively. Higher magnitudes of negative pressure were not tested, because the resulting flow rates would exceed the need of typical μGC systems.

The flow conductance was measured with two capillary tubes that were attached to the two gas flow ports of the microvalve. The two capillary tubes had an inner diameter (ID) of 250 μm and a total length of 6 cm. Estimated by the Poiseuille's law [Bru07], the two capillary tubes presented a total flow resistance of 0.187 kPa/sccm. After subtracting the flow resistance of capillary tubes from the experimental flow resistance, the flow resistance of the microvalve was determined as 0.053 kPa/sccm, being only 1.9% different from the simulated flow resistance (*i.e.*, 0.052 kPa/sccm).

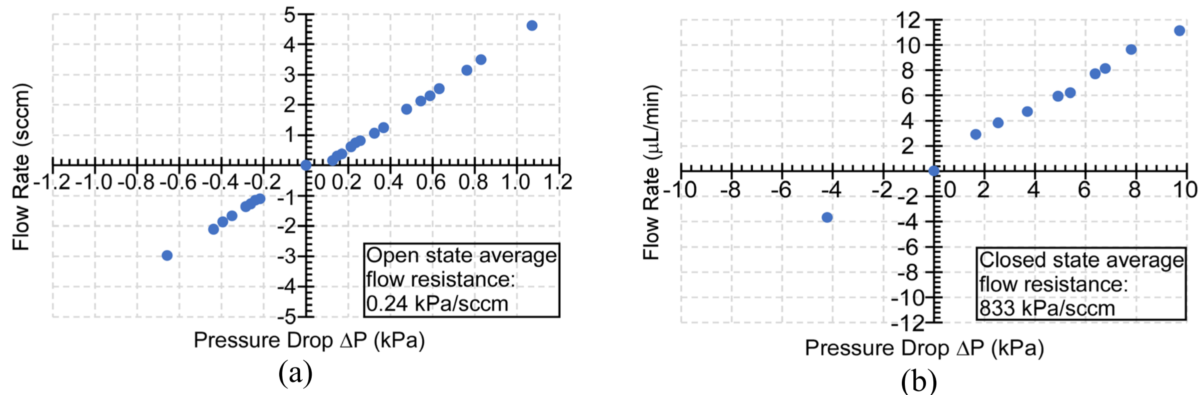

Fig. 2.14: (a) Flow characteristics for an open microvalve. (b) Leakage characteristics for a closed microvalve.

B. Dynamic response tests

To study the dynamic response of the actuator, the actuator operation was recorded by a video camera. A light emitting diode (LED) was connected with the solenoid actuator as an indicator of the applied current. At time 0, the current started to illuminate the LED; at time 90 ms, the plunger started to move; at time 120 ms, the plunger reached the end position (Fig. 2.15). These measurements indicated that there was 90 ms delay between the application of the actuation current

and the start of actuation, and 30 ms duration for the actuation. Therefore, the overall time that was required for a complete actuation was ≈120 ms.

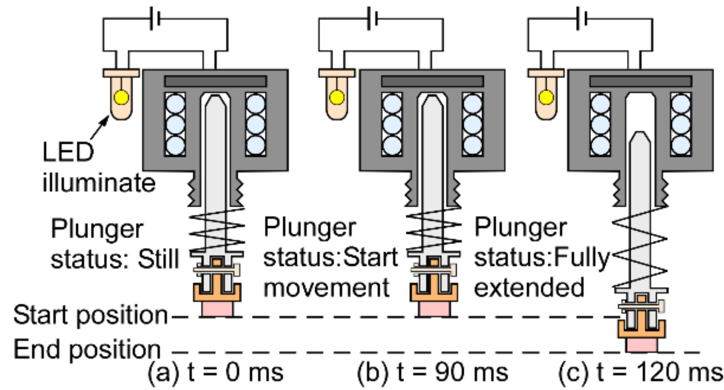

Fig. 2.15: Dynamic response of the valve. (a) At 0 ms, the light emitting diode was turned on, confirming the passage of electric current. (b) At 90 ms, the plunger started to move. (c) At 120 ms, the plunger reached the end position.

C. Power and energy consumption

During the switching transients, the actuator consumed 0.27 J per switch. In the latched states (*i.e.*, fully open and fully closed states), power was only consumed for the flow path heater, if at all. The embedded flow heating was controlled by a close-loop algorithm in LabVIEW, in which the input current and voltage were monitored. The microvalve required 144.5 J to be heated to 75°C; this temperature could be maintained with an input power of 1.0 W (Fig. 2.16). The measured result matched the simplified thermal modeling result with only 10% difference. The maximum power that was provided in this test was limited to ≈2.4 W, although higher power could be used to accelerate the heating.

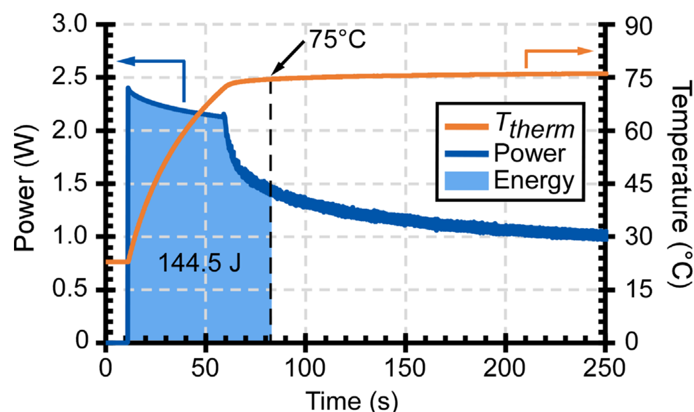

Fig. 2.16: The energy and power consumption of the microvalve during heating. The microvalve was heated to and maintained at 75°C under servo control.

D. Chemical injection tests

The impact of the valve on chromatographic peaks was evaluated while using a benchtop gas chromatograph (7890A, Agilent Technologies, Inc., Santa Clara, CA, USA) equipped with an oven, within which were located a flame ionization detector (FID), and a separation column with 1 m length, 320 µm ID, and 5 µm thick OV-1 stationary phase coating (115-3206, Ohio Valley Specialty Company, Marietta, OH, USA) (Fig. 2.17). The valve under test was located outside the oven and connected along the flow path, downstream of the inlet and upstream of the separation column and the FID. The column was maintained at 80°C inside the oven. With 0.6 sccm N_2 carrier gas flow, the analytes injected at the inlet flowed through the valve in its open state, the separation column, and into the FID.

The experiments included four test cases. In Case 1, a benchmark for the chromatographic peaks was established without any valve; a chemically deactivated capillary load that had equivalent flow resistance to the microvalve was used in place of the valve. In Case 2, the microvalve was operated at 22°C ambient temperature. In Case 3, the microvalve was operated at 80°C while using the embedded flow heating. In Case 4, the microvalve was replaced by a COTS valve (LHLA1231211H, The Lee Co., Westbrook, CT, USA) that has been used previously in

multiple μGC systems [Zam09, Kim11, Gar15, Lee16, Col14]. The COTS valve was only operated at 22°C ambient temperature, as it does not have embedded flow heating capability.

Two chemicals were selected in order to compare these four cases: 1-butanol, representing light polar species, and DEMP, representing heavy polar species. The former is a polar alcohol with a Kovats retention index (RI) of 660, whereas the latter is an organophosphorus compound with a Kovats RI of 975. The responses of the four cases are compared in the normalized peaks that are presented in Fig. 2.18. The FID signal intensity of each case normalized to its peak is plotted against a time axis. The time axis is centered at the peak and ratioed to peak width at half height (PWHH) for Case 1 in order to compensate for run-to-run variation in the test setup [Fol83]. Thus, a Case that provides a PWHH of 2 on this plot represents a peak that is double the width of the reference Case 1, and the overlay of these normalized peaks readily reveals the chromatogram distortion that is attributable to the valve under test (Fig. 2.19).

For the 1-butanol peak, the unheated microvalve (Case 2) did not cause any noticeable distortion relative to Case 1, but it showed 20% broadening for the DEMP peak. The heated microvalve (Case 3) showed no distortion for both the 1-butanol peak and DEMP peak. In contrast, the unheated COTS valve (Case 4) increased PWHH of the 1-butanol peak by 240% (Fig. 2.18a). The DEMP peak was virtually eliminated in Case 4, which indicated that DEMP was severely retained by the COTS valve. Thus, the light polar species were slightly affected by the microvalve operating at room temperature, but severely affected by the COTS valve. Further, the heating of the microvalve virtually eliminated distortion. These results were verified with multiple runs of each test case.

Additional chemicals that were tested in Case 3 included a non-polar mixture (containing pentane, benzene, toluene, ethylbenzene, o-xylene, and decane), and a polar mixture (containing

acetone, 1-butanol, chlorobenzene, DMMP, and DEMP). In both chromatograms, which are shown in Fig. 2.19, all of the chemical species eluted in the sequence of their expected retention time [Fol83] and did not show significant peak distortion. Overall, the results show that the heated microvalve does not retain analytes and, consequently, that the sensitivity of μGC systems that incorporate it will not be affected.

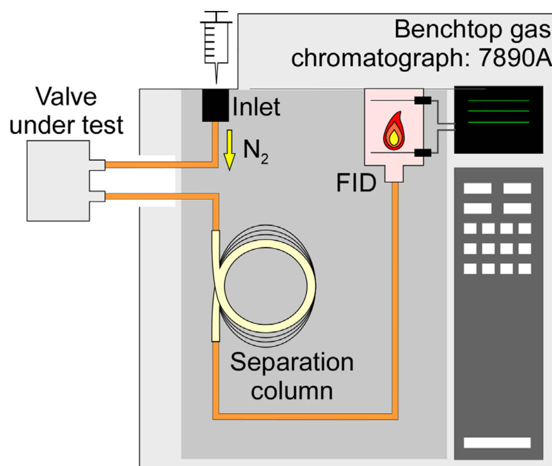

Fig. 2.17: The test setup of the chemical injection tests. The valve under test was connected to the flow path of a benchtop gas chromatograph (7890A, Agilent Technologies, Inc., Santa Clara, CA, USA).

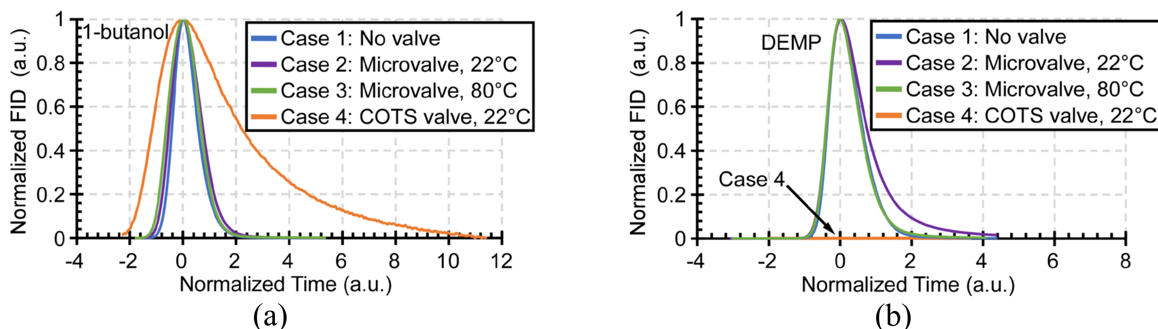

Fig. 2.18: (a) Normalized and shifted peaks for 1-butanol. (b) Normalized and shifted peaks for diethyl methyl phosphonate.

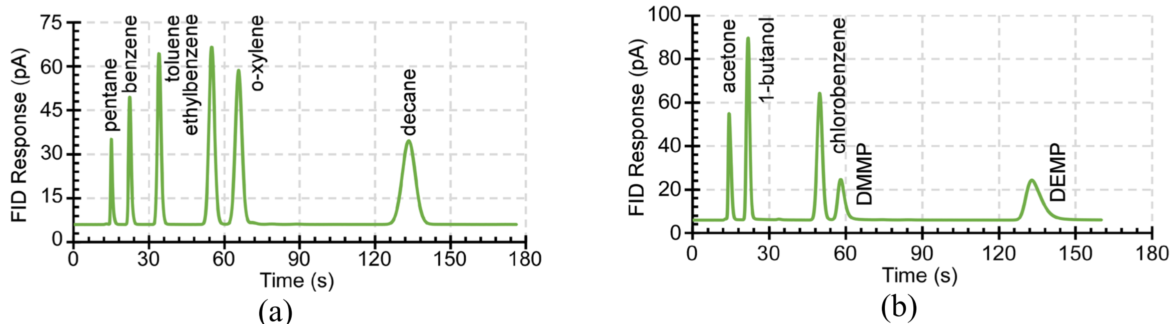

Fig. 2.19: (a) The chromatogram of non-polar chemical analytes in Case 3. (b) The chromatogram of polar chemical analytes in Case 3.

2.3 Enhanced Monolithic Valve Modules – VM2

2.3.1 Design

A. Failure analysis

Embedded flow heating is demanded for analyzing surface-adsorptive analytes, however, it is observed that the embedded flow heating creates reliability issues for the VM1. In the VM1, a flowable adhesive (Dow Corning® 734, Dow Corporate, Midland, MI, USA) is applied at the contact interface of the plunger connector, soft post, and valve membrane to couple them. After the flowable adhesive is cured, it forms a solid bonding layer. However, the cured flowable adhesive is subject to unpredictable thermal deformation at the elevated temperature, which results in leakage during valve closure (Fig. 2.20a). To mitigate the undesired thermal deformation, the flowable adhesive is applied only at the perimeter of the silicone post, nonetheless, the bonding strength becomes weak. This leads to the detachment of the silicone post from the valve membrane when the supplied flow is in the negative pressure regime where a force pulling down the membrane is created, and consequently the failure of the valve (Fig. 2.20b). This is problematic because a μGC system may require a high flow rate in the negative pressure regime during sampling.

This dilemma can be addressed by replacing the flowable adhesive and the silicone post with a double-sided adhesive foam with a higher temperature rating. This provides several benefits. First, very few adhesives can adhere to a silicone surface reliably. Eliminating the usage of silicone post permits more options of adhesive to be investigated. Second, the adhesive foam has a firm geometry and high conformability, which allow uniform thermal deformation of the foam. If the foam expands, it exerts a compressing force toward the contact surfaces, *i.e.*, the valve seat, rather than creating gaps and consequently leakage. Moreover, the foam is soft, providing the same level of conformable seal as the silicone post during the valve closure. The assembly process is also simplified as less components are used. With all these assumptions, a double-sided adhesive rated for high temperature applications is identified, incorporated within the VM2, and thoroughly evaluated based on the lifetime of the valve.

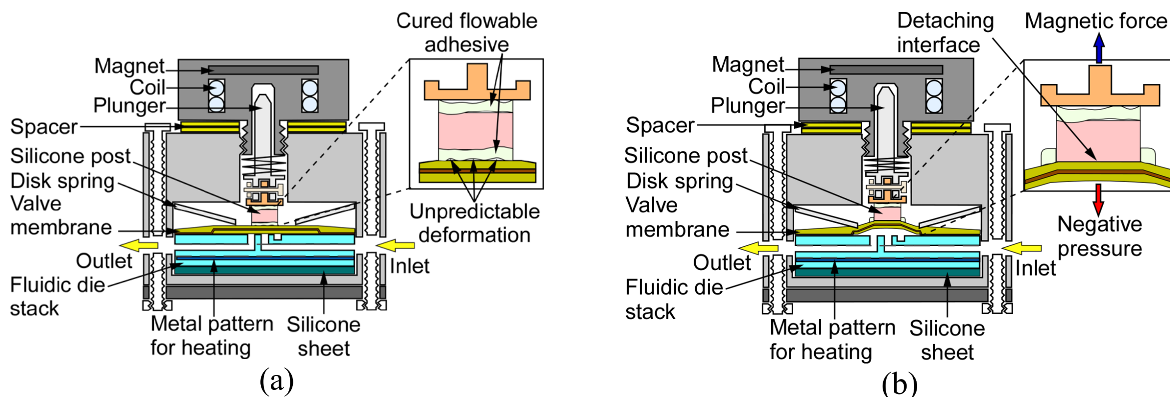

Fig. 2.20: (a) The unpredictable thermal deformation of the cured flowable adhesive that creates leakage. (b) The detachment of valve membrane when flow with negative pressure is supplied.

B. Architecture

The VM2 adopts similar architecture as the VM1 (Fig. 2.21a and b). Two modules, a 2-valve VM2 and a 3-valve VM2, are designed and fabricated. The 2-valve VM2 incorporates two valves with a common inlet (Fig. 2.21a and c), whereas the 3-valve VM2 incorporates three valves and a 3-to1 connector (Fig. 2.21b and d). A microfabricated fluidic die stack is combined with

valve membranes, solenoid actuators, and a customized two-part housing. The fluidic die stack is made of three layers of fused silica. The top die incorporates valve seats and through-holes, the middle die incorporates fluidic channels and gas flow ports at the perimeter, and the bottom die incorporates metal pattern for embedded flow heating (Fig. 2.21c and d). The valve membranes are made of two layers of self-adhesive polyimide membrane. The lower layer is a circular film aligned onto the valve seat area and oriented with its polyimide side facing down to provide chemical inertness. The upper layer is a larger film oriented with its adhesive side facing down to anchor the lower layer onto the fluidic die stack and prevent leakage to ambient. Disk springs are used to mechanically clamp the perimeters of the upper valve membrane to avoid interaction between analytes and the adhesives on the back side of the upper polyimide valve membrane. Multiple solenoid actuators attached with plunger connectors are incorporated within the VM2 (Fig. 2.21).

Different from the VM1, a double-sided adhesive foam (VHB 5962, 3M, Saint Paul, MN, USA) is used to couple the actuator to the valve membranes. The adhesive foam provides high foam strength, conformability, and adhesion. More importantly, the high adhesive strength can be maintained at an elevated temperature up to 90°C. Three different thicknesses, 25 mil, 42 mil, and 62 mil, of the adhesive foam are tested and proves that sufficient thickness is needed to provide reliable sealing during valve closure. Therefore, the 62-mil thick adhesive foam is selected. To enhance the bonding strength in the contact interface of the adhesive foam and the plunger connector, the material of the plunger connector is changed from Ultem 1010 polymer to aluminum. Aluminum has a higher surface energy that allows the adhesive to spread on easily and achieves an intimate contact. This significantly improves the bonding strength at the contact interface. The plunger connector is manufactured by CNC machining.

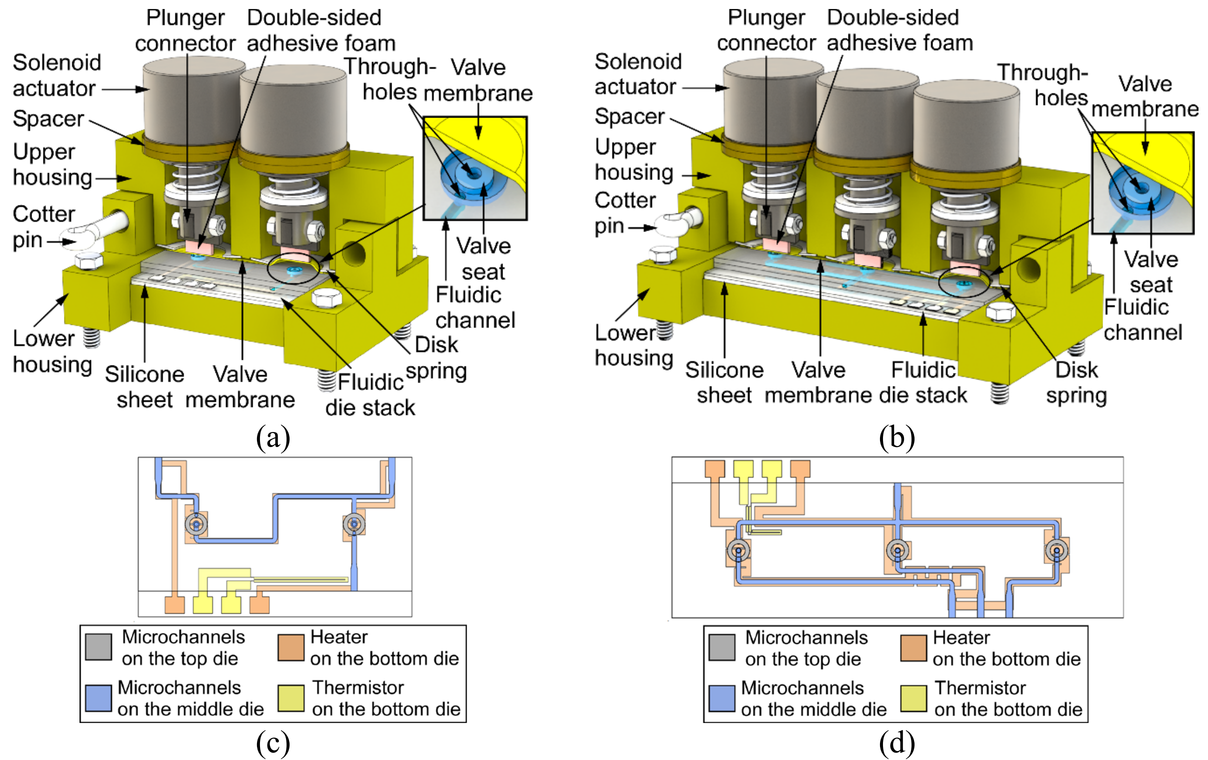

Fig. 2.21: The architecture of the VM2. (a) The 2-valve VM2. The right valve is open, whereas the left valve is closed. (b) The 3-valve VM2. The valve on the right is in the open state, whereas the rest of the valves are in the closed state. (c) Top view of the fluidic die stack of the 2-valve VM2, showing the patterns of the fluidic microchannels and the embedded flow heater and thermistor. (d) Top view of the fluidic die stack of the 3-valve VM2, showing the patterns of the fluidic microchannels and the embedded flow heater and thermistor.

All the components, including fluidic die stack, valve membranes, and solenoid actuators are assembled within a revised two-part housing. The housing components are made of Ultem 1000 and are manufactured by CNC-machining process, which provides a better surface quality than 3D printing. To improve assembly process, instead of using screws and nuts to fasten the two parts, cotter pins are used. An assembly hole is allocated on each side of both the upper housing and lower housing. The locations of assembly holes in the upper housing are 50 µm higher than the assembly holes on the lower housing. When the cotter pins are inserted through the assembly holes to combine the two parts, the upper housing compresses against the lower housing by 50 µm. This mating mechanism not only simplifies the assembly process, but also prevents excessive

clamping force from damaging the fluidic die stack as the clamping force is defined by the offset between the assembly holes. The lower housing has a thicker base, eliminating the need of the aluminum sheet. Each VM2 is mounted onto a custom PCB to facilitate electrical testing and control. The wires of the solenoid actuators and the connection pads of the embedded flow heaters are soldered to testing headers that are easily accessed. The major changes between the VM1 and the VM2 are summarized in Table 2.3.

Table 2.3: The differences between the VM1 and VM2.

Valve generation	VM1		VM2	
Module	2-valve	3-valve	2-valve	3-valve
Size (cm^3)	5.3×1.7×4.4		3.9×2.7×4.4	5.5×2.7×4.4
Footprint of FDS* (cm^2)	3.9×1.4		2.5×1.2	4.0×1.2
Soft post	Silicone		Double-sided adhesive foam	
Plunger connector	3D-printed Ultem1010		CNC-machined aluminum	
Two-part housing	• 3D-printed Ultem1010 • Assembled by screws and nuts		• CNC-machined Ultem1000 • Assembled by cotter pins • Thicker lower housing	
Aluminum sheet	Added		Removed	
*FDS: Fluidic die stack				

C. Gas pressure management

When a gas flow is supplied to the microvalve, pressure drop occurs along the flow path. Whether the supplied flow is in the positive pressure regime or negative pressure regime, an undesired counteracting force is generated. It is preferred to reduce this counteracting force by alleviate the pressure difference between the membrane area (P_{mem}) and ambient (P_{amb}), particularly when the supplied flow is in the negative pressure regime. As revealed in the failure analysis, the valve membrane can be detached from the double-sided adhesive foam when the negative pressure within the valve membrane is high. Based on the equivalent fluidic circuit (Fig. 2.22), the difference between P_{mem} and P_{amb} is determined by the flow resistance of the upstream microchannel ($R^{up}_{\mu cha}$) and the upstream tubing (R^{up}_{tubing}). To reduce this pressure difference,

distribution of flow resistance and pressure along the flow path of microvalve are estimated. The equations for calculating flow resistance of a circular channel (R_h^{cir}) and a rectangular channel (R_h^{rec}), total flow resistance ($R_{h,total}$), and pressure drop are [Pri16]:

$$R_h^{cir} = \frac{8\mu_{dyn}L}{\pi r^4} \tag{2.6}$$

$$R_h^{rec} = \frac{12\mu_{dyn}L}{wh^3(1-0.63\,w/h)} \tag{2.7}$$

$$R_{h,total} = R_{h1} + R_{h2} \tag{2.8}$$

$$\Delta P = Q \cdot R_h \tag{2.9}$$

where μ_{dyn} is dynamic viscosity of air, L, w, h, and r are length, width, height, and radius of the fluidic channel. ΔP is the pressure difference whereas Q is the flow rate.

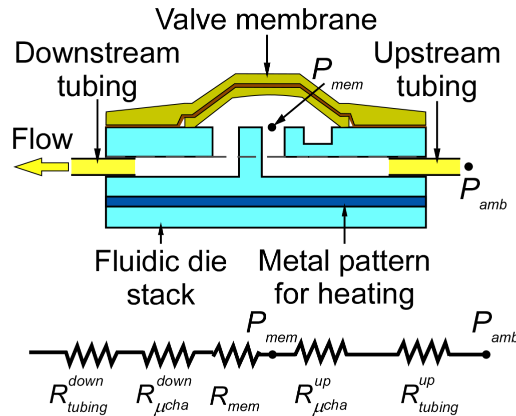

Fig. 2.22: The equivalent fluidic circuit of the flow path of the VM2.

The flow path includes two microchannels, valve membrane area, and two external capillary tubing. The flow resistances of the capillary tubing and microchannels can easily be estimated using eqn (2.3) and (2.4). The microchannels have a tapered sidewall off vertical due to

the fabrication process. Therefore, an estimated average width is used for calculating the flow resistance in microchannels. To calculate the flow resistance of the membrane area, it is approximated as a rectangular fluidic channel. At valve opening, the channel width is the perimeter of the valve seat as the flow is coming from the center port, the channel length is the width of valve seat as the flow travels across the valve seat, and the channel height is the displacement of the actuator.

The dimensions of the right microvalve in Fig. 2.21b and the estimated flow resistance of each flow path are summarized in Table 2.4. When an external capillary tubing with an ID of 250 µm is used, the total flow resistance is dominated by the external tubing because the tubing diameter is smaller than the heights of the membrane area and the microchannels. However, when an external capillary tubing with an ID of 530 µm is used, the flow resistance is no longer limited by the external tubing. This indicates that the ID of the external tubing creates a huge impact on the flow resistance and pressure distribution. With the same flow rate supplied to the valve, by using a 530-µm ID tubing, the pressure difference between P_{mem} and P_{amb} can be reduced by ≈84.6%, which is significant.

Table 2.4: Dimensions and calculated flow resistances of all the flow paths.

	Length (mm)	Width (µm)	Height (µm)	Est. Flow Resistance (kPa/sccm)
Upstream microchannel	10.2	400	420	2.3×10^{-2}
Downstream microchannel	19.4	400	420	3.7×10^{-2}
Membrane area	0.4	≈2510	560	3.8×10^{-6}
Capillary Tubing with Φ250	60	Φ250	Φ250	0.187
Capillary Tubing with Φ530	60	Φ530	Φ530	9.3×10^{-3}

2.3.2 Fabrication and assembly

The fabrication process of the fluidic die stack of VM2 is the same as VM1 (Fig. 2.11). The valve seats, through holes, and fluidic channels on the top die and middle die are created by

sandblasting (provided by Ikonics® Corporation, Duluth, MN, USA), whereas the Ti/Pt layer on the bottom die is created by evaporation and lift-off process (provided by SenPlus, Inc., Gyeonggi-do, Korea). Only three lithographic masks are used in the whole fabrication process. The three dies are bonded by epoxy (Epotek 377, Epoxy Technology Inc., Billerica, MA, USA) to form a fluidic die stack. The footprints of the fluidic die stack of the 2-valve VM2 and 3-vlave VM2 are 2.5×1.2 cm^2 and 4.0×1.2 cm^2, respectively (Fig. 2.23).

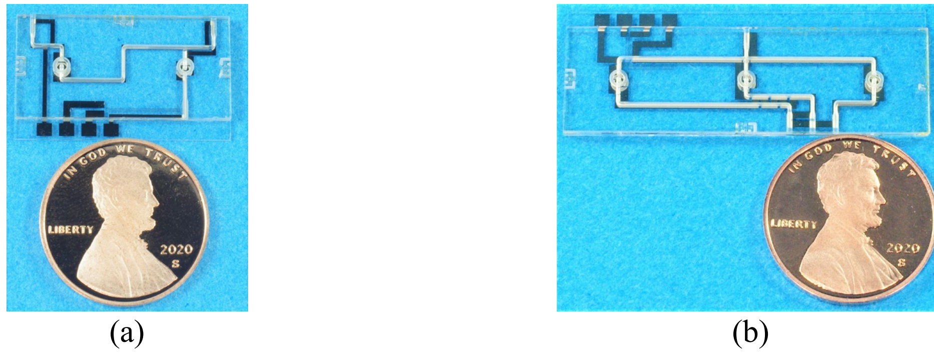

Fig. 2.23: (a) A photograph of the fluidic die stack of the 2-valve VM2. (b) A photograph of the fluidic die stack of the 3-valve VM2.

Two layers of the polyimide membrane are combined using its own adhesive. To facilitate alignment, a laser-engraved pattern is created on the top side of the upper layer. The outer circular pattern is for the alignment of the lower membrane whereas the inner circular pattern is for the alignment of the double-sided adhesive (Fig. 2.24a). The plunger connector as well as the two-part housing are machined by CNC process to provide a better surface quality (Fig. 2.24b and Fig. 2.25) (provided by Proto Labs, Inc., Maple Plain, MN, USA). Owing to the better surface quality, the two-part housing is semi-transparent, which allows visual observation of actuator operation. This assists the assembly and testing process. Each assembled device is attached to a custom PCB via screws and nuts (Fig. 2.26). The assembled 2-valve VM2 and 3-valve VM2 have sizes of $3.9 \times 2.7 \times 4.5$ cm^3 and $5.5 \times 2.7 \times 4.5$ cm^3, respectively.

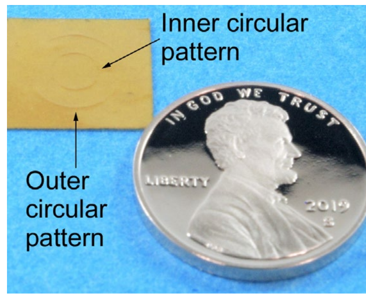

(a)

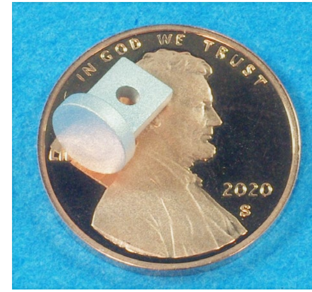

(b)

Fig. 2.24: (a) The laser-engraved upper polyimide membrane. (b) The CNC-machined plunger connector.

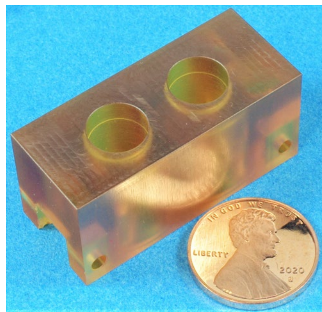

(a)

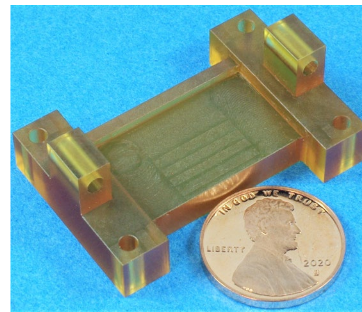

(b)

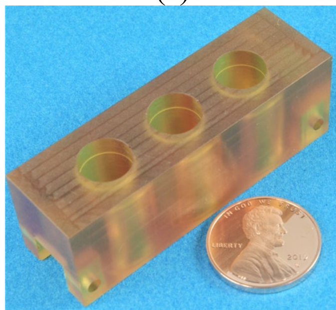

(c)

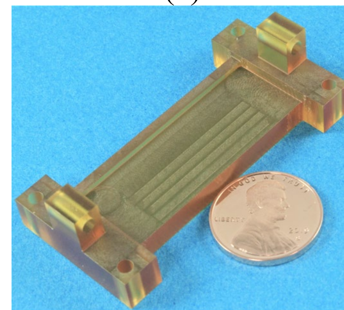

(d)

Fig. 2.25: (a) A photograph of the upper housing of the 2-valve VM2. (b) A photograph of the lower housing of the 2-valve VM2. (a) A photograph of the upper housing of the 3-valve VM2. (b) A photograph of the lower housing of the 3-valve VM2.

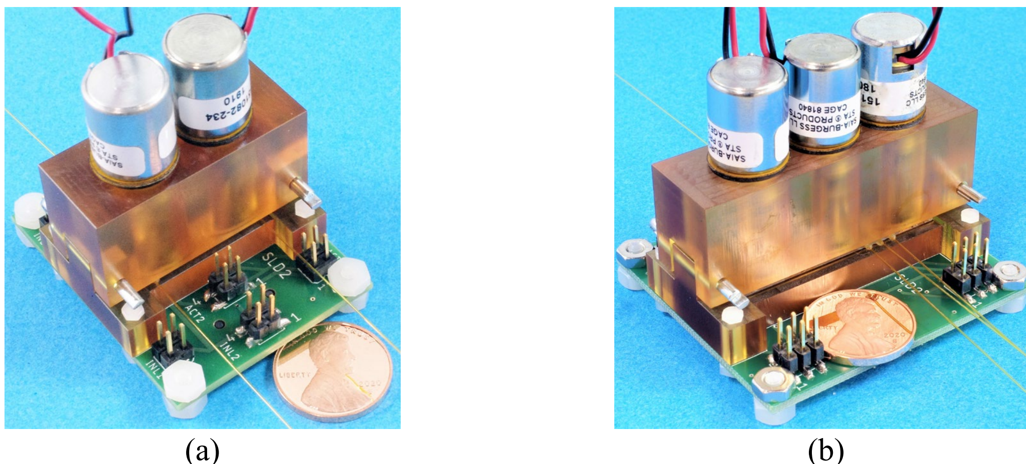

(a) (b)

Fig. 2.26: Photographs of the assembled valve modules mounted onto custom PCBs. (a) The 2-valve VM2. (b) The 3-valve VM2.

2.3.3 Experimental results

A. Lifetime Results

The lifetime of the microvalve was evaluated using a test setup that can provide bi-directional flow while measuring the flow rates through the microvalve and the corresponding pressure drops (Fig. 2.27). Two sets of pumps (NMP03KPDC-L, KNF Neuberger, Inc., Trenton, NJ, USA), differential sensors (MPXV5010DP, NXP, Austin, TX, USA), and flow meters (FMA 1603A & 1601A, Omega Engineering, Inc., Norwalk, CT, USA) were used. One set was used to provide and measure air flow in the positive regime whereas the other set was used to provide and measure air flow in the negative regime. To switch the direction of air flow, a three-way valve (LHLA1231211H, The Lee Company, Westbrook, CT, USA) was needed. The flow rate was tuned into a range that was typically used in a μGC system using capillary loads. The control of pumps and valves, including COTS three-way valve and microvalve, and data collection were implemented via a LabVIEW software program.

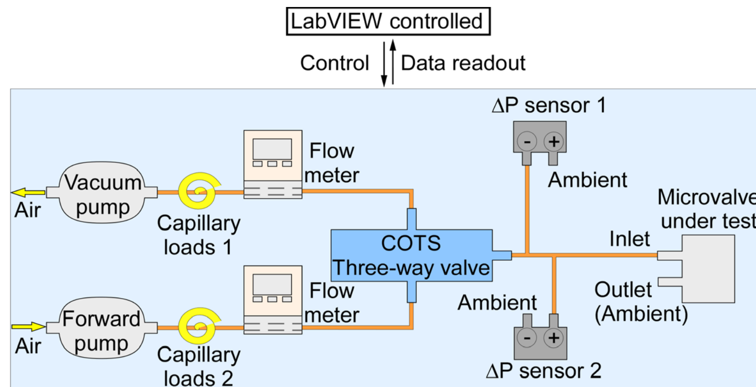

Fig. 2.27: The test setup for evaluating the lifetime of the microvalve.

The lifetime was tested by cyclical operation. In the preliminary lifetime tests, only uni-directional flow was supplied (*i.e.*, switching of three-way valve was not required). This helped in identifying failure modes if there were any. In one cycle, the microvalve was opened for 10 minutes, and then closed for another 10 minutes. In the last 30 s of opening, the microvalve was heated to 75°C by the embedded flow heater. A total of 60 testing cycles, which were equivalent to 40 hours, were conducted. Three microvalves assembled using different thickness of adhesive foam were tested: Microvalve1 was assembled with a 25-mil thick adhesive foam, Microvalve2 was assembled with a 42-mil thick adhesive foam, and Microvalve3 was assembled with a 62-mil thick adhesive foam. The measured temperature and flow rate in positive pressure regime and negative regime of Microvalve1 were shown in Fig. 2.28a and b, respectively. The results of Microvalve2 and Microvalve3 can be found in Fig. 2.29 and Fig. 2.30. For all three valves, 8.5 sccm was supplied in the positive pressure, and 5.9 sccm was supplied in the negative pressure regime. When Microvalve1 was subjected to the flow in the positive pressure regime, it showed no failures in the open state. However, leakages were found when Microvalve1 was in the closed state. This was caused by the positive pressure from the flow that was pushing against the valve membrane. Microvalve1 had no failures when the supplied flow was in the negative pressure regime. Both Microvalve2 and Microvalve3 revealed no issues for flow in both positive and

negative regimes in both open and closed states. These results indicate that sufficient thickness of the foam is required to provide a reliable seal. Furthermore, the valve with revised structure can be heated to 75°C with a flow in the negative pressure regime, which resolved the failure mode that was identified in VM1.

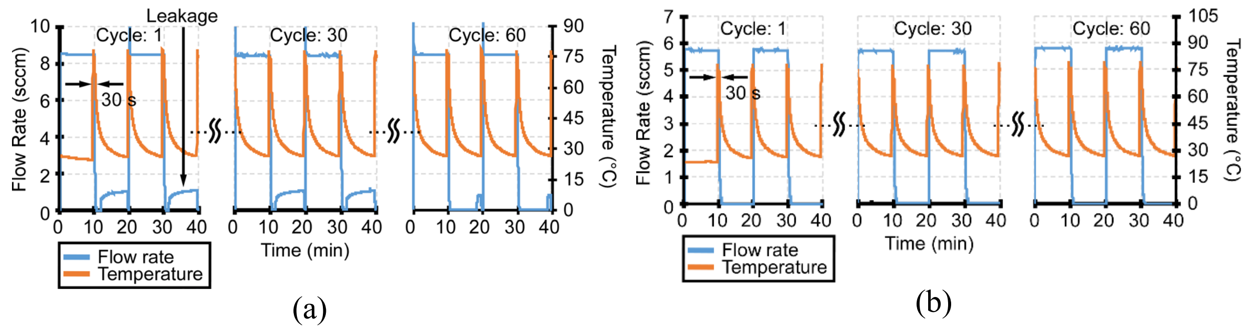

Fig. 2.28: Measured flow rates and temperatures of Microvalve1 in the preliminary lifetime results. (a) The supplied flow was in the positive pressure regime. (b) The supplied flow was in the negative pressure regime.

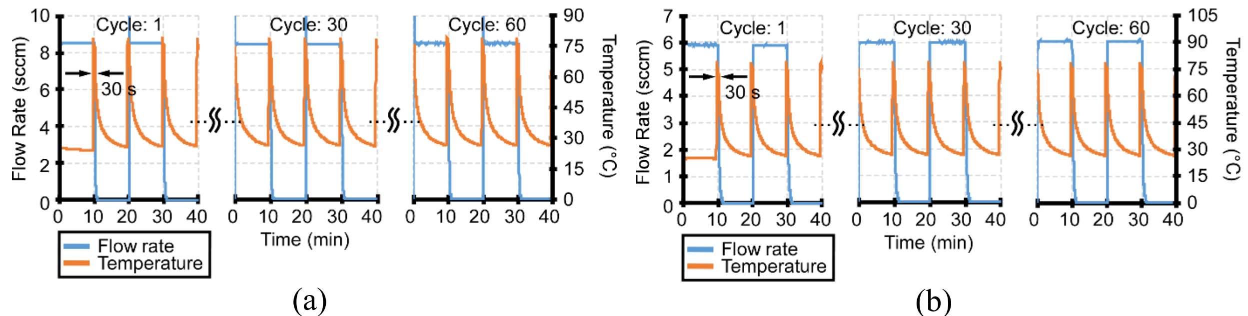

Fig. 2.29: Measured flow rates and temperatures of Microvalve2 in the preliminary lifetime results. (a) The supplied flow was in the positive pressure regime. (b) The supplied flow was in the negative pressure regime.

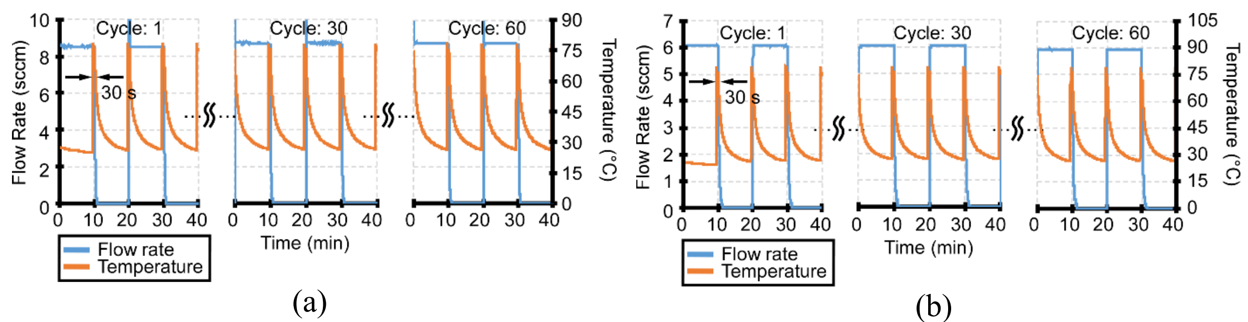

Fig. 2.30: Measured flow rates and temperatures of Microvalve3 in the preliminary lifetime results. (a) The supplied flow was in the positive pressure regime. (b) The supplied flow was in the negative pressure regime.

After testing the adhesive foam with different thicknesses based on the lifetime of the microvalve, Microvalve3, of which the adhesive foam had the largest thickness (*i.e.*, 62 mil) among the three tested microvalves, was selected and tested for a longer period with more thorough testing conditions. In the long-term evaluation, during each testing cycle, the microvalve was tested with bi-directional flow in open and closed states. The testing conditions included four stages: (i) microvalve open in the negative pressure regime, (ii) microvalve closed in the positive pressure regime, (iii) microvalve closed in the negative pressure regime, and (iv) microvalve open in the positive pressure regime. In the last 30 s of the open state, *i.e.*, stage (ii) and (iv), the microvalve was heated to 75 °C (Fig. 2.31). The flow rate through the microvalve was 1.0 sccm in the positive regime, represented separation flow, and 7.3 sccm in the negative regime, represented the sampling flow. The tests revealed a lifetime >720 cycles over a duration of 480 hours without any degradation in performance.

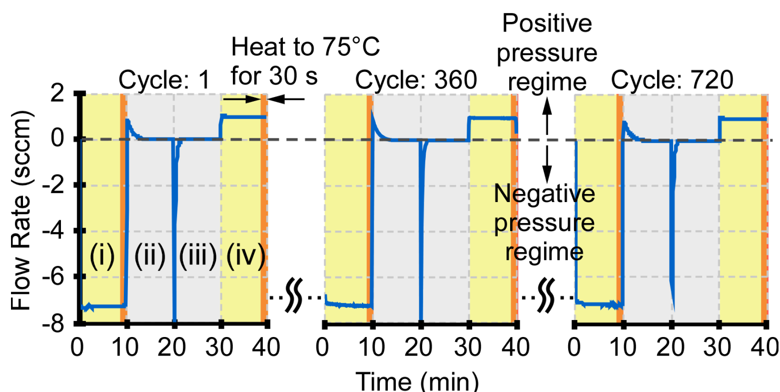

Fig. 2.31: Cycling lifetime test of the microvalve. The sudden change of flow rate at t = 20 minute resulted from an imposed reversal of flow direction.

B. Integration with MPCA1.0 µGC

To evaluate the impact of the VM2 within the context of µGC[2], the 2-valve VM2 and 3-valve VM2 were fluidically connected with a monolithic µGC chip that implemented the MPCA,

[2] This work was performed in collaboration with Ms. Weilin Liao, Mr. Xiangyu Zhao, Mr. Declan Winship, Mr. Qu Xu, Dr. Irene Lara Ibeas, and Dr. Yutao Qin

which was an enhanced architecture based on progressive cellular architecture, with 3 cells (Fig. 2.32). The 2-valve VM2 controlled the sampling flow (*i.e.,* labelled as sampling microvalve module in Fig. 2.32), whereas the 3-valve VM2 controlled the separation flow (*i.e.,* labelled as separation microvalve module in Fig. 2.32). The MPCA incorporated arrays of detectors with different sensing mechanisms to provide high orthogonality for analytes detection and identification. Two types of capacitive detectors (CapDetA and CapDetB) and one arrayed photoionization detector (AiPD) were used for each cell. This chip was named the MPCA1 chip. The details of the MPCA1 chip are described in Chapter 3. The MPCA1 chip was combined with sampling microvalve module, separation microvalve module, and a bi-directional pump module to form a microscale gas chromatograph – the MPCA1.0 μGC.

With the 2-valve module being maintained at 70°C when the surface-adsorptive analytes passed through, which was the end of sampling, the MPCA1.0 μGC successfully analyzed a vapor mixture of 22 analytes (Table 2.5) including alkanes (pentane, hexane, heptane, octane, nonane, decane, undecane, dodecane), aldehydes (butanal, pentanal, hexanal), ketone (acetone), aromatics (benzene, toluene, ethylbenzene, m-, p- and o-xylenes, mesitylene, naphthalene), and phosphonate esters (DMMP, DEMP, and diisopropyl methylphosphonate [DIMP]) with a nominal concentration of 100 ppb. The chromatograms generated by AiPDs in Cell2 and Cell3 were provided (Fig. 2.33b). Blank runs (*i.e.*, no analytes supplied to the MPCA1.0 μGC) with the same sampling duration were conducted right before and right after the actual test (Fig. 2.33a and c). These blank runs provided a benchmark for comparison as well as proved that the MPCA1.0 μGC remained operational after the test. The detector responses were not the focus of this work, but chromatograms generated by the CapDetAs in Cell2 and Cell3 were provided to show that phosphonate esters can be detected and separated by MPCA1.0 μGC with the presence of the

sampling microvalve module (Fig. 2.34). Further discussions on the detector response pattern can be found in [Lia21b].

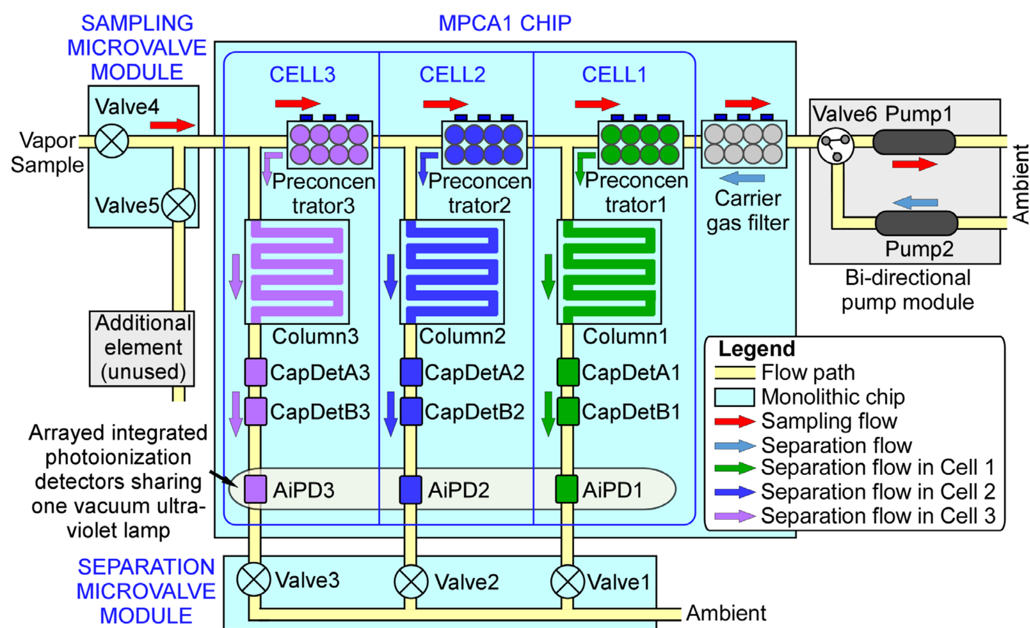

(a)

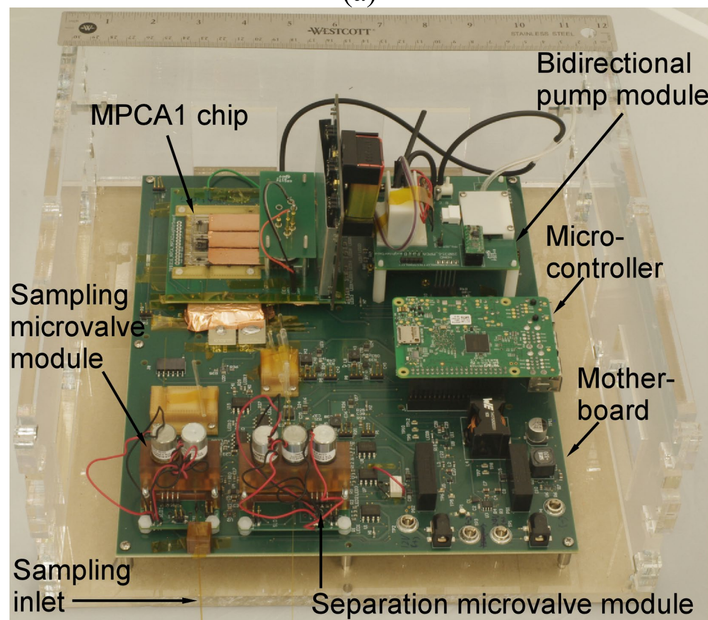

(b)

Fig. 2.32: (a) Architecture of MPCA1.0 μGC. (b) A photograph of the MPCA1.0 μGC.

Table 2.5: List of 22 tested analytes and their Kovats RI.

Compound	Kovats RI	Label	Compound	Kovats RI	Label
Acetone	475	-	m-Xylene /p-Xylene	853 859	9
Pentane	500	-	o-Xylene	862	10
Butanal	600	1	Nonane	900	12
Benzene	647.5	2	Mesitylene	956	13
Pentanal	674	3	DEMP	975	15
Heptane	700	4	Decane	1000	14
Toluene	755.4	5	DIMP	1073	16
Hexanal	769	6	Undecane	1100	17
Octane	800	7	Naphthalene	1170	18
DMMP	839	11	Dodecane	1200	19
Ethylbenzene	854	8			

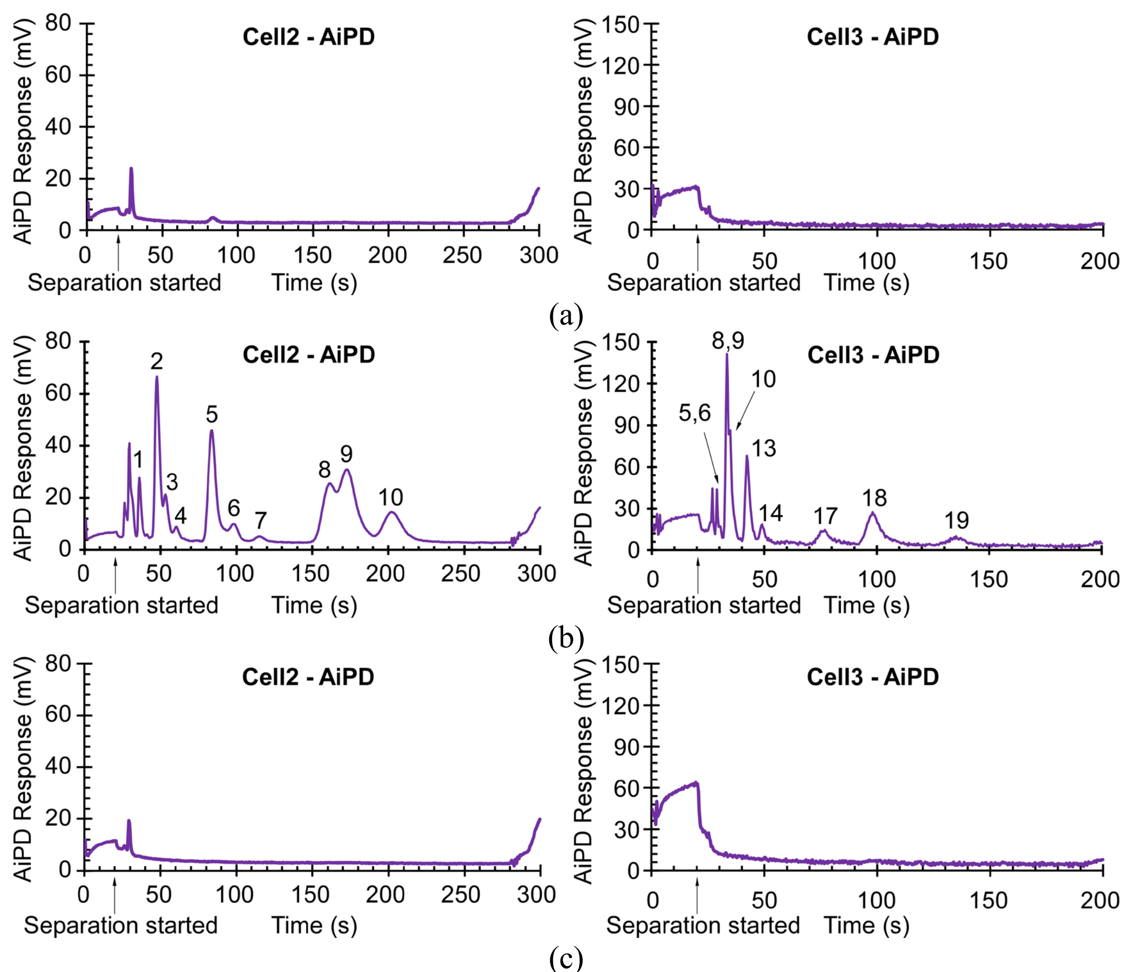

Fig. 2.33: (a) The chromatograms generated by the AiPDs before the sample injection, showing the baseline of the signal. (b) The chromatograms generated by the AiPDs in Cell2 and Cell3. (c) The chromatograms generated by the AiPDs after the sample injection, showing the baseline of the signal.

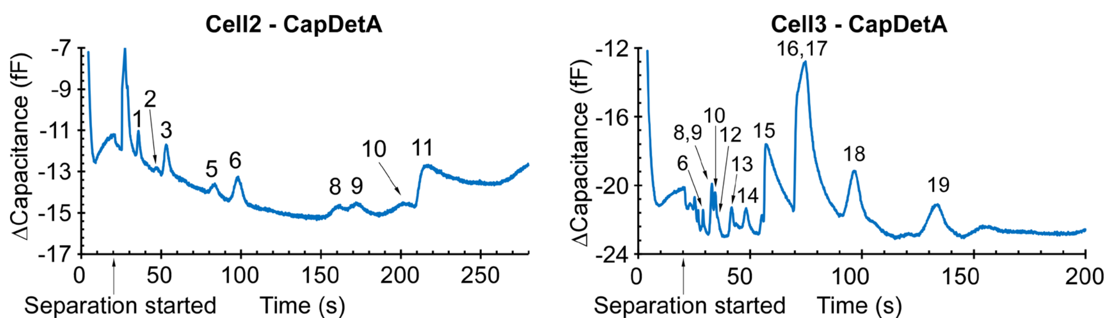

Fig. 2.34: The chromatograms produced by the CapDetAs in Cell2 and Cell3.

2.4 Discussion and Conclusion

The microvalve has provided a high open-close ratio of flow conductance of 3.46×10^3 and a large flow conductance of 4.15 sccm/kPa (*i.e.*, a flow resistance of 0.24 kPa/sccm) in the open state. Unlike many microfabricated valves, where the low flow conductance was primarily constrained by the membrane displacement that can be generated by the actuators (*e.g.*, [Sho91, Rob98, Rob03, Bae07]), the solenoid actuators that have been used in this work provide a large displacement of 560 µm, and do not limit the flow conductance. This suggests that the flow conductance can be further increased by increasing the hydraulic diameters of the fluidic channels and external capillary tubing. The simplicity of the fabrication is reflected in the number of lithographic masks; additionally, no bonding step is necessary. Table 2.6 compares multiple gas valves; this work requires only three lithographic masks, and uniquely possesses the feature of embedded flow heating that is required for µGC applications. The embedded flow heating has been proven to be necessary for analyzing highly surface-adsorptive analytes. Compared to our prior work [Lu18], which required only two masks, the additional mask used for the valve described in this section was used to fabricate the embedded flow heater. Additionally, this valve provided an excellent open-close ratio. However, the microvalves suffered from minor leakage (0.0012 sccm/kPa) in the closed state. One possible reason is a misalignment between the soft

post and actuator, which could cause non-uniform force distribution and, consequently, leave a gap between the valve membrane and valve seat. The use of appropriate alignment jigs and tools in the assembly process may alleviate this issue.

Table 2.6: Comparison of some gas microvalves.

Reference	Type[2]	Dimension per valve (mm^3)	Open-Close Ratio	Power (J/switch)	Masks	Embedded flow heating
This work	2-way EM[3]	53×17×15	3.46×10^3	0.27	3	Yes
Lu18[1]	3-way PE	30×30×10	3.68×10^3	7.8×10^{-4}	2	N/A
Par08	2-way PE	10×10×10	9.89×10^3	2.3×10^{-3}	5	N/A
Gro15	2-way PE	40×40×15	9.46×10^2	2.0×10^{-5}	3	N/A
Fu03	2-way EM	10×10×4.3	3.70×10^2	6.4×10^{-2}	Molding	N/A
Yan04	2-way ES	4.1×3.3×0.8	1.52×10^2	7.6×10^{-7}	9	N/A
Bae07	2-way ES	-	1.06×10^4	5.0×10^{-8}	7	N/A

1. Additional work that is reported in Appendix A
2. PE: Piezoelectric; EM: Electromagnetic; ES: Electrostatic
3. Bi-stable solenoid actuators (*i.e.,* consume no power in latching states)

The power consumed for actuation is also compared in Table 2.6. Although the reported microvalve consumed 0.27 J/switch, it consumed no power in the latched states, which saved substantial energy. For μGC applications, because frequent switching is not required, this is acceptable. The main power consumption of the microvalve resulted from the embedded flow heating. For maintaining the microvalve at 75°C, as necessary for accommodating certain analytes, the required embedded flow heating power is 1.0 W.

In conclusion, this chapter has reported two generations of monolithic multi-valve modules that combine microfabricated valve seats, fluidic microchannels, heaters, and thermistors with prefabricated valve membranes and actuators. The integration of microfabricated components and commercially available components has eliminated the need to fabricate thin suspended valve membranes, which simplifies the fabrication and improves the robustness. These features enable the incorporation of the multi-valve modules into μGC systems [Lia21a, Lia21b]. The microvalve

module was tested with polar and non-polar species of VOCs in standalone form and it provided chromatograms with almost no peak distortion when embedded flow heating is used. The superior chemical resistance and embedded flow heating capability of the microvalve module were also confirmed as being extremely necessary and critical for μGC systems, especially for those targeting a wide-range analysis; the chemical resistance of the unheated COTS valve was shown to cause significant peak distortion. Furthermore, the performance of these valve modules was evaluated within the context of a μGC system that has demonstrated a chromatogram of 22 non-polar and polar analytes. For future work, the multi-valve module can be further miniaturized by using smaller solenoid actuators with modifications on the fluidic die stack and 3D printed housing. If superior chemical inertness is desired, a deactivation process can be performed to further reduce the interaction between the wetted surfaces and the analytes.

Chapter 3:

A Flow Management Method For A Microscale Gas Chromatograph Eliminating Sample Inlet Valve

This chapter investigates a flow management method that is able to navigate gas flow between a sampling flow path and multiple separation flow paths while eliminating the usage of a high-performance valve at the sample inlet. Such a method significantly reduces the overall complexity and assembly ease while increasing the reliability of a microscale gas chromatography (μGC) system while permitting the analysis of highly surface-adsorptive analytes, such as phosphonate esters. This flow management method is firstly validated in a preliminary evaluation, and later demonstrated on a μGC system that integrates a monolithic μGC chip, a flow restrictor, and multiple valves and pumps. By placing all the valves downstream of the detectors and using two pumps for separation, bi-directional flow can be provided in the preconcentrators without the need of a sample inlet valve. Chromatograms of alkanes, aromatics, and phosphonate esters are generated to demonstrate the feasibility of this flow management method.

3.1 Introduction

In conventional microscale gas chromatographs, valves are commonly used to switch flow between the sampling path and the separation path. The locations of these valves are carefully designed to avoid the flow path of sample injection, separation, and detection in a μGC architecture. However, a valve is often needed at the sample inlet of a microscale gas chromatography (μGC) system to allow the entrance of analytes during sampling and block the sample inlet during separation [Kim11, Col14, Gar15, Lee16, Zho16, Wan18]. The sample inlet valve needs to have superior chemical inertness and embedded flow heating to prevent highly surface-adoptive analytes, such as phosphonate esters, from being retained within the valve during sampling [Lu21]. These phosphonate esters have high polarity that causes strong surface adsorption on surfaces along the flow path. Consequently, these analytes can easily present abnormal responses or even become undetectable.

The necessity of superior chemical inertness and embedded flow heating was validated by the chemical injection test results presented in Chapter 2. In these tests, a microvalve with superior chemical inertness and embedded flow heating was compared against an unheated commercial off-the-shelf (COTS) valve. Each valve under test was connected in series with a separation column and a flame ionization detector (FID) (Fig. 2.17). A highly surface-adsorptive analyte, diethyl methylphosphonate (DEMP), was injected into the valves. As shown in Fig. 3.1, when the microvalve was heated to 80°C using the embedded flow heating, the DEMP was detected without noticeable broadening and distortion. Nonetheless, when the unheated COTS valve was tested, the DEMP was not detected by the FID, indicating that the unheated COTS valve severely retained the DEMP, and virtually eliminated the chromatographic peak. If an unheated COTS valve is

placed at the sample inlet of a μGC system, the unheated COTS valve may retain the highly surface-adsorptive analytes, and potentially constrain the application of a μGC system.

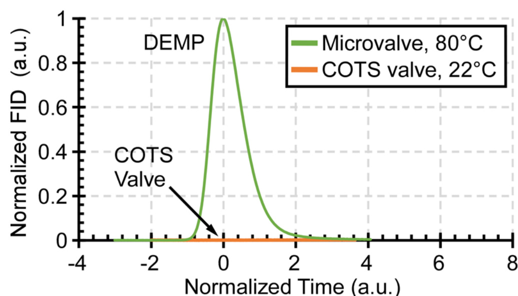

Fig. 3.1: The DEMP peak generated by a FID when a heated microvalve and an unheated COTS valve were tested, respectively.

Although the sample inlet valve should ideally possess superior chemical inertness and embedded flow heating, the fabrication and assembly, fluidic connection, and reliability are the trade-offs of using such high performance microvalves. If the sample inlet valve is absent, an undesired outgoing or incoming flow can occur during separation. Consequently, this causes sample loss or sample intake that introduces contaminants or moisture from ambient to the system. To overcome this dilemma, many μGC systems adopted valveless architectures to avoid the use of valves. For the architecture of single flow path with the use of uni-directional flow [Gor12, Qin14a], the preconcentrator was limited to a single type of sorbent; for the architecture of single flow path with the use of bi-directional flow, the analyte samples might be retained in the column during sampling [Qin14b, Qin15b, Qin16].

This chapter reports a flow management method that permits bi-directional flow in the preconcentrators while eliminating the sample inlet valve and maintaining high analytical performance. By circulating the separation flow using a single pump, the valve used to block the sample inlet during separation is not needed. A flow restrictor, which provides a modest flow resistance, is incorporated at the sample inlet to minimize any undesired flow. This concept is validated in a preliminary evaluation using a setup that emulates a simplified μGC architecture.

In the system implementation, instead of using a single pump to circulate the separation flow, two pumps that are located at upstream and downstream of the separation path are used. This prevents the exhausts of analytes from being redirected back to the system and potentially degrading the analytical performance. By conducting fluidic analysis and adjusting pump operations, the configuration of two pumps is equivalent to the configuration of single pump that circulates the flow. The undesired outgoing or incoming flow during separation can be fully eliminated. This flow management method is implemented in a μGC system, MPCA1.1 μGC, that adopts multi-sensing progressive cellular architecture (MPCA) and can be further applied to other typical μGC systems.

The concept evaluation and system-level demonstration are described in Section 3.2, the experimental results are presented in Section 3.3, and followed by the discussion and conclusion in Section 3.4.

3.2 Concept Evaluation and System-level Demonstration

3.2.1 Concept Evaluation

In a typical μGC system, bi-directional flow is provided by a sampling pump, a separation pump, and a three-way valve that selects between the two pumps (Fig. 3.2a). To prevent the undesired outgoing or incoming flow through the columns during sampling, a valve downstream of the separation path is needed. This valve can be placed further downstream of the detector, and thus not require superior chemical inertness and embedded flow heating. To prevent the undesired outgoing or incoming flow through the sample inlet during separation, a sample inlet valve with high performance is generally needed. The function of the sample inlet valve can in principle be replaced by a flow management method that uses the separation pump to circulate the flow from

the separation outlet to the separation inlet (Fig. 3.2b). In this manner, the gas flows through the three-way valve, preconcentrator, column, detector, separation valve, and back to the separation pump. Assuming an ideal pump, the flow rates through these components should be the same, implying no flow in the path of sample inlet. A flow restrictor can be incorporated at the sample inlet to minimize the undesired flow in the transient state.

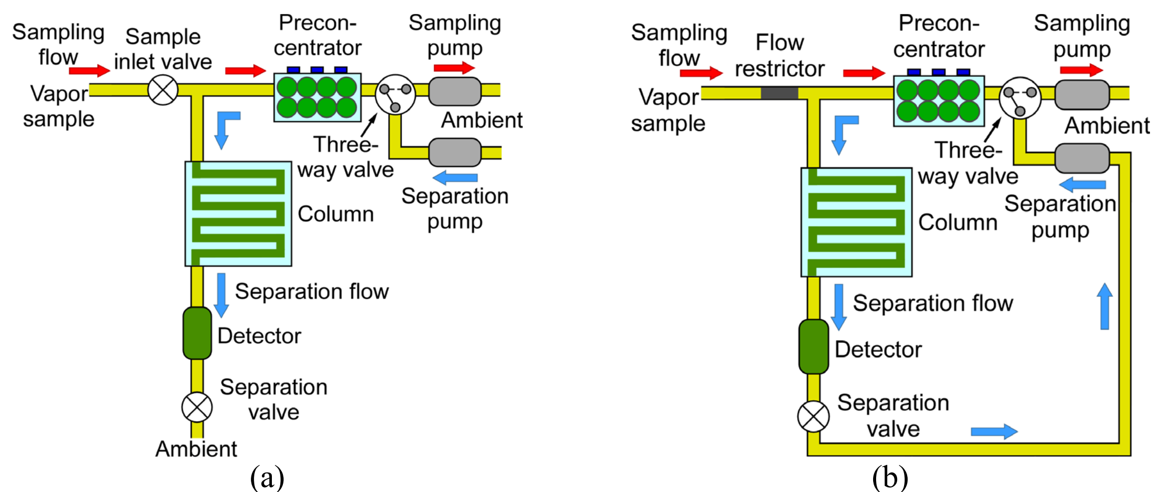

Fig. 3.2: (a) Conventional μGC architecture. (b) Flow management method that circulates the separation flow and replaces the sample inlet valve with a flow restrictor.

To evaluate the concept, a preliminary experimental evaluation was conducted. To mimic the separation scenario of a general μGC system, a fluidic setup that represented a simplified μGC architecture was built. The test setup included a separation pump (mp6, Bartels Mikrotechnik GmbH, Dortmund, Germany), a tee connector, three flow meters (FMs) (MW-10SCCM-D & MW-20SCCM-D, Alicat Scientific, Inc., AZ, USA; FMA 1603A, Omega Engineering, Inc., Norwalk, CT, USA), and two flow loads (*i.e.*, capillary tubes with a diameter of 250 μm and different lengths) was used (Fig. 3.3a). The flow rates through the three paths, the upstream separation path, the downstream separation path, and the path of sample inlet, were constantly monitored by the FMs. The Flow load1, which represented the flow restrictor, had a flow resistance of 0.25 kPa/sccm, whereas the Flow load2, which represented the preconcentrator, had a flow resistance of 1.00

kPa/sccm. The test was conducted at room temperature using ambient air as the medium. When the separation pump was activated to provide the flow, after reach the steady state, both FM2 and FM3 measured flow rates of ≈0.60 sccm, whereas FM1 measured zero flow. This validated the concept of using one separation pump to circulate the flow. However, before reaching the steady state, a transient flow rate was measured by FM1 (Fig. 3.3b). The transient flow was presented as an incoming flow that lasted for ≈4.5 s and had a peak flow rate of 0.35 sccm. Estimated by the steady state flow rate and separation duration, the volume of the underside flow was 0.5% of the total flow volume when the separation lasted for 5 minutes.

The impact of the distribution of flow resistance was also evaluated. When the Flow load2 was moved to the downstream separation path, the steady state responses of the three FMs remained unchanged. Nonetheless, it was observed that the direction of the undesired transient flow changed. In this case, FM1 measured an outgoing flow during the transient state.

Such transient flow is caused by the activation of pump and can lead to a split or dilution of the preconcentrator desorption flow. This issue can be resolved by heating the preconcentrator after the separation flow stabilizes, however, this places stringent requirements on the heating ramp rate of the preconcentrator. The heating requirements of the preconcentrators and other μGC components are described in Chapter 5.

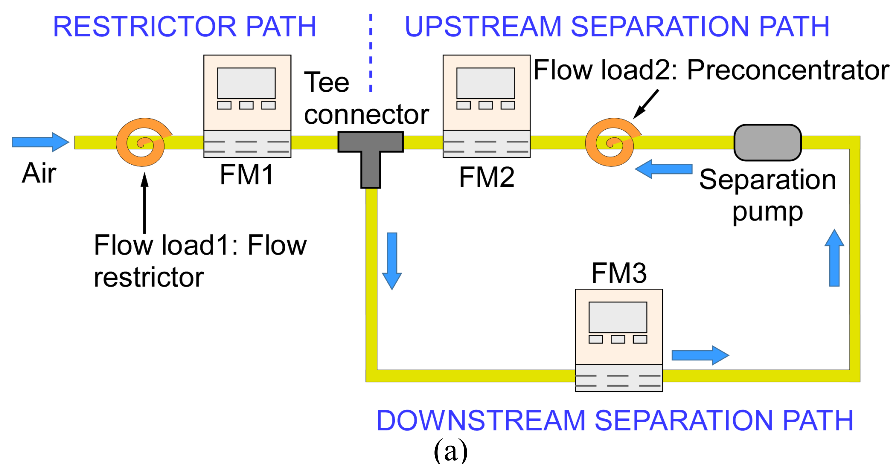

(a)

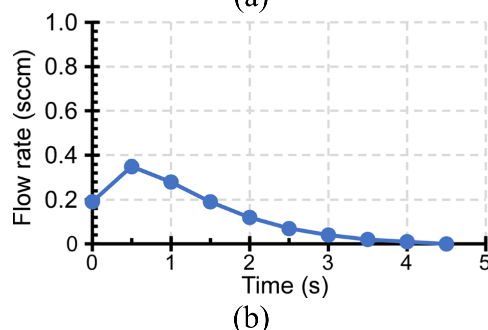

(b)

Fig. 3.3: (a) The test setup of the preliminary experimental evaluation. (b) The transient flow rates measured by FM1.

3.2 2 System-level Demonstration

A. Fluidic architecture and operation

In a μGC implementation[3], using one separation pump to circulate the separation flow can eliminate the sample inlet valve. However, in addition to the concerns described in Section 3.2.1, this method has the concern of redirecting the exhausts of analytes back to the system. Although a filter can be incorporated to provide clean carrier gas during separation, constantly supplying exhaust to the system is still not desired. Instead of using a single pump to circulate the separation flow, this issue is addressed by dividing the single separation pump into two separation pumps,

[3]The system integration and chromatograms acquisition were performed by Ms. Weilin Liao and Dr. Irene Lara Ibeas. The hardware electronics was investigated by Mr. Xiangyu Zhao and Mr. Declan Winship. The control software was investigated Mr. Qu Xu.

one locates at the upstream separation path and the other one locates at the downstream separation path (Fig. 3.4a). By adjusting the operations of the two separation pumps, the undesired flow in the path of sample inlet can be eliminated. Essentially, the two configurations (*i.e.,* two separation pumps versus one separation pump that circulates the flow) are equivalent. The theoretical fluidic analysis is performed and described in the next section.

The flow management method is applied in a μGC system, named MPCA1.1 μGC (Fig. 3.4b), that consists of a monolithic μGC chip (MPCA1 chip), a pumps/valves module, and a flow restrictor. The pumps/valves module integrates three pumps and four valves. The flow restrictor is a deactivated fused silica tube that also serves as the sample inlet. Its flow resistance is determined by the dimensions of the tube. In the sampling phase, the sampling pump is activated to provide the flow through the preconcentrators that are connected in series. Meanwhile, the three separation valves *(i.e.*, Valve1, Valve2, and Valve3) are closed. Note that the presence of the flow restrictor reduces the sampling flow rate. In the separation phase, a flow in the opposite direction is provided by activating the two separation pumps simultaneously. The flow mainly goes through the prescribed flow path (Fig. 3.4b), however, the undesired outgoing or incoming flow may still resent in the path of sample inlet. The outgoing flow could result in sample loss, whereas the incoming flow that contains moisture and contaminants could result in inaccurate analyte identification. Between the two, the incoming flow is more harmful to the analytical performance of MPCA1.1 μGC.

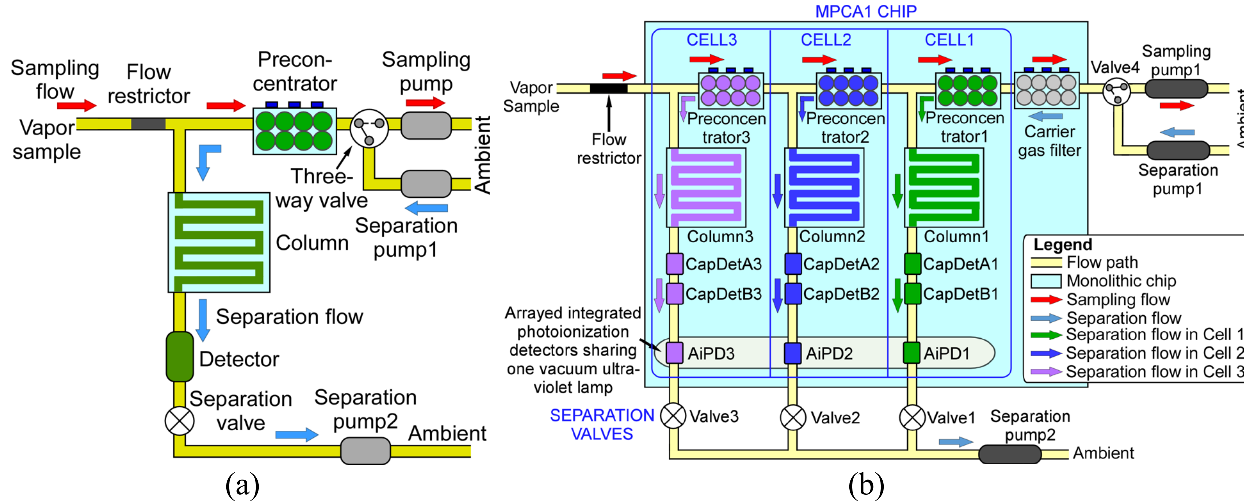

Fig. 3.4: (a) Dividing a single separation pump to two separation pumps. (b) Architecture of the MPCA1.1 μGC.

B. Analytical fluidic model

The goal of this analysis is to derive the conditions required to eliminate the potential undesired flow in the path of sample inlet when the two pumps are used for separation. An analytical fluidic model is constructed to study how distribution of pressure and flow resistance affect both the sampling and separation flow. The flow resistance of all the components, including preconcentrators, columns, carrier gas filter, and interconnecting fluidic channels are estimated. The flow resistance of the flow restrictor, columns, detectors, and interconnecting fluidic channels can be calculated by Equation (2.6) and (2.7) as they are rectangular and circular channels; the flow resistance of the preconcentrators can be calculated below [Erg52]:

$$R_h^{PCF} \approx \frac{150\mu_{dyn} \cdot L_{bed}}{d_{particle}^2 \cdot (W_{bed} \cdot H_{bed})} \frac{(1-\varepsilon^2)}{\varepsilon^3} \tag{3.1}$$

where μ_{dyn} is dynamic viscosity of air; L_{bed}, W_{bed}, H_{bed} are the length, width, and height of the sorbent bed, respectively; $d_{particle}$ is the diameter of the sorbent particle; and ε is the porosity of the

bed. The flow resistances presented by the valves in open state are negligible. The estimated flow resistance of each component is listed in Table 3.1.

Table 3.1: Estimated flow resistances of all the components within the MPCA1 chip

Component	Est. flow resistance (kPa/sccm)
Flow restrictor	0.219
Preconcentrator1	0.134
Preconcentrator2	0.073
Preconcentrator3	0.041
Carrier gas filter	0.167
Column1	1.065
Column2	0.984
Column3	0.916
Detector array with interconnecting channels	0.088

In the sampling phase, the flow rate is determined by the performance of the sampling pump and the flow resistance of the sampling path (*i.e.,* flow restrictor, three preconcentrator, and a carrier gas filter). In the separation phase, the distribution of flow is determined by the performances of the separation pumps and the flow resistances of the upstream separation path, the downstream separation path, and the path of sample inlet. To estimate the portion of the undesired flow in the path of sample inlet, an equivalent fluidic circuit of Cell3 separation is constructed.

The fluidic circuit is illustrated in Fig. 3.5, where P_{up} is the positive pressure provided by the separation pump1, P_{down} is the negative pressure provided by the separation pump2, and P_3 is the ambient pressure (*i.e.,* P_3 is assumed zero). In Cell3 separation, R_{res}^{Cell3} represents the flow resistance of the path of sample inlet, which solely includes the flow restrictor; R_{up}^{Cell3} represents the total flow resistance of the upstream separation path, which includes three preconcentrators, a carrier gas filter, and interconnecting fluidic channels; and R_{down}^{Cell3} represents the total flow

resistance of the downstream separation path, which includes Column3, detectors, and interconnecting fluidic channels.

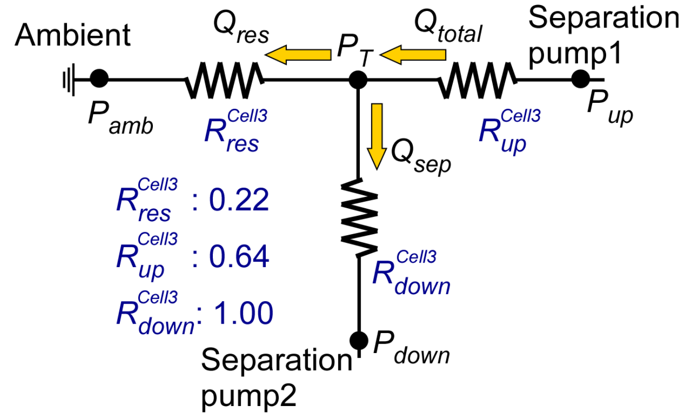

Fig. 3.5: The equivalent fluidic circuit and the flow resistances (kPa/sccm) of different flow paths in Cell3 separation.

By solving the fluidic circuits (Fig. 3.5) using Kirchhoff's rule [Bir01], the pressure at the T-junction, P_T, and the flow in the path of sample inlet, Q_{res}, can be derived.

$$Q_{res} = \frac{P_{up} \cdot R^{Cell3}_{res} + P_{up} \cdot R^{Cell3}_{down} - P_{down} \cdot R^{Cell3}_{res}}{R^{Cell3}_{up} \cdot R^{Cell3}_{res} + R^{Cell3}_{down} \cdot R^{Cell3}_{res} + R^{Cell3}_{up} \cdot R^{Cell3}_{down}} \tag{3.2}$$

$$P_T = \frac{R^{Cell3}_{res} \cdot (P_{up} \cdot R^{Cell3}_{down} + P_{down} \cdot R^{Cell3}_{up})}{R^{Cell3}_{up} \cdot R^{Cell3}_{res} + R^{Cell3}_{down} \cdot R^{Cell3}_{res} + R^{Cell3}_{up} \cdot R^{Cell3}_{down}} \tag{3.3}$$

If P_{up} and P_{down} are distributed based on the ratio of R^{Cell3}_{up} over R^{Cell3}_{down}, which are the ideal operating points of the two separation pumps, Q_{res} is theoretically zero. This means that during separation, there is no undesired flow through the path of sample inlet. This further implies that when the two pumps are operated at these ideal conditions, the configuration of two separation pumps is equivalent to the configuration of one pump that circulates the flow. However, if the performances of the pumps drift over time, which cause P_{up} and P_{down} shifting away from the ideal operating points (*i.e.,* the condition that permits zero flow in the path of sample inlet), the undesired flow of

Q_{res} occurs. For instance, if P_{up} remains unchanged and P_{down} is decreased by 20% due to the degradation of the separation pump2, without the presence of the flow restrictor, the undesired flow is 20% of the total flow. With the current value of R_{res}^{Cell3} equals to 0.22 sccm/kPa, the undesired flow is reduced to 13.5% of the total flow. If R_{res}^{Cell3} is increased to the same value as R_{down}^{Cell3}, the undesired flow of Q_{res} is only 6.1% of the total flow (Q_{total}). The relationships between the portion of Q_{res} (*i.e.*, Q_{res} /Q_{total}) and R_{res}^{Cell3} under different level of P_{down} decrement are shown in Fig. 3.6.

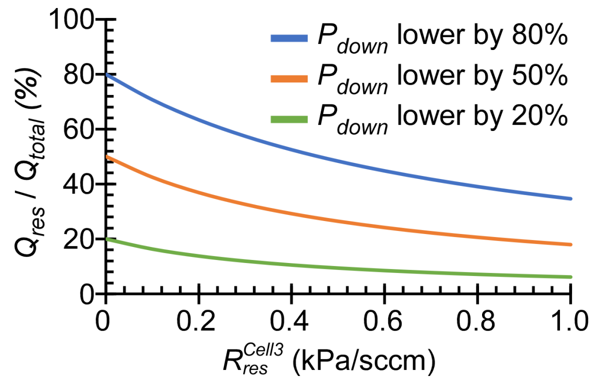

Fig. 3.6: Portion of outgoing flow versus the flow resistance of the flow restrictor.

The same fluidic model can be applied to Cell1 and Cell2 separation with modifications on the flow resistance in each flow path. In both Cell1 and Cell2 separation, the flow resistances of the path of sample inlet increase because of the additional contribution from the preconcentrators, whereas the flow resistances of the upstream separation paths decrease. The flow resistances of the downstream separation paths remain similar because they are dominated by the correspondent columns, which have similar values of flow resistances. To achieve zero flow in the path of sample inlet, the performances of the pumps need to be adjusted accordingly. The direction of the undesired flow is also determined by P_{up} and P_{down}. When P_{up} is higher than its ideal operating point (or P_{down} is lower than its ideal operating point), the undesired flow is an outgoing flow.

When P_{up} lower than the ideal operating point (or P_{down} is higher than the ideal operating point), the undesired flow is an incoming flow.

C. MPCA1 chip - µGC architecture

The MPCA1 chip implements MPCA by monolithically integrating three µGC cells within a fused silica chip (Fig. 3.4). Each cell comprises a preconcentrator, a separation column, two types of capacitive detectors (*i.e.,* CapDetA and CapDetB), and an array integrated photoionization detector (AiPD). Additionally, a carrier gas filter is integrated. The MPCA1 chip comprises a stack of two fused silica dies and an MgF_2 window. The top die is 675 µm thick, containing 180 µm deep flow channels, 500 µm deep chambers, in addition to cutouts. The 180 µm depth is for the separation columns, capacitive detectors, and on-chip fluidic interconnects; the 500 µm depth is for sorbent chambers of the preconcentrators and the carrier gas filter; whereas the cutouts are for thermal isolation, upper openings of the AiPDs, and sorbent loading ports of the preconcentrators. The bottom die is 500 µm thick, containing patterned thin-film Ti/Pt of two different thicknesses, in addition to thermal isolation cutouts. A 50/100 nm thick Ti/Pt provides sensing electrodes of the capacitive detectors, whereas another 100/200 nm thick Ti/Pt provides heaters, thermistors, and sensing electrodes of the AiPDs. The MgF_2 window covers the upper openings of the AiPDs and allows transmission of vacuum ultraviolet (VUV) radiation from the lamp.

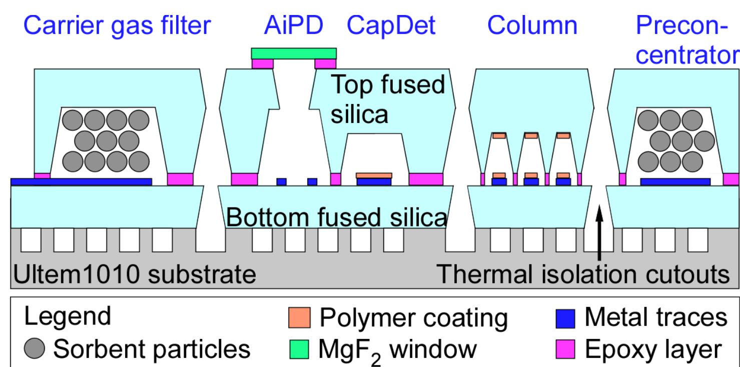

Fig. 3.7: Illustration of the cross section of the MPCA1 chip.

In the MPCA1 chip, each cell targets a specific volatility range of analytes: Cell1 targets C_3-C_5, Cell2 targets C_5-C_8, and Cell3 targets C_8-C_{12}. The sorting of the targeted analytes into the dedicated cells is provided during sampling, when the preconcentrators are connected in series. Low-volatility analytes are trapped in the upstream preconcentrators, whereas high-volatility analytes undergo breakthrough in the upstream preconcentrators and are trapped in the downstream preconcentrators. The material, volume, and mass of the sorbent in each preconcentrator are tailored. Preconcentrator3, located upstream in the sampling flow, incorporates the smallest sorbent chamber of 2.7 μL inner volume for an estimated 1.8 mg of the weakest sorbent Carbograph™ 2 (#1728, Grace Davison Discovery Science, IL, USA). Preconcentrator2, located midstream in the sampling flow, incorporates a mid-size sorbent chamber of 8.6 μL inner volume for an estimated 3.5 mg of a stronger sorbent Carbopack™ X (#10437-U, Sigma Aldrich, St. Louis, MO, USA). Preconcentrator1, located downstream in the sampling flow, incorporates the largest sorbent chamber of 15.2 μL inner volume for an estimated 7.4 mg of the strongest sorbent Carboxen™ 1003 (#10471-U, Sigma Aldrich, St. Louis, MO, USA).

The separation column in each cell is also tailored. In principle, the column length, width, height, and stationary phase material and thickness are parameters that can be tailored; in this work, only the stationary phase thickness is tailored. All three separation columns are designed as serpentine channels with 0.57 m length, 500 μm width, 180 μm height, and coated with a polydimethylsiloxane (PDMS) stationary phase. Column1, Column2, and Column3 have coating thicknesses of 10 μm, 5 μm, and 0.5 μm, respectively.

Each cell incorporates two complementary capacitive detectors, *i.e.*, CapDetA and CapDetB, and one AiPD. The CapDetA and CapDetB are coated with PDMS with a thickness of 0.4 μm and 2 μm, respectively. The CapDetA response is dominated by the PDMS swelling upon

absorption of the analytes, producing a capacitance change (ΔC) that is always positive, whereas CapDetB response is minimally dependent on PDMS swelling but dominated by the change in the dielectric constant as analytes are absorbed in the PDMS [Qin16]. Consequently, the CapDetB response can be either positive or negative, corresponding to whether the dielectric constant of the analyte is larger or smaller than that of PDMS. The AiPD generates electric current when the analyte molecules are ionized by the VUV radiation.

A carrier gas filter is integrated at the carrier gas inlet of the MPCA1 chip. The filter is designed as a U-shaped chamber with an inner volume of 6.8 µL for an estimated ≈4.9 mg of Molecular Sieve 5A (#20302, Sigma Aldrich, St. Louis, MO, USA). The filter provides scrubbed ambient air as the carrier gas for the separation by trapping moisture and vapor phase contaminants at ambient temperature. The filter can be regenerated by a short thermal pulse during sampling to desorb the trapped moisture and contaminants back into the ambient.

The MPCA1 chip is microfabricated lithographically with 6 masks. The top die is micromachined by sandblasting (Ikonics® Corporation, MN, USA) using 3 masks. On the bottom die, the Ti/Pt thin films are created by evaporation and liftoff (SenPlus Inc., Gyeonggi-do, Korea) using 2 masks, whereas the thermal isolation cutouts are created by sandblasting (Ikonics® Corporation, MN, USA) using an additional mask. The two dies and the MgF_2 window are bonded by epoxy (#377, Epoxy Technology, MA, USA). The coating of columns and capacitive capacitors use a proprietary process. All three columns are deactivated by pinacolyl methylphosphonate [Rad08]. The sorbent materials are packed into the preconcentrators through the loading ports on the top surface of the sorbent chambers. These loading ports are then sealed by an epoxy (#Stycast2850FT, Henkel, Germany). The overall footprint of the MPCA1 chip is 40.3×55.7 mm^2 (Fig. 3.8a).

D. Components integration

The MPCA1 chip is fluidically connected to a flow restrictor, and a pumps/valves module that includes four valves (#LHLA1231211H, The Lee Company, CT, USA) and three pumps. One pump provides the sampling flow (#NMP03KPDC-L, KNF Neuberger Inc., NJ, USA), and the other two pumps (#mp6-air, Servoflo Corporation, MA, USA), of which the pressure heads are electrically adjustable, provide separation flow. The flow restrictor is a fused silica tube with a diameter of 250 μm and a length of 7 cm.

The MPCA1 chip and the pumps/valves module are installed on dedicated printed circuit boards (PCBs). On the PCB for the MPCA1 chip, the MPCA1 chip is seated on a 3D-printed Ultem 1010 substrate (provided by CIdeas Inc., Crystal Lake, IL, USA), which incorporates an array of pillars. The air gap between the pillars reduces heat dissipation from the MPCA1 chip to the daughterboard, while the pillars maintain sufficient mechanical support. These PCBs and a microcontroller (#Raspberry Pi 3B, Raspberry Pi Foundation, UK) are electrically connected to a motherboard with control, power supply, and readout electronics. All these components except the laptop are placed within a 20.0 × 23.0 × 10.5 cm^3 transparent acrylic box (Fig. 3.8b).

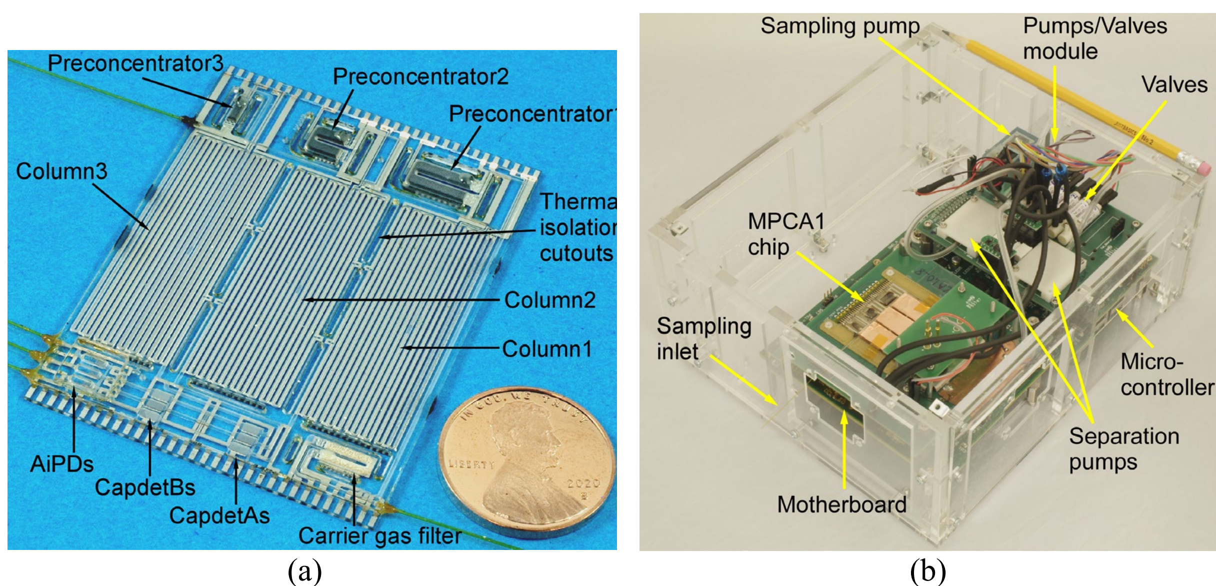

Fig. 3.8: A photograph of the (a) MPCA1 chip and (b) MPCA1.1 μGC.

3.3 Experimental Results

A typical analytical run consisted of four steps: conditioning, sampling, purging, and separation. The separation step included three substeps, each corresponding to the separation in a cell. The first step, conditioning, was used to remove any analytes that might have remained in the preconcentrators from the preceding run. During conditioning, Valve1, Valve2, and Valve3 were closed. The separation pump1 was activated to provide a flow rate of ≈2 sccm through the carrier gas filter, the preconcentrators, and the flow restrictor. Meanwhile, the preconcentrators were heated to 180°C, maintained for 30 s, then cooled down to room temperature by natural air convection.

During sampling, the sampling pump provided a flow rate of ≈25 sccm through the flow restrictor, Preconcentrator3, Preconcentrator2, Preconcentrator1, and the carrier gas filter. In the last 35 s of the sampling, the carrier gas filter was heated to 180°C to remove water molecules and any potential contamination adsorbed during the preceding run and the ongoing sampling step.

Next, the preconcentrators and columns were purged separately at ambient temperature by a flow of air supplied by the separation pumps and dried by the carrier gas filter. Such a "dry-purge" technique was reported for removing moisture while preserving analytes in the preconcentrators packed with hydrophobic sorbents [Gaw01, Fas05]. The preconcentrators were purged for 90 s in the same direction used in the conditioning step by only the separation pump1. Subsequently, the columns were purged altogether for 20 s, during which Valve1, Valve2, and Valve3 were opened, and both separation pump1 and separation pump2 were activated.

Finally, for the separation of each cell, Valve1, Valve2, and Valve3 were sequentially opened. For the control of gas flow, the separation pumps maintained a carrier gas flow rate of ≈0.4 sccm. By electrically adjusting the pressure heads of the two separation pumps, the flow rate

in the path of sample inlet was nearly zero, which was confirmed by a temporary flow meter that was connected in series with the sample inlet. To ensure that the unpredictable drift of pumping performances did not cause an incoming flow, the separation pump1 was set to have a pressure head that was slightly higher than its ideal operating point. This resulted in a minor outgoing flow of 0.04-0.05 sccm, which was acceptable. The flow rates through the preconcentrator and the column in each cell are summarized in Table 3.2.

Table 3.2: Flow rates through the preconcentrator and the column in each cell.

Flow rate	Preconcentrator (sccm)	Column (sccm)
Cell1	0.47	0.42
Cell2	0.47	0.43
Cell3	0.46	0.42

For the control of heating, during Cell1 separation, Preconcentrator1 was heated to 180°C and maintained for 15 s, whereas Column1 and the detectors were both maintained at room temperature (≈26°C). During Cell2 separation, Preconcentrator2 was heated to 180°C and maintained for 15 s. The heating of Column2 was tailored based on the analytes. For less surface-adsorptive analytes, such as alkanes, Column2 was maintained at isothermal 40°C; for highly surface-adsorptive analytes, such as phosphonate esters, Column2 was linearly ramped from room temperature to 70°C. The detectors were operated isothermally at 40°C. During Cell3 separation, Preconcentrator3 was heated to 180°C and maintained for 15 s, whereas Column3 and the detectors were operated isothermally at 60°C.

To validate the operation and evaluate the performance of MPCA1.1 µGC, two analytical runs were conducted using different vapor mixtures. The first mixture included non-polar analytes, containing hexane, heptane, octane, nonane, and decane (C_6-C_{10}), with a nominal concentration of 100 ppb for each analyte. The second vapor mixture included both non-polar and polar analytes, containing benzene, toluene, ethylbenzene, m-, p- and o-xylenes (BTEX), and phosphonate esters

(dimethyl methylphosphonate [DMMP], DEMP and diisopropyl methylphosphonate [DIMP]). The BTEX had a nominal concentration of 15 ppb whereas the phosphonate esters had a nominal concentration of 50 ppb. The selections were made to test the capability of MPCA1.1 μGC to detect a broad range of analytes with different volatilities and chemical properties.

The resulting chromatograms generated by the AiPDs in Cell2 and Cell3 were shown Fig. 3.9. Cell1 chromatograms were not provided because the volatility of the tested analytes was not within the volatility range of Cell1. In the chromatograms of alkanes, hexane, heptane, and octane were separated in Cell2; octane, nonane and decane were separated in Cell3 (Fig. 3.9a). In the chromatograms of BTEX and phosphonate esters, benzene, toluene, ethylbenzene, m-xylene, p-xylene, o-xylene, and DMMP were separated in Cell2. All the analytes were retained and separated in Cell3 (Fig. 3.9b). From the raw chromatograms, most analytes were properly separated, and produced symmetrical and narrow chromatographic peaks. However, full coelution of ethylbenzene and m-/p- xylenes occurred in both Cell2 and Cell3. A noticeable tailing was also observed for phosphonates esters. To demonstrate the unique feature of the detector arrays of MPCA1.1 μGC, the chromatograms of alkane mixture generated by the CapDetAs and CapDetBs in Cell2 and Cell3 were provided in Fig. 3.10. These chromatograms demonstrated that MPCA1.1 μGC could detect analytes with a wide range of volatility.

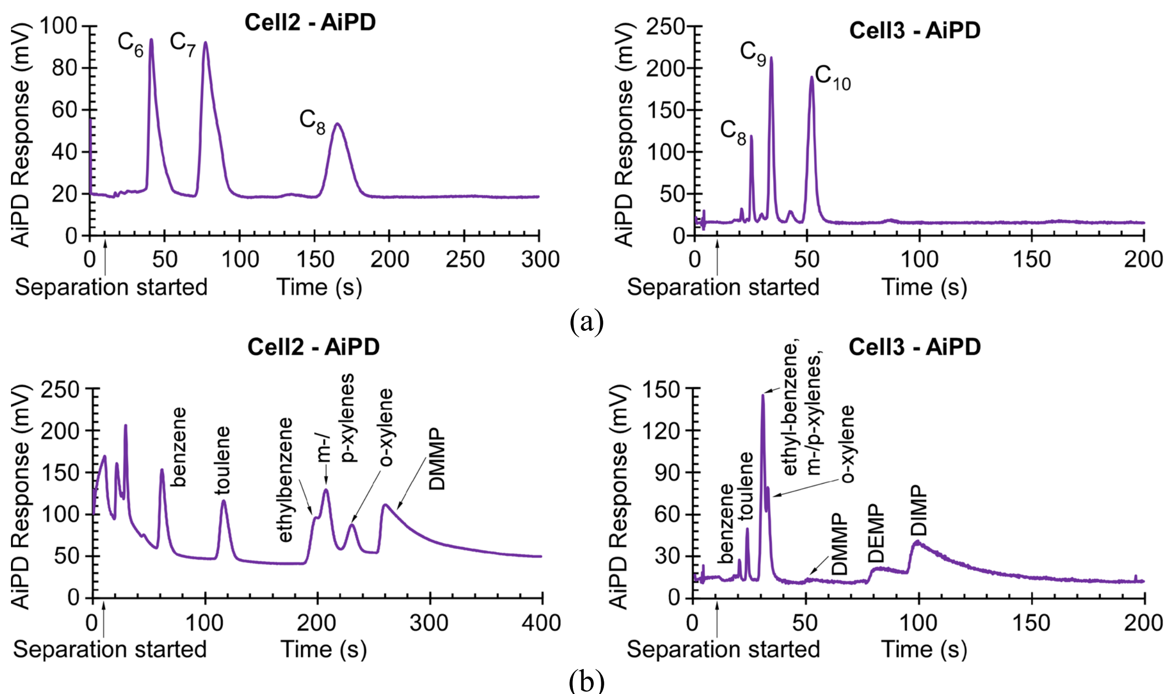

Fig. 3.9: (a) The chromatograms of alkanes generated by the AiPDs in Cell2 and Cell3. (b) The chromatograms of BTEX and phosphonates generated by the AiPDs in Cell2 and Cell3.

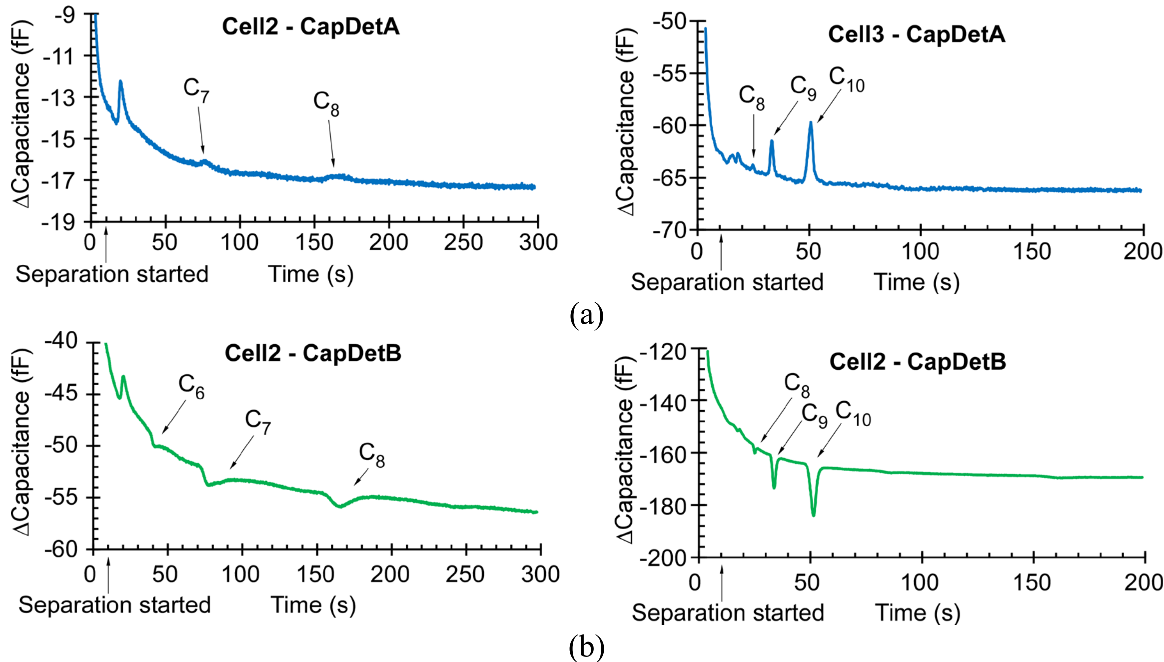

Fig. 3.10: (a) The chromatograms of alkanes generated by the CapDetAs in Cell2 and Cell3. (b) The chromatograms of alkanes and phosphonates generated by the CapDetBs in Cell2 and Cell3.

3.4 Discussion and Conclusion

This chapter describes a new flow management method that eliminates the sample inlet valve. In the preliminary evaluation, a setup that emulates the separation of a typical μGC system is established. The preliminary results validate that using a single pump to circulate the separation flow eliminates the undesired flow in the path of sample inlet. In the system implementation, to avoid the exhausts of analytes being redirected to the μGC system, the single separation pump is divided into two separation pumps. This allows the analytes to exit the system while maintaining the same function as the single pump that circulates the flow. The experimental results prove the feasibility of eliminating the valve at the sample inlet. Without the need of a high performance microvalve, the overall fabrication and assembly complexity, labor, and cost are eminently reduced. Additional benefits include the higher sampling flow rate and the system reliability. In the MPCA1.1 μGC, all the microfabricated components are monolithically integrated and have no moving parts.

Although the MPCA1.1 μGC suffered from minor outgoing flow during separation, it is acceptable. It demonstrated the capability of separating and detecting both non-polar and polar analytes with a wide range of volatility. For analytes that were distributed in Cell2 and Cell3, a primary cell can be selected based on the fractional distribution or the retention of the analytes. Early peaks in Cell3, such as benzene, toluene, ethylbenzene, and -m, -p -o xylenes peaks before 40 s, do not have proper retention in the separation column, and hence should not be used for identification, whereas the corresponding peaks in Cell2 have proper retention in the separation column and should be used for quantification and identification.

The distribution of analytes and detector response patterns are not the focus of this work, and hence not discussed further. However, some improvements can be envisioned: (1)

characterizing the response pattern of the detector arrays to establish a library of chemicals, and (2) quantitatively analyzing the distribution of the analytes between the two neighboring cells. These will permit identification of chemicals with similar retention times, even when they are coeluted.

In the future, pressure sensors that monitor the P_{up} and P_{down} shall be incorporated. These pressures could drift easily due to degradation of pumps, particle accumulation within the system, and variation in ambient conditions, such as humidity and temperature. By monitoring these pressures and adopt close-loop real-time control to both separation pumps, zero flow in the path of sample inlet can be maintained constantly. This ensures no unwanted sample loss or intake during separation, and thus improves separation performance of the MPCA1.1 μGC.

Chapter 4:

Thermal Management of

A Highly Integrated Microscale Gas Chromatograph

This chapter describes a thermal management method that identifies heating requirements and design constraints, establishes computational model, validates the model, and provides tailored on-chip heaters with high heating performances. To permit a high analytical performance for a microscale gas chromatography (μGC) system, high heating performances of the on-chip heaters and minimal thermal crosstalk among them are essential. The reported thermal management method is implemented on a highly-integrated μGC chip that monolithically integrates preconcentrators, columns, detectors, and a carrier gas filter. The transient thermal responses and temperature uniformities of these components are simulated by finite element analysis (FEA). Moreover, the modeling results are validated by the experimental thermography results. Upon the fabricated design, two designs with revised heater patterns, improving the heating ramp rates and temperature uniformities are reported. The effectiveness of the thermal isolation cutouts is evaluated. In the established FEA model, the revised monolithic on-chip heaters permit small temperature variations of <2°C in the preconcentrators and <4°C in the separation columns. The heaters also provide heating ramp rates of >50 °C/s (*i.e.,* heated to >170°C in 3 s) for the preconcentrators, >1 °C/s (*i.e.,* heated to >70°C in 50 s) for the columns, and >4 °C/s (*i.e.,* heated to >80°C in 15 s) for the detectors.

4.1 Introduction

4.1.1 Overview and challenges

Temperature management of microscale gas chromatography (μGC) components is critical to the analytical performance of any μGC system, especially when components are monolithically integrated. The heating requirements, such as targeted temperatures, heating durations, and heating ramp rates, vary significantly from components to components. For instance, a preconcentrator needs to be heated to a high temperature (>200°C) in a few seconds [Lee16, Zho16, Zha19]. Otherwise, the analytes might not be thermally desorbed completely by the preconcentrators. On the other hand, a column is usually heated to a moderate temperature (100°C) with a smaller ramp rate. Otherwise, highly surface-adsorptive analytes might be retained, and consequently present tailing in the correspondent chromatographic peaks. Overall, it is difficult to meet several sets of heating requirements when components are monolithically fabricated on a silicon substrate [Ter79, Lew06, Bon08, Kaa10, Man11, Pot12, Nar13, Red13, Col14, Akb15, San16, Zho16, Wan18, Zha19], which is thermally conductive. The thermal crosstalk among the components is rarely addressed by other reported monolithic μGC systems.

To mitigate the thermal crosstalk, using thermally insulating substrates or suspended structures, and incorporating physical cutouts or heatsinks can be implemented [Bon08, Man11, Col16, Qin16]. Thermally insulating substrates, such as fused silica or glass substrates, can significantly suppress the conductive heat transfer between the components. However, they may easily cause heating non-uniformity, which consequently causes problems such as incomplete preconcentrator desorption and peak tailing. Mechanically suspending the components and creating thermal isolation cutouts can also effectively suppress thermal crosstalk, while raising concerns about fabrication complexity and mechanical robustness [29]. Incorporating an external

heat sink or fan can dissipate heat out of the unwanted spaces, but these additional components increase the complexity of assembly and packaging. The selection of these approaches requires comprehensive considerations.

Several additional constraints should be taken into account when designing the monolithic on-chip heaters. For example, the heater voltages that can be supplied by the hardware electronics are limited. Therefore, to provide high heating powers, the electrical resistances of the heaters need to be low enough. Nonetheless, these on-chip heaters are typically made of thin film metals that typically high electrical resistances due to the thin-film nature. To achieve low electrical resistances, the width and length of the heaters need to be designed appropriately. Using thermally insulating substrate can mitigate thermal crosstalk as mentioned, however, the temperature uniformity is compromised. To resolve this issue, the patterns of the heaters need to be highly customized. Creating physical cutouts on a substrate also provides effective thermal isolation, however, the heater patterns might be damaged during the fabrication of the cutouts. Sufficient spaces between the thermal isolation cutouts and heater patterns need to be defined based on the manufacturing capability.

4.1.2 Goals

This chapter reports a thermal management method that addresses the aforementioned challenges. This method includes four major steps: 1) identifies targets and constraints, 2) establishes computational model, 3) validates the model through experimentally results, and 4) provides tailored heater designs based on the established model. Such a method is conducted on a highly-integrated μGC chip – the MPCA1 chip. The MPCA1 chip implements the multi-sensing progressive cellular architecture (MPCA) where three preconcentrators, three columns, nine detectors, and a carrier gas filter are monolithically integrated. To permit heating for each

component, on-chip heaters assuming a supplied voltage of 24 V are designed. The thermal isolation among the components is provided by the physical cutouts. To ensure that the heaters are not damaged during the fabrication of thermal isolation cutouts, a distance of 250 μm between these two features is mandatory.

To prevent incomplete desorption from the preconcentrators, uniform temperature distribution and rapid heating are required. The primary target is to achieve temperature variations smaller than 5°C within the sorbent areas (*i.e.,* the temperature between the center and the perimeter of the sorbent chamber) [Lew05]. The secondary target is to achieve a sufficient heating ramp rate. Based on the results reported in [Lia21], the smallest peak width at half height (PWHH) of the peaks in Cell1, Cell2, and Cell3 were ≈3.4 s, 2.3s and 2.4 s, respectively, provided by the separation column. In order to prevent the slow thermal desorption of preconcentrator from broadening the peaks, the preconcentrators need to be heated to 170°C within a time frame that is comparable to the PWHH of those peaks. Therefore, all the preconcentrators target a heating ramp rate of 50 °C/s (*i.e.*, heated from a room temperature of 20°C to 170°C in 3 s). It should be noted that although the three preconcentrators have the same targeted temperature variation and heating ramp rate, because of the differences in their sizes and thermal masses, they required different heating powers and custom heater patterns. Unlike the preconcentrators, the columns do not require rapid heating. Nonetheless, the columns shall have a heating ramp rate of 1 °C/s (*i.e.,* heated to 70°C in 50 s) to allow analysis of highly adsorptive analytes. The detectors are desired to be pre-heated to the targeted temperature and then operated isothermally, as temperature ramping may cause baseline drift in the detector signals. Therefore, a heating ramp rate of 4 °C/s (*i.e.,* heated to 80°C within 15 s) is adequate. The constraints and targets that are addressed by this method are listed in Table 4.1.

Table 4.1: Constraints and targets of the MPCA1 chip.

Hardware electronics	
• Supplied heating voltages are limited to 24 V	
Manufacturing	
• Tolerance of 250 μm is required between the thermal isolation cutouts and the heaters	
Thermal performances	
Preconcentrators	• Primary: Temperature variation <5°C • Secondary: Heating ramp rate >50 °C/s
Columns	• Heating ramp rate > 1°C/s
Detectors	• Heating ramp rate > 4 °C/s
Carrier gas filter	• Heating ramp rate >50 °C/s

In this thermal management method, a finite element analysis (FEA) model is established to evaluate whether the fabricated MPCA1 chip achieves the targeted values. The electrical behavior of the on-chip heaters, the thermal behavior of the μGC components, and the effectiveness of the thermal isolation cutouts are computationally simulated. The simulated results are validated by the thermography results of the heated MPCA1 chip using an infrared camera. Beyond the MPCA1 chip, the established computational model continues to be used to improve the heating ramp rate and temperature uniformity for individual component. Two designs of chips – MPCA2-A and MPCA2-B – that intend to improve the performances of the on-chip heaters are provided. The MPCA2-A chip assumes the thermal isolation cutouts with the same dimensions remain in the same locations as the MPCA1 chip, whereas the MPCA2-B chip assumes thermal isolation cutouts are not incorporated within the monolithic chip. Comparison between these two designs demonstrates the effectiveness and necessity of the thermal isolation cutouts.

The design and modeling are described in Section 4.2, the experimental results are presented in Section 4.3, and followed by the discussion and conclusion in Section 4.4.

4.2 Design and Modeling

A. MPCA1 chip – On-chip heaters

The MPCA1 chip is the same monolithic μGC chip that is presented in Chapter 2 and Chapter 3. The focus in this section is the design of the on-chip heaters. The MPCA1 chip incorporates three preconcentrators, three columns, three type-A capacitive detectors (CapDetA), three type-B capacitors (CapDetB), three arrayed integrated photoionization detectors (AiPDs), and a carrier gas filter (Fig. 4.1). The sizes of the three preconcentrators are tailored based on the volatility range of targeted analytes, whereas the sizes of the three columns are identical. Preconcentrator3, intended for low-volatility analytes, has the smallest sorbent chamber volume of 2.7 μL; Preconcentrator2, intended for medium-volatility analytes has a mid-size sorbent chamber volume of 8.6 μL; and Preconcentrator1, intended for the high-volatility analytes, has the largest sorbent chamber volume of 15.2 μL.

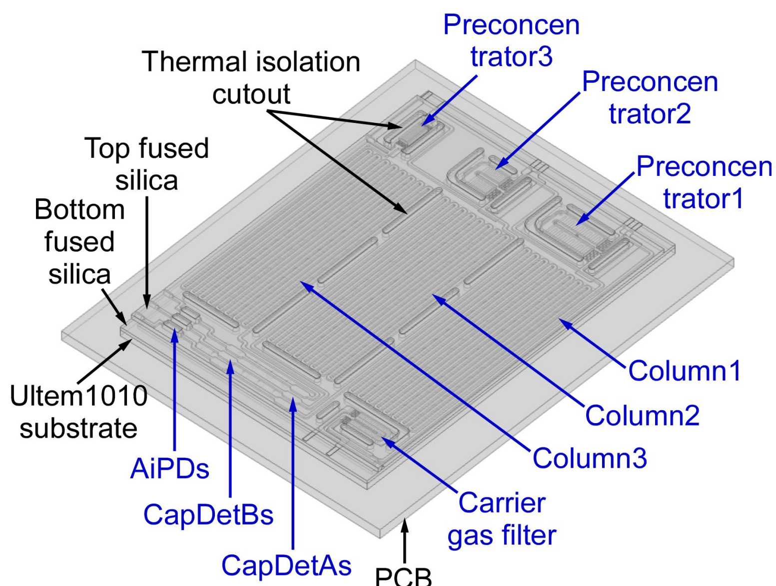

Fig. 4.1: The 3D illustration of the MPCA1 chip, Ultem1010 substrate, and PCB.

In the MPCA1 chip, to implement the heating of individual component, each preconcentrator, column, and carrier gas filter possesses its own set of on-chip heater and thermistor, whereas the detectors from the three cells share a single set of on-chip heater and thermistor. Although in principle the detectors may benefit from using separate heaters and thermistors, sharing a single set of heater and thermistor is acceptable, as the three types of detectors can operate at similar temperatures. To design on-chip heaters that can provide uniform and rapid heating, some general principles need to be followed: 1) The electrical resistances should be designed based on the heater voltage and targeted powers. With a heater voltage of 24 V, to provide at least a heating power of 5 W to the preconcentrators, the electrical resistances of the preconcentrator heaters shall be smaller than 115.2 Ω. On the contrary, the columns do not require rapid heating. Moreover, column heaters usually have higher electrical resistances because the heating metal traces need to follow the fluidic channels, which results in long lengths. To permit a heating power of at least 2 W, the electrical resistances of the column heaters need to be smaller than 288.0 Ω. 2) To provide uniform heating, custom serpentine patterns are commonly used (Fig. 4.2a). Nonetheless, it should be noted that longer metal trace leads to a higher electrical resistance and thus a lower heating power. To compensate for the electrical resistance, the width of the metal traces needs to be adjusted accordingly. The dimensions (*i.e.,* width and length) and the patterns of the heating metal traces are heavily coupled with each other. 3) To reduce parasitic heating, the effective heater fraction (*i.e.*, the serpentine fraction of the preconcentrator heater or the metal trace overlapping with the fluidic channels in the column heater) should generally have widths that are adequately smaller than those in the non-effective heater fraction. For the column heaters, to maintain a certain width while increasing the electrical resistance, narrow slits can be incorporated (Fig. 4.2.b).

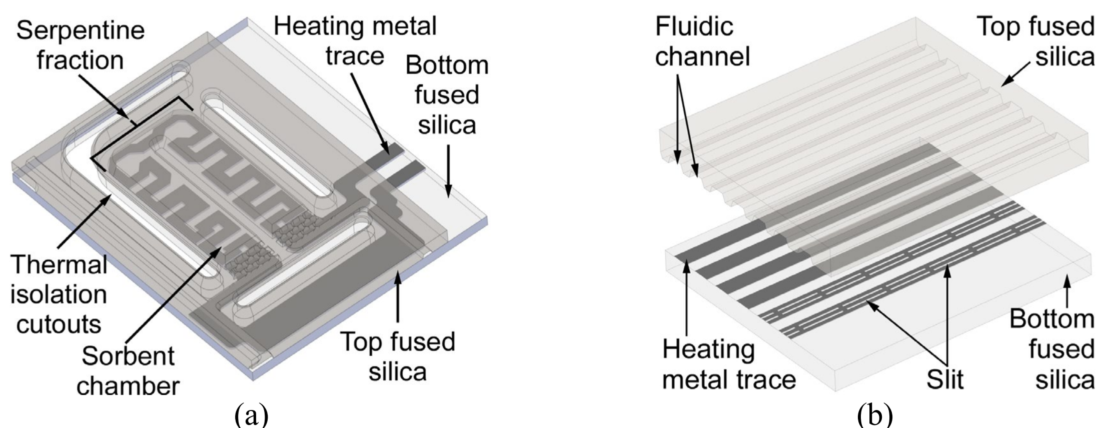

Fig. 4.2: (a) The 3D illustration of Preconcentrator1, showing the sorbent chamber and heater pattern. (b) The 3D illustration showing the slits of the column heater.

In the fabricated MPCA1 chip, several thermal isolation cutouts with a width of 1 mm are implemented. The length of these cutouts varies from 4.4 mm to 12 mm. These thermal isolation cutouts are minimally 250 µm away from the patterns of heaters. The MPCA1 chip is seated on a 3D printed Ultem 1010 substrate (provided by CIDEAS Inc., Crystal Lake, IL, USA), which incorporates array of pillars. The air gap between the pillars reduces heat dissipation from the MPCA1 chip to the printed circuit board (PCB), while the pillars maintain sufficient mechanical support (Fig. 4.1). The overall footprint of the MPCA1 chip is 40.3×55.7 mm^2.

B. Thermal Modeling

<u>Overview</u>

The transient thermal responses of the components in the monolithic µGC chip, including preconcentrators, columns, detectors, and a carrier gas filter, are simulated by finite element analysis (FEA) using COMSOL Multiphysics® 5.3. The heating ramp rate and temperature uniformity of each component as well as the effectiveness of the thermal isolation cutouts are modeled. The FEA model couples the electrical and thermal responses, including the effects of Joule heating and temperature-induced change in the electrical resistance of the on-chip heaters.

For each component, three different designs of chips – MPCA1, MPCA2-A, and MPCA2-B – are simulated[4]. The MPCA1 is the fabricated design, where the thermal isolation cutouts are initially implemented. However, the on-chip heaters are not designed for uniform heating. The MPCA2-A chip revises the patterns of on-chip heaters to permit uniform temperature distribution. The thermal isolation cutouts remain at the same locations with the same dimensions. In the MPCA2-B chip, the thermal isolation cutouts are assumed to be absent. This is to evaluate the effectiveness of the thermal isolation cutouts as they increase the fabrication complexity and reduce the mechanical integrity of the chip. The thermal isolation cutouts in the MPCA2-B chip are modeled as fused silica, which implies no physical cutouts are created.

Mimicking the designed implementation, the simulated structure incorporates the MPCA1 chip seated on the Ultem 1010 substrate, which is further mounted on a PCB. The thermal conductivity assumed for each material is listed in Table 4.2. The sorbent beds of the preconcentrators and the carrier gas filter are modeled as a uniform material with an equivalent thermal conductivity of 6 W/mK [Dun89]. All the fluidic channels and the thermal isolation cutouts are modeled as air. Also incorporated in the model are the experimentally measured temperature coefficient of resistance and electrical resistivity at room temperature of the Ti/Pt thin film, which are 0.003 1/°C and 3.8×10^{-7} Ω·m, respectively. The ambient temperature is assumed to be 20°C. Natural air convection is assumed on all the exterior surfaces.

Prior to modeling the thermal characteristics, the electrical resistance of each heater in the MPCA1 chip is first verified in the model. The simulated resistances generally match the experimentally measured values (Table 4.3). The simulated resistances of the heaters in the MPCA2-A and MPCA2-B chips are also provided. Then, in the simulation of heating each

[4] The layout of the MPCA1 chip was provided by Ms. Weilin Liao.

individual component, a 24 V heater voltage is supplied to its heater at t =2.0 s in a step function with smooth approximation: the voltage remains at 0 V at t = 1.9 s and reaches 24 V at t = 2.1 s. Specifically, the average temperatures of the heated components are monitored over the transient heating.

Table 4.2: Thermal conductivity values of the simulated components in FEA.

Materials	Thermal conductivity value (W/mK)
Fused silica	1.4
Sorbent material	6.0
PCB	0.30
Ultem 1010	0.22
Ti/Pt	71.6
Air	0.03

Table 4.3: Measured and simulated electrical resistances of the on-chip heaters.

Heater	Measured MPCA1 (Ω)	Simulated MPCA1 (Ω)	Simulated MPCA2-A (Ω)	Simulated MPCA2-B (Ω)
Preconcentrator1	85.2	90.5	66.9	67.8
Preconcentrator2	94.2	101.0	67.7	70.1
Preconcentrator3	99.3	117.2	104.2	104.2
Column1	274.0 (average)	288.3	181.3	178.7
Column2		281.8	175.2	190.4
Column3		293.7	170.9	177.6
Detector	166.0	157.9	130.3	N/A
Carrier gas filter	80.0	97.2	84.9	94.8

Preconcentrator1

The temperature ramping rates, current consumptions, and temperature distributions of Preconcentrator1 of the three different designs are shown in Fig. 4.3., whereas the electrical and thermal characteristics are summarized in Table 4.4. In 4 s of heating, the Preconcentrator1 shows heating ramp rates of 50.4 °C/s in the MPCA1 chip, 59.4 °C/s in the MPCA2-A chip, and 44.3 °C/s in the MPCA2-B chip, respectively. The heating ramp rates are mainly affected by the heating power and the presence of the thermal isolation cutouts. In the case of preconcentrators, the effect of thermal isolation cutouts dominates because their sizes are comparable to the preconcentrators.

Among the three chips, the MPCA2-A chip has the highest heating ramp rate, followed by the MPCA1 chip, and the MPCA2-B chip. In the MPCA1 and MPCA2-A chips, even though Preconcentrator1 is heated to over 200°C, the neighboring components remain nearly at the room temperature, indicating the effectiveness of the thermal isolation cutouts for confining the heat within each preconcentrator. In the MPCA2-B chip, the north edge of the Column1 reaches ≈40°C.

As evident from the Fig. 4.3c, the temperature distribution within Preconcentrator1 of the MPCA1 chip is non-uniform. It shows a temperature variation of 65.7°C across the sorbent area. By revising the heater pattern, the temperature variations are significantly reduced. In the MPCA2-A and MPCA2-B chips, the temperature variations are 0.5°C and 13.9°C, respectively. The impact and necessity of the thermal isolation cutouts can also be seen from the temperature variations.

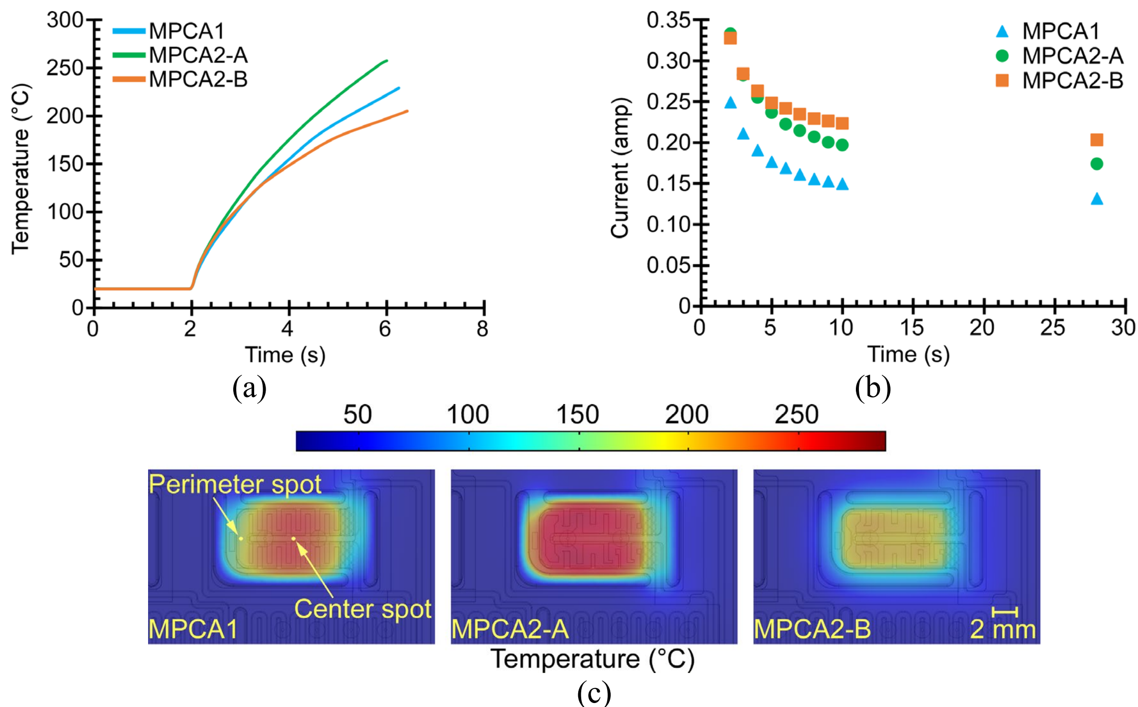

Fig. 4.3: The simulated thermal characteristics of Preconcentrator1 in three different designs. (a) The simulated transient responses. (b) The simulated current consumptions. (c) The simulated temperature distributions after 4 s of heating.

Table 4.4: Heating power and thermal characteristics of Preconcentrator1 in 4 s.

Chip design	Power (W)	Ramp rate (°C/s)	σ (std. dev.) (°C)	σ (std. dev.) (%)	Cen. (°C)	Per. (°C)	Var. (°C)	Var. (%)
MPCA1	6.36	50.4	23.9	12.2	236.2	170.5	65.7	32.6
MPCA2-A	8.61	59.4	17.7	7.6	247.8	247.3	0.5	0.2
MPCA2-B	8.50	44.3	13.6	7.9	193.1	1792	13.9	7.9

Preconcentrator2

The heating ramp rates, current consumptions, and temperature distributions of Preconcentrator2 are shown in Fig. 4.4. The electrical and thermal characteristics of Preconcentrator2 are provided in Table 4.5. Preconcentrator2 has the mid-size among the three preconcentrators. Similar to Preconcentrator1, the thermal isolation cutouts have a more significant impact than the heating power on the heating ramp rates. In 2.5 s, Preconcentrator2 shows heating ramp rates of 73.2 °C/s, 95.0 °C/s, and 77.8 °C/s in the MPCA1, MPCA2-A, and MPCA2-B chips, respectively. The MPCA1 chip has a lower heating ramp rate because of the low heating power, whereas the MPCA2-B has a lower heating ramp rate because of the absence of the cutouts. In both MPCA1 and MPCA2-A chips, the neighboring components remained at <30°C, whereas in the MPCA2-B chip, the north edge of Column2 reaches ≈46°C.

Non-uniform temperature distribution is observed in the MPCA1 chip where a temperature variation of 67.1°C is presented. By using the same approach that adjusts the dimensions and patterns of the heating metal traces based on the MPCA1 temperature distribution, the temperature variations are reduced to 0.7°C and 12.1°C in the MPCA2-A and MPCA2-B chips, respectively.

Table 4.5: Heating power and thermal characteristics of Preconcentrator2 in 2.5 s.

Chip Design	Power (W)	Ramp rate (°C/s)	σ (std. dev.) (°C)	σ (std. dev.) (%)	Cen. (°C)	Per. (°C)	Var. (°C)	Var. (%)
MPCA1	5.70	73.2	19.6	10.4	210.8	143.7	67.1	36.7
MPCA2-A	8.51	95.0	11.6	4.9	239.8	20.5	0.7	0.3
MPCA2-B	8.12	77.8	10.1	5.3	203.4	11.3	12.1	6.2

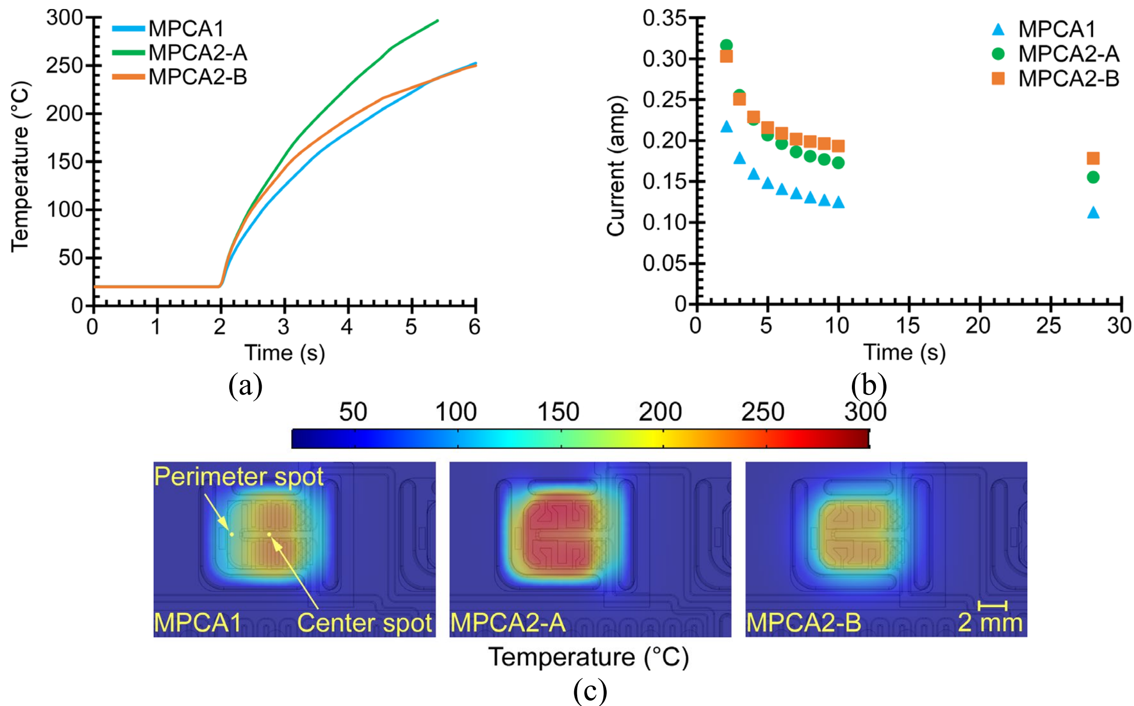

Fig. 4.4: The simulated thermal characteristics of Preconcentrator2 in three different designs. (a) The simulated transient responses. (b) The simulated current consumptions. (c) The simulated temperature distributions after 2.5 s of heating.

Preconcentrator3

The heating ramp rates, current consumptions, and temperature distributions of the Preconcentrator3 are shown in Fig. 4.5. The electrical and thermal characteristics of Preconcentrator3 are provided in Table 4.6. Preconcentrator3 has the smallest size among the three preconcentrators, therefore, with the same targeted heating ramp rate, the required heating powers are smaller. In Preocncentrator3, because the heating power of the MPCA1 chip is sufficient, the electrical resistances of the heaters in both MPCA2-A and MPCA2-B chips are not enormously decreased to increase the heating power. Additionally, the heater patterns in the MPCA2-A and MPCA2-B chips are identical. In 1 s of heating, Preconcentrator3 shows heating ramp rates of 189.7 °C/s in the MPCA1 chip, 195.6 °C/s in the MPCA2-A chip, and 169.1 °C/s in the MPCA2-B chip. The high heating ramp rates are attributed to the small size of

Preconcentrator3. The neighboring components in all three designs remained at nearly room temperature because of the short heating duration.

The temperature variation within the sorbent area of the MPCA1 chip is 19.3°C. Although it is smaller than those prenoted in Preconcentrator1 and Preconcentrator2 due to the shorter heating duration, it still does not reach the goal of 5°C variation. In the MPCA2-A and MPCA2-B chips, the temperature variations are reduced to 2.0°C and 0.5°C, respectively. It is worth noting that for the smallest Preconcentrator3, the MPCA2-B chip has the smallest temperature variation. This is because the sorbent area is smaller than the area covered by the heating metal traces. Even if the thermal isolation cutouts are absent, the sorbent area can still be uniformly heated.

The carrier gas filter, which has the similar structure and size to the preconcentrators, is also simulated. The results are presented in the Appendix B.

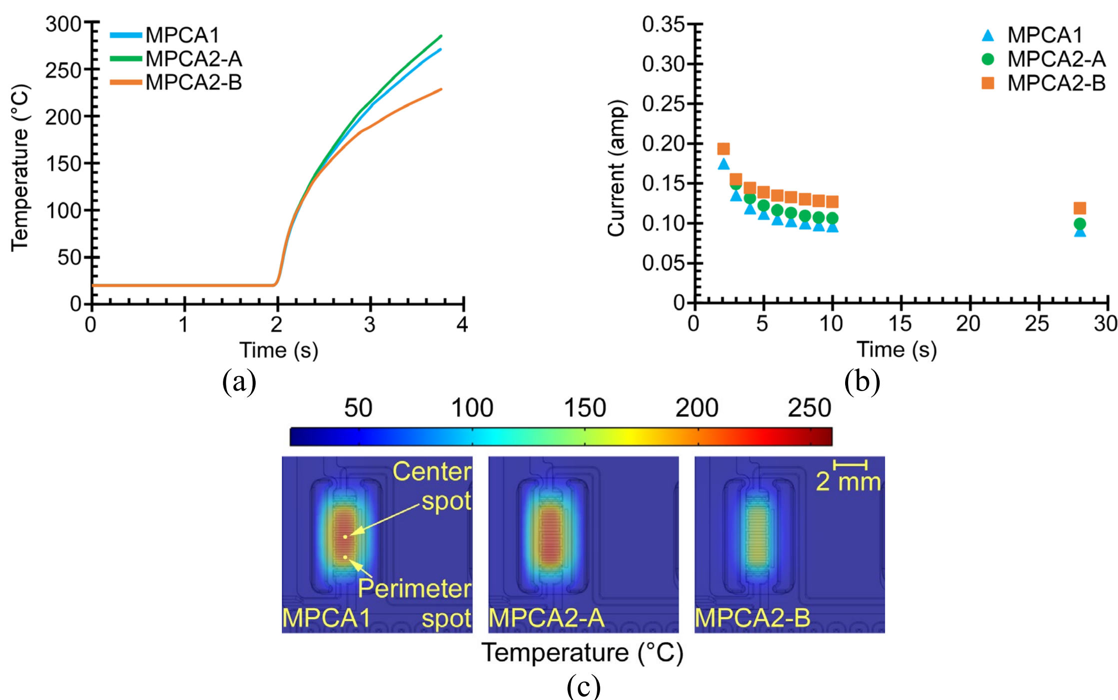

Fig. 4.5: The simulated thermal characteristics of Preconcentrator3 in three different designs. (a) The simulated transient responses. (b) The simulated current consumptions. (c) The simulated temperature distributions after 1 s of heating.

Table 4.6: Heating power and thermal characteristics of Preconcentrator3 in 1 s.

Chip Design	Power (W)	Ramp rate (°C/s)	σ (std. dev.) (°C)	σ (std. dev.) (%)	Cen. (°C)	Per. (°C)	Var. (°C)	Var. (%)
MPCA1	4.91	189.7	14.0	7.6	211.2	191.9	19.3	10.2
MPCA2-A	5.53	195.6	10.9	5.7	210.0	208.0	2.0	1.1
MPCA2-B	5.53	169.1	11.6	7.1	183.9	184.4	0.5	0.3

Column1

The electrical and thermal characteristics of Column1 are summarized in Table 4.7. During the transient heating, Column1 shows heating ramp rates of 0.80 °C/s, 1.11 °C/s, and 1.08 °C/s in the MPCA1, MPCA2-A, and MPCA2-B chips, respectively (Fig. 4.6a). From the transient responses, the MPCA1 chip does not reach 70°C after 50 s of heating, which indicates the heating power is not sufficient. Although the thermal isolation cutouts can confine the heat within the columns and thus raise the heating ramp rates, they are not as effective as they are in the preconcentrators because of the large sizes of the columns. Therefore, reducing the electrical resistances of the heaters to increase heating power is required. Among the three designs, only the MPCA2-A chip achieve the targeted heating ramp rate of 1.1 °C/s. When Column1 is heated, in both MPCA1 and MPCA2-A chips, the neighboring components, including the Preconcnetrator1, Column2, and carrier gas filter, remained at < 31°C. However, in the MPCA2-B chip, these neighboring components are heated to 40-50°C.

Table 4.7: Heating power and thermal characteristics of Column1 in 50 s.

Chip Design	Power (W)	Ramp rate (°C/s)	σ (std. dev.) (°C)	σ (std. dev.) (%)	Cen. (°C)	Per. (°C)	Var. (°C)	Var. (%)
MPCA1	2.00	0.80	3.8	10.7	61.2	58.2	3.0	7.5
MPCA2-A	3.18	1.11	3.7	6.9	74.9	78	3.1	5.6
MPCA2-B	3.23	1.08	5.1	11.0	71.1	61.2	9.9	18.4

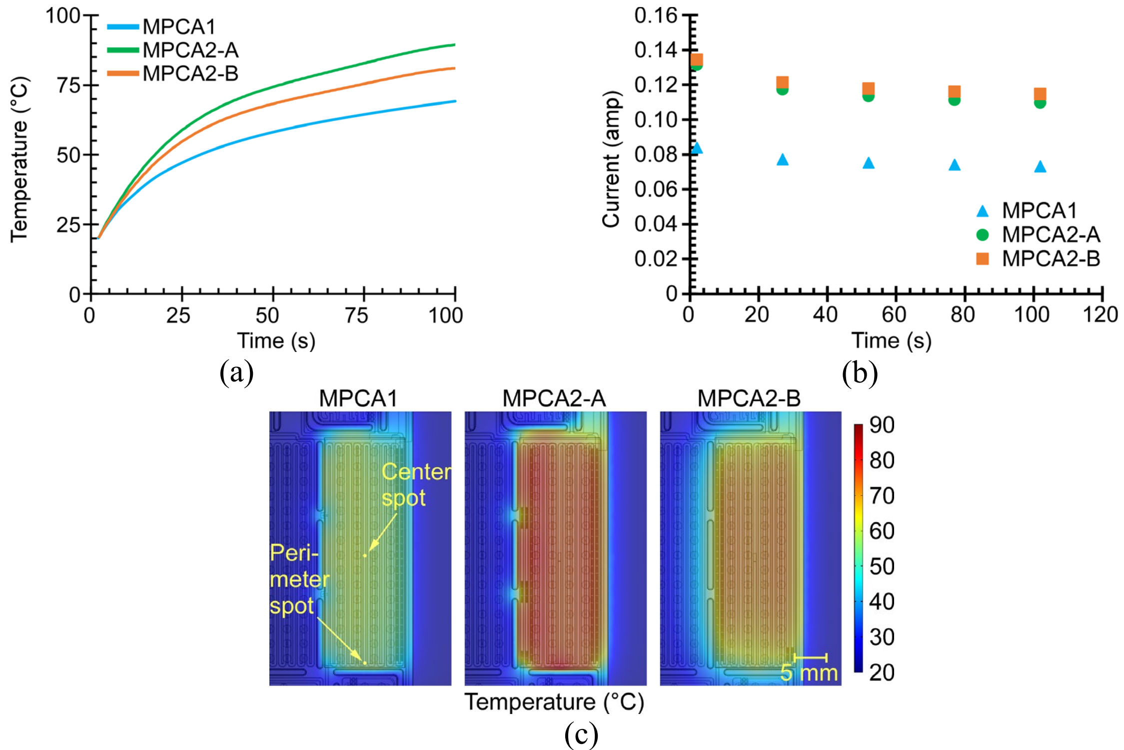

Fig. 4.6: The simulated thermal characteristics of Column1 in three different designs. (a) The simulated transient responses. (b) The simulated current consumptions. (c) The simulated temperature distributions after 50 s of heating.

Temperature distributions after 50 s of heating are shown in Fig. 4.6c. The temperature variations of the MPCA1 and MPCA2-A chips are 3.0°C and 3.1°C, respectively. However, in the MPCA2-B chip, the temperature variation is increased to 9.9°C due to the lack of thermal isolation cutouts. The heat dissipates to the neighboring components, rather than being confined within the column area. This makes the perimeter of Column1 to be colder than the center, and thus reduces the temperature uniformity.

The thermal transient responses of Column2 and Column3 are provided in Fig. 4.7a and b. The results show that only the MPCA2-A chip that has both higher heating power and thermal isolation cutouts achieve the targeted temperature of 75°C in 50 s. Detailed electrical and thermal characteristics, and temperature distributions are provided in Appendix B.

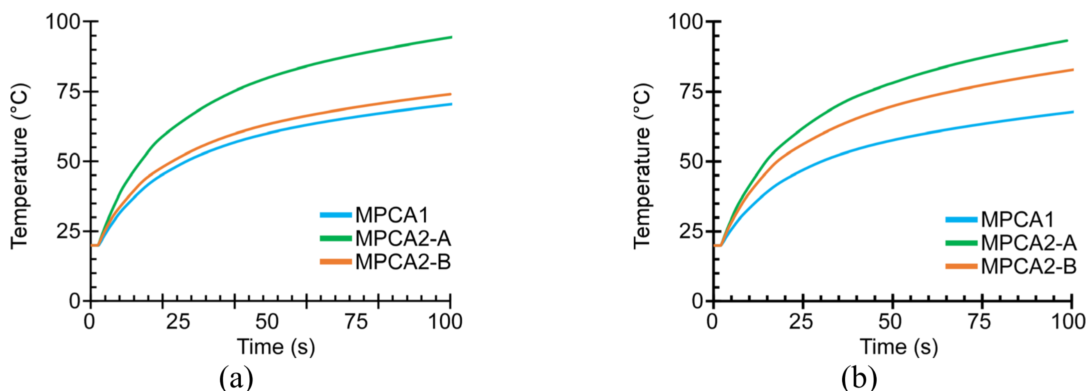

Fig. 4.7: The simulated transient responses of (a) Column2 and (b) Column3.

Detector

The temperature distributions and transient responses of the detectors in the MPCA1 and MPCA2-A chips are shown in Fig. 4.8a and b separately. Based on the simulation, all detectors reach >72.3°C in 15 s (*i.e.,* equal to a heating ramp rate of >3.4 °C/s) in the MPCA1 chip (Fig. 4.8a). Separated by the thermal isolation cutouts, most of the neighboring areas remain at <30°C. In the MPCA2-A chip, the on-chip heater is revised to resolve the accumulated heat in certain areas. The heating ramp rates are also increased that all the detectors in the MPCA2-A chip are heated to >83.2°C in 15 s (*i.e.,* achieve heating ramp rates of >4.2 °C/s) (Fig. 4.8b). Moreover, the fluidic interconnects between the detectors are heated more uniformly. However, because all the detectors shared a single heater that must avoid the sensing electrodes of the detectors, high temperature uniformity is difficult to achieve. As illustrated in the preconcentrators and columns that thermal isolation cutouts are necessary, the design of MPCA2-B is not implemented for the detectors.

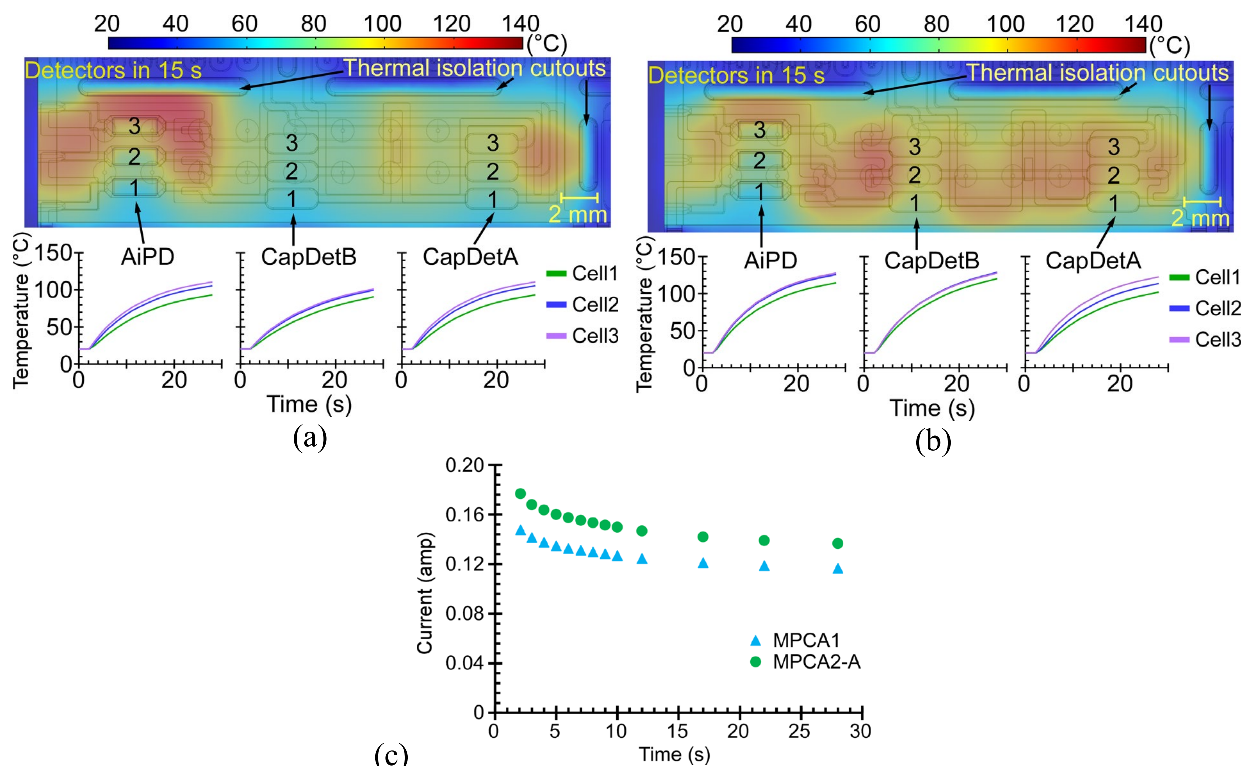

Fig. 4.8: The simulated temperature distributions and transient responses of the detectors in (a) the MPCA1 chip, and (b) the MPCA2-A chip. (c) Current consumptions of the detector heaters in the two designs.

4.3 Experimental Results

To reveal the temperature distribution of the heated MPCA1 chip, thermal imaging was conducted using an infrared camera (MS-IR M-VLW-SLS, Telops, Canada)[5]. The MPCA1 chip was seated on the Ultem1010 substrate and soldered to the PCB via commercial headers for electrical control and temperature programming. In this experiment, no flow was supplied to the MPCA1 chip. Each heater was supplied with 24 V. The heating started with Cell1 components, followed by the Cell2 and Cell3 components sequentially (Fig. 4.9). In each cell, the column was heated prior to the preconcentrator. The targeted temperature of each column was 100°C whereas the targeted temperature of each preconcentrator was 180°C. The detector was heated along with

[5] These experiments were performed at the Naval Research Lab with the help from the staff.

the Cell3 components. The columns and detectors were covered by copper shields that were grounded to reduce electromagnetic interference, and thus not visually accessible by the infrared camera.

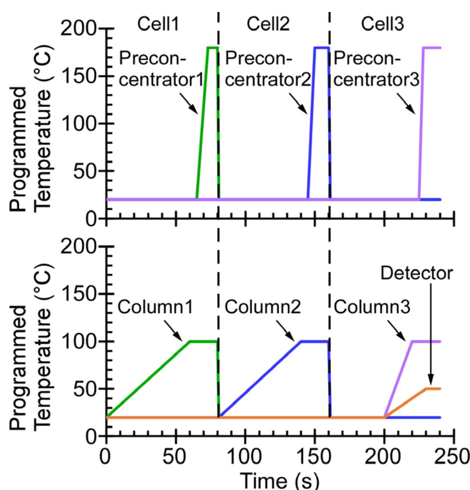

Fig. 4.9: The programmed temperature and heating duration of each component.

The thermography results of Preconcentrator1 and Preconcentrator2 were provided in Fig. 4.10 and Fig. 4.11. Moreover, the temperature of a measured spot in each preconcentrator was provided. To compare with the simulated results that were reported in Section 4.2, the simulated temperature distribution, and the ramping of average temperature of the sorbent area and the thermistor area were plotted along with the experimental results.

As indicated by the thermography results (Fig. 4.10a and Fig. 4.11a), the heating of preconcentrator was not uniform. As the heating duration lasted, the temperature around the sorbent areas became higher, whereas the temperature around the thermistor area remained low. For Preconcentrator1, after 4.0 s of heating, the sorbent area was 88°C higher than the thermistor area; for Preconcentrator2, after 2.5 s of heating, the sorbent area was ≈91°C higher than the thermistor area. The heating ramp rates (Fig. 4.10b and Fig. 4.11b) showed that the temperature of the measured spot lay between the average temperatures of the sorbent area and the thermistor

area. Although the initial temperatures in the experiments were slightly higher than the room temperature due to the heating of the neighboring columns, this did not affect the results of temperature uniformities and heating ramp rates. The experimental results validated the non-uniform temperature distribution within the heated MPCA1 chip.

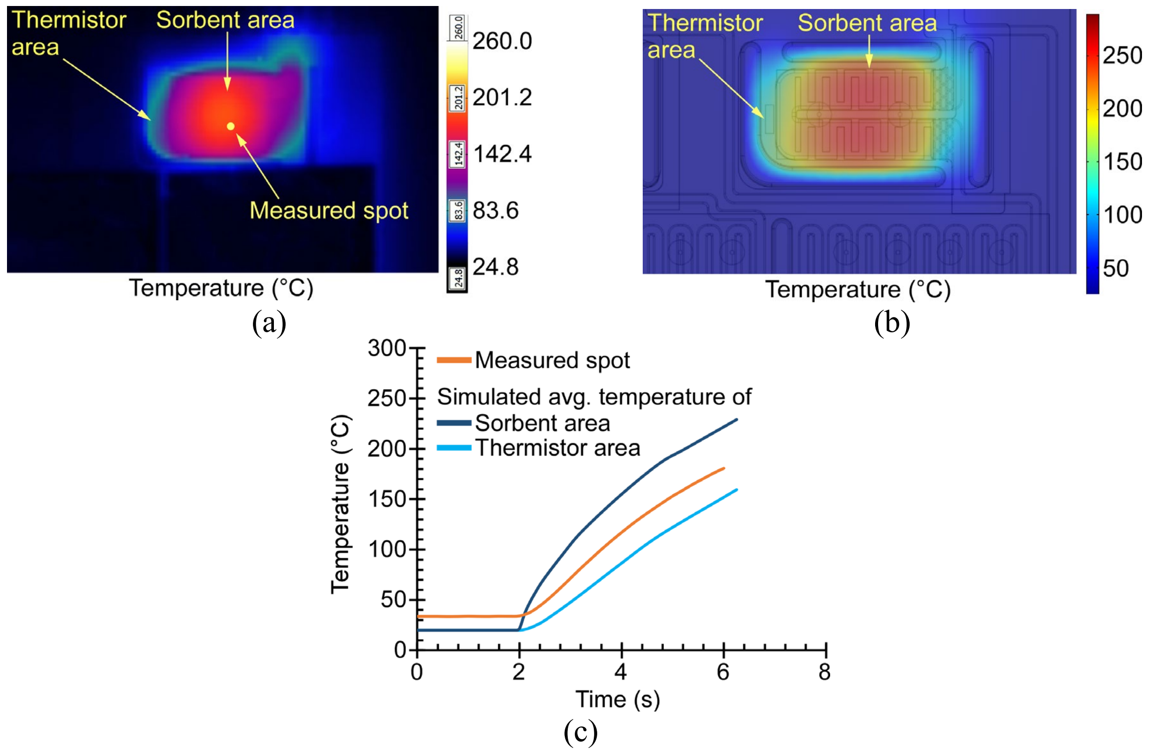

Fig. 4.10: The temperature distributions and heating ramp rates of Preconcentrator1 after 4 s of heating. (a) The thermography results. (b) The simulated results. (c) The transient thermal responses.

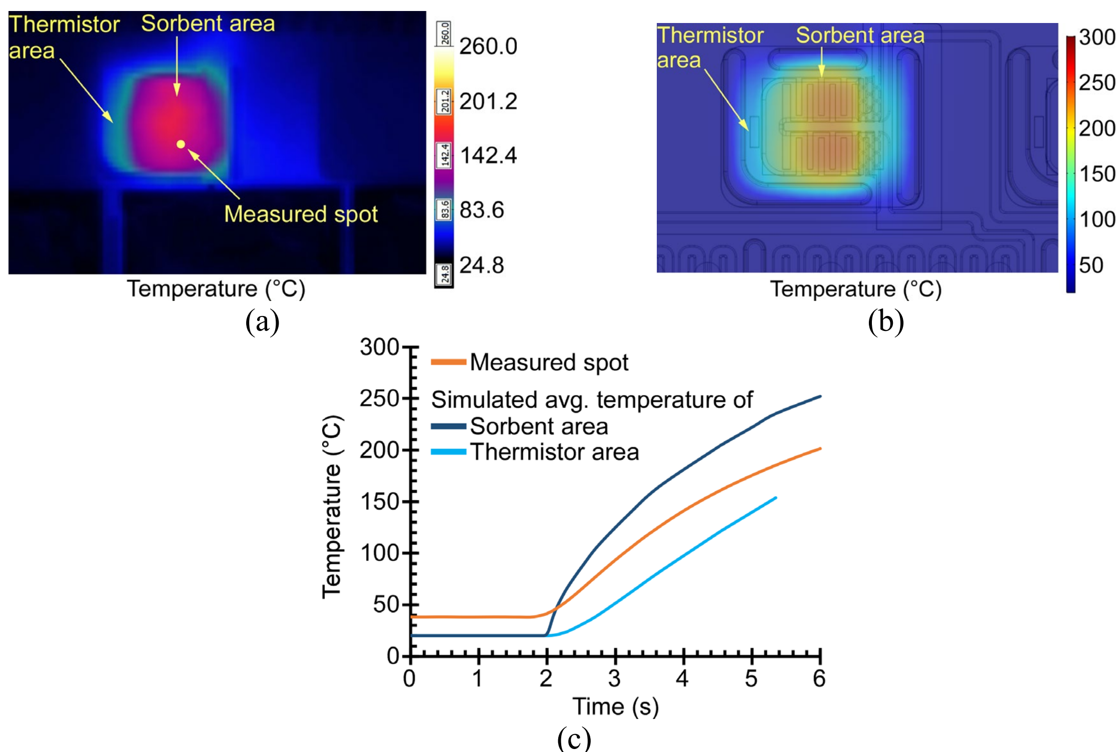

Fig. 4.11: The temperature distributions and heating ramp rates of Preconcentrator2 after 2.5 s of heating. (a) The thermography results. (b) The simulated results. (c) The transient thermal responses.

4.4 Discussion and Conclusion

This chapter presents a thermal management method that significantly improves the performances of the monolithic on-chip heaters while addressing several constraints. The targeted temperature variations and heating ramp rates are defined based on the analytical performance of the PCA and the targeted analytes in each cell. The primary and secondary targets of the preconcentrator heaters are to achieve a temperature variation <5°C and a heating ramp rate of >50 °C/s. The columns require a heating ramp rate of >1 °C/s, whereas the detectors require a heating ramp rate of >4 °C/s. All the targeted values are achieved in the MPCA2-A chip.

In the MPCA1 chip, the simulated heating ramp rates and temperature variations are 50.4 °C/s and 65.7°C for Preconcentrator1, 73.2 °C/s and 67.1°C for Preconcentrator2, and 189.7 °C/s

with 19.3°C for Preconcentrator3, respectively. Although the three preconcentrators achieve the targeted heating ramp rates, none of them meet the requirements of 5°C temperature variation. The three columns show heating ramp rates <0.85 °C/s, which are insufficient. For the detectors, the three of them in Cell1 did not achieve the targeted heating ramp rate of 4 °C/s. In this design, the heating powers of many components are insufficient. Moreover, the temperature distributions of the preconcentrators are extremely non-uniform.

In the MPCA2-B chip, the heater patterns are revised, but the thermal isolation cutouts are not implemented. The simulated heating ramp rates and temperature variations are 44.3 °C/s and 13.9°C for Preconcentrator1, 77.8 °C/s and 12.1°C for Preconcentrator2, and 169.1 °C/s and 0.5°C for Preconcentrator3, respectively. Among the three preconcentrators, only Preconcentrator3 achieve the desired performances. The heating ramp rates of Column1, Column2, and Column3 are 1.1 °C/s, 0.9 °C/s, and 1.0 °C/s, respectively. Among the three columns, Column2 does not achieve the desired performance. This design proves that the absence of thermal isolation cutouts significantly compromises both heating ramp rates and uniformities.

In the MPCA2-A chip, the heater patterns are revised, and the thermal isolation cutouts are implemented. The simulated heating ramp rates and temperature variations are 59.4 °C/s and 0.5°C for Preconcentrator1, 95.0 °C/s and 0.7°C Preconcentrator2, and 195.6 °C/s and 2.1°C Preconcentrator3, respectively. These simulated values achieve the targeted values in both temperature variations and heating ramp rates. The three columns show heating ramp rates of >1.1 °C/s; all the detectors show heating ramp rates of >4.2 °C/s. Both columns and detectors obtain the desired heating performances.

This set of thermal modeling results demonstrates the impact and necessity of heater improvement and thermal isolation cutouts. The thermal isolation cutouts not only ensure the

unheated components are minimally affected, but also improve the heating ramp rates and uniformities of the heated components. This effect is more prominent when the components have comparable sizes to the cutouts, such as the preconcentrators and carrier gas filter.

The thermography results demonstrate significant non-uniform temperature distributions within the heated preconcentrators and validate the outcomes of the thermal FEA. For Preconcentrator1, after 4 s of heating, the thermography results show a temperature difference of ≈88°C between the sorbent area and the thermistor area, whereas the simulated results show a temperature difference of ≈91°C. For Preconcentrator2, after 2.5 s of heating, the thermography results show a temperature difference of ≈91°C, whereas the simulated results show a temperature difference of ≈105°C. The heating ramp rates of the measured spots are closer to the heating ramp rates of the thermistor areas, which are relatively cold in both Preconcentrator1 and Preconcentrator2. This is possibly because the measured spots are not at the center of the sorbent areas. Additionally, the experimentally supplied heating voltages may be lower than 24 V due to the close-loop control and parasitic electrical resistances, and consequently reduce the supplied heating power.

To conclude, in this thermal management method, the monolithic on-chip heaters of several μGC components, including preconcentrators, columns, detectors, and a carrier gas filter are tailored to achieve their targeted performances while addressing the manufacturing and electronics constraints. The established computational model is validated by the experimental results and used to revise the heater designs. The MPCA2-A chip will be fabricated and experimentally tested as a future effort. Such a method can be applied to other highly-integrated μGC designs where different sets of constraints and targets are imposed.

Chapter 5:

Conclusions And Future Work

5.1 Conclusions

This research has advanced the fluidic and thermal management methods of highly-integrated microscale gas chromatography (μGC) systems. Monolithic microvalve modules (VM1 and VM2) intended for μGC applications with high performances are demonstrated. These microvalve modules possess the unique features of high chemical inertness and embedded flow heating that have not been reported in any other works. Alternatively, a flow management method that eliminates the sample inlet valve, and thus reduces the overall complexity of a μGC system is reported. The analytical performance of the μGC system is not compromised, which is validated by the chromatograms of a wide volatility range of analytes. Finally, temperature and heating management of various μGC components, including preconcentrators, columns, detectors, and a carrier gas filter, are investigated. The tailored design of each on-chip heater ensures sufficient heating ramp rate and temperature uniformity. The importance of thermal isolation cutouts is proved by comparing the two designs, one assumes the existence of cutouts and the other one assumes the absence of cutouts.

The monolithic multi-valve modules provide high flow modulation capability, low power actuation, chemical inertness, and embedded flow heating. Besides the high performance, a facile fabrication that needs no more than three lithographic masks is accomplished, attributing to the combination of microfabricated components and prefabricated components. The microvalve

measures a flow conductance of 3.46×10^3 and can actively withstand bi-directional flow. The consumed energy and time response per valve switch are 0.27 J and 120 ms, which are both sufficient for μGC applications. Chemical injection tests with quantitative analysis demonstrating the low dead volume, chemical inertness, and embedded flow heating capability of the microvalve are performed. The tested analytes include alkanes, alcohol, ketone, aromatic hydrocarbons, and phosphonates. Furthermore, the lifetime of the VM2 is thoroughly evaluated. The flow is supplied in both positive pressure and negative pressure regimes in both open and closed states of valve. The valve is heated to 75°C by the embedded flow heater in the open state, mimicking the application scenarios. The lifetime of VM2 is > 480 hours. Such high reliability makes it eligible to any system that is deployed in field and requires a long maintenance-free period. Finally, the VM2s are incorporated into the MPCA1.0 μGC, which successfully present a chromatogram of 22 analytes.

The benchmarking of microfabricated and commercial off-the-shelf (COTS) valves are shown in Fig. 5.1. In order to compare the valves within the context of μGC, the performance can be summarized in five metrics: open-close ratio of flow conductance, ease of fabrication, compactness (which is inversely related to size), chemical resistance, and embedded flow heating. For most μGC systems and other systems where frequent switching of valve is not required, the power consumption and response time are less critical, and, therefore, not compared. In Fig. 5.1, two metrics — open-close ratio of flow conductance, and compactness — that can both be quantitatively evaluated are scaled to a range of 0-5; three other metrics — embedded flow heating, chemical resistance, and ease of fabrication — which can only be qualitatively evaluated, are rated high (H), medium (M), or low (L). The open-close ratio of flow conductance is evaluated based on the actual performance; the compactness is evaluated based on the device volume; ease-of-

fabrication is estimated from the lithographic mask count, except for the COTS valve; and chemical resistance is estimated from the wetted materials. The original data and scaled values of these metrics are provided in Table 5.1. For μGC systems, the microvalve should preferably merit at least a moderate score in each of the five metrics.

Table 5.1: The original values and scaled values for benchmarking the valves.

	Open-close ratio | Scaled Val.	Volume | Compact.	Embedded flow heating	Chem. Resis.	Ease. of Fab.
Pot12	6.97×10^5 | 5.00	0.11 | 5	L	H	L
Par08	9.80×10^3 | 3.15	1.00 | 4.051	L	M	L
Lu18	3.68×10^3 | 2.72	13.50 | 2.92	L	H	M
This work	3.45×10^3 | 2.7	10.07 | 3.05	H	H	M
Gro15	9.46×10^2 | 2.13	0.58 | 4.29	L	H	L
Böh00	1.00×10^2 | 1.16	1.03 | 4.04	L	L	M
Clippard	2.00×10^4 | 3.46	8.38 | 3.13	L	H	H
The Lee Co.	4.88×10^4 | 3.85	0.88 | 4.10	L	L	H

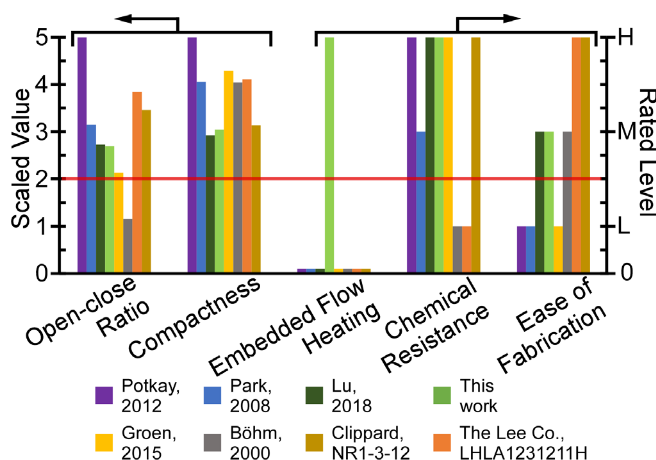

Fig. 5.1: A multi-dimensional benchmarking of microvalves in the context of μGC. The minimum desired level for μGC is indicated by the red line. The microvalve module in this work uniquely provides both embedded flow heating capability and superior chemical resistance, while only modestly compromising other metrics.

The second major contribution of this thesis is the validation of a new flow management method that demonstrates the feasibility of eliminating the valve at the sample inlet while permitting bi-directional flow in preconcentrators. The concept is first validated using a setup that represents a simplified μGC architecture. A separation pump that circulates the flow and a flow

restrictor are combined to replace the sample inlet valve. In the preliminary evaluation, no undesired flow is observed in steady state; the undesired transient flow is minimal. In the system-level demonstration, the single separation pump is divided into two pumps to provide better analytical performances. All the valves integrated within the MPCA1.1 μGC are not placed in any critical flow path that demands superior chemical inertness and embedded flow heating. Therefore, COTS valves are utilized. This approach significantly reduces complexity and cost of a μGC system. Fluidic analysis is performed to minimize the undesired gas flow in the path of sample inlet during separation. Along with the efforts on the microvalve modules, this research advances the control of gas flow control in μGC. Both the microvalves and the fluidic architecture that eliminates the sample inlet valve can be adopted by general μGC systems.

The thermal management in μGC is as important as the flow management. The proposed thermal management method presents a design flow that defines targets and constraints, establishes computational model, validates simulation, and performs design revision. This method is implemented in a highly-integrated MPCA1 chip, where the temperature ramping and distribution of several monolithic components are comprehensively studied via finite element analysis (FEA). Thermography results revealing the non-uniform temperature distribution within the heated preconcentrators of the MPCA1 chip are provided to validate the FEA model. The MPCA2-A chip, which is revised upon the MPCA1 chip, has shown significant improvement in both heating ramp rates and temperature uniformities quantitatively. The comparison between the MPCA2-A and MPCA2-B proves the importance of the thermal isolation cutouts. This type of thermal management method can be applied to any μGC system that has different sets of targets and constraints.

5.2 Future Work

As discussed in Chapter 2, microvalve is an essential component for μGC systems and other microsystem applications. To enable the microvalve module to be used in applications that require even higher operating temperatures, thermal isolation between the die stack and housing can be created. Additionally, the packaging materials with higher temperature tolerance shall be used. These changes will enhance both heating efficiency and heating capability without compromising device lifetime, thereby enabling the device to be used at even higher temperatures in chromatography and sensing systems, such as in certain industrial settings, or in other applications, such as gas fuel delivery.

The thermal management method can be used to evaluate whether thermal isolation cutouts with different sizes, locations, and geometries can create significant impacts on the heating ramp rates and temperature uniformities of the monolithic μGC components. Moreover, with minor modification on the established model, the thermal stress induced by thermal expansion can be simulated. To improve the uniformity of detector heating, each detector shall equip its own set of heater and thermistor. This requires reallocation of electrical controls of the microcontroller. Therefore, software programming and hardware electronics need further investigation.

Appendix A:

A Piezoelectric Hybrid Valve with Three-way Control

The appendix reports a three-way valve that combines a lithographically microfabricated silicon substrate and valve seats with prefabricated piezoelectric actuators and polyimide valve membranes. The microvalve is designed for low dead volume and chemical resistance, as needed for gas chromatography (GC) systems. In contrast with valves that use microfabricated valve membranes, the incorporation of prefabricated membranes significantly simplifies manufacturing and improves the structural robustness. Further, this three-way valve provides independent open-close control for each flow path, rather than simply switching the flow from one path to the other, which is the case for most three-way valves. The overall dimension of the device is $3 \times 3 \times 1.5$ cm^3. Each flow path of the three-way valve provides a flow conductance of 4.42 sccm/kPa, a leakage conductance of 0.0012 sccm/kPa, and an overall open-close ratio of 3.68×10^3. In preliminary tests, the valve had been switched 1900 times over 24 hours without showing any performance variation. A revised microvalve made of fused silica with embedded heater has also been implemented and tested with alkanes. A chromatogram of pentane, heptane, nonane, and decane has demonstrated the chemical resistance and low dead volume of the microvalve.

A.1 Design

A. Architecture and operation

The microvalve consists of a microfabricated fluidic die stack, two prefabricated piezoelectric bimorph actuators, polyimide valve membranes (100HN, DuPont, Wilmington, DE, USA), a custom 3D printed housing (provided by CIdeas, Inc., Crystal Lake, IL, USA), four polytetrafluoroethylene (PTFE) O-rings, and two magnets (Fig. A.1). The microfabricated fluidic die stack includes three microfabricated silicon dies. Each die has a diameter of 26 mm, which matches the piezoelectric disk actuator to facilitate assembly process. The valve seats are located on the top and bottom dies, each designed in a ring geometry to fit the prefabricated piezoelectric actuator and avoid any corner that can potentially cause a dead volume. The valve seat and ring channel has a width of 500 μm and 600 μm respectively. The fluidic channels are in the middle die and designed with a width of 600 μm and a depth of 400 μm. Each die has two through holes, of which the diameter is 600 μm, to connect the flow from the middle die to the top and bottom dies. Each side of the fluidic die stack has a two-layer polyimide membrane that serves as the valve membrane. The valve membrane has the same structure as the valve membrane that is reported in chapter 2. Piezoelectric bimorph actuator is selected due to its low power consumption, fast response, and large bi-directional displacement. Two actuators (20-2235, APC. International, Ltd., Mackeyville, PA, USA) on both sides of the fluidic die stack are used to open or close the flow paths independently by bending upwards or downwards with different applied voltage polarities. Each actuator is clamped by two O-rings near the perimeter. The designed structure has an estimated dead volume of 0.96 μL.

A heater die, which consists of a thin-film heater and thermistor, is designed as an optional die for the microvalve. The heater trace follows the pattern of fluidic channels to efficiently heat

the flow path. The heater die is designated to be assembled between the top die and middle die by incorporating two through holes to allow gas flowing through.

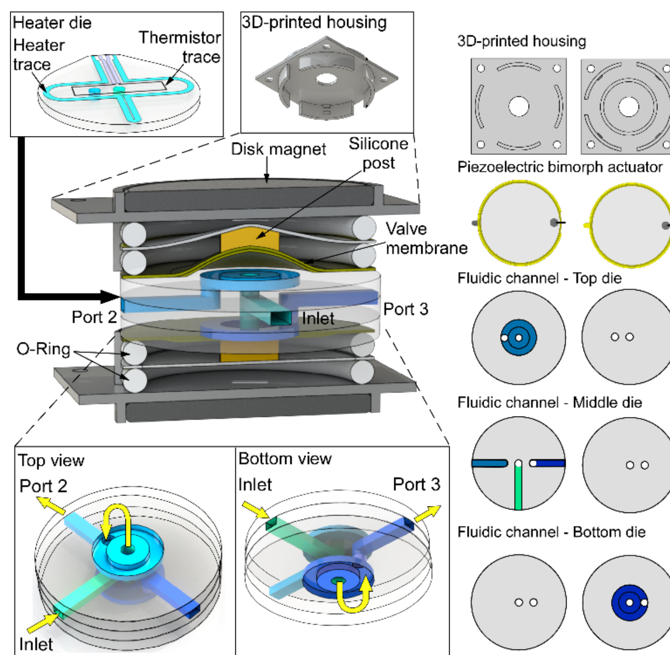

Fig. A.1: The architecture of the microvalve. The flow routing path from different perspective views are shown in the inset below. The top view and bottom view of each component are demonstrated at the right.

A silicone post is used to mechanically couple the actuator to the valve membrane. The adhesion between these components is provided by double-coated adhesive membranes (PS-1340, Polymer Science, Inc., Monticello, IN, USA). The softness of the silicone post ensures a good seal of the valve seat when closing the valve.

A custom 3D printed two-part housing is designed to accommodate the fluidic die stack and bimorph actuators with precise alignment. These components are clamped by disk magnets (ND0504-52NA, CMS Magnetics, Inc., Garland, TX, USA).

B. Characterization of the piezoelectric actuator

The overall performance and surface profile of the piezoelectric bimorph disk actuator have been characterized prior to assembly. The actuator can generate a large out-of-plane displacement of -89.4 μm to 102.9 μm with an applied voltage ranging from -80 V to 80 V (Fig. A.2a). The surface profile of the actuator was measured by a laser-confocal microscope (Fig. A.2b-c), indicating an arithmetic mean roughness (R_a) of ≈1.44 μm, a maximum height (R_z) of ≈9.7 μm, and a waviness height of ≈50 μm. The surface roughness of the actuator is tolerable, because it can be covered by an ultra-smooth valve membrane as the contact surface to the valve seat.

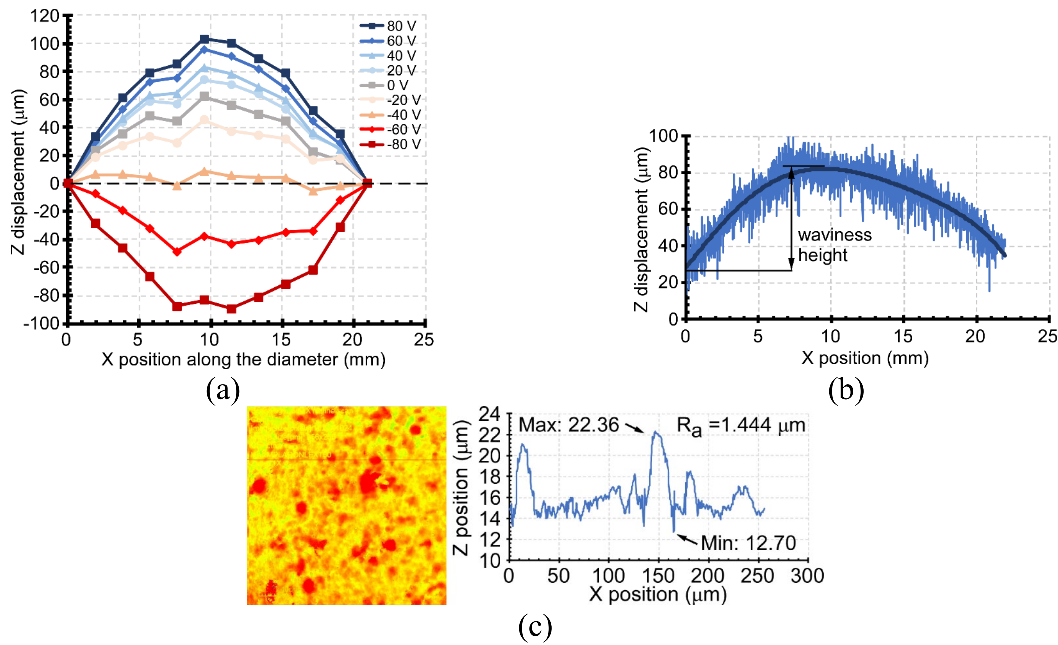

Fig. A.2: (a) The displacement generated by the bimorph actuator. (b) The waviness of the bimorph actuator. (c) 2D and 1D profile of the surface roughness of the bimorph actuator.

C. Assembly of actuator

The assembly of actuator is critical as the boundary condition has a direct impact on the displacement of the actuator. In a one-dimensional analysis, the maximum deflection of a beam with a fixed-fixed boundary condition is (Fig. A.3a -b), [Ger09]:

$$y_{fix}^{\max} = \frac{w_f L_{beam}{}^4}{384EI} \quad \text{(A.1)}$$

where w_f is distributed force, E is young's modulus, L_{beam} is beam length, and I is second moment of area. With a simply-supported boundary condition (Fig. A.3c-d), the maximum deflection of a beam is:

$$y_{simp}^{\max} = \frac{5w_f L_{beam}{}^4}{384EI} \quad \text{(A.2)}$$

With both ends being simply supported, which allows the beam to rotate around the anchored point, the maximum deflection is 5 times larger. Therefore, two rigid O-rings are used to sandwich the actuator. The rigidity of the O-rings is a critical factor that determines the boundary condition of the actuator. Rigid O-rings provide a simply-supported boundary condition, whereas softer O-rings tend to change the boundary condition to a fixed-fixed condition, which substantially reduces the actuator displacement. In addition, the maximum deflection is proportional to the quadruple of L_{beam}. This implies that the actuator needs to be supported at the perimeter with minimal contact with the supporting structure. It is experimentally verified that the actuator supported by soft O-rings did not provide sufficient displacement to open the valve.

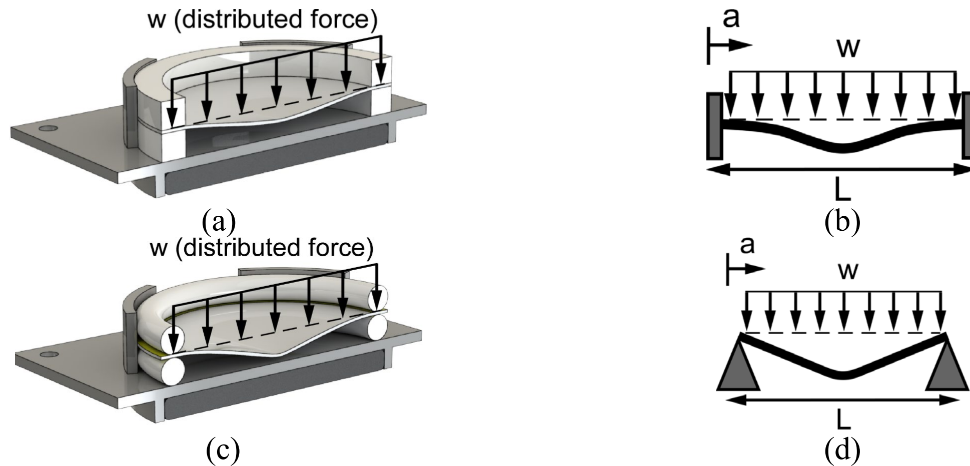

Fig. A.3: (a) 3D demonstration of actuator assembly with a fixed-fixed boundary condition. (b) Analogous 2D demonstration of beam deflection with a fixed-fixed boundary condition. (c) 3D demonstration of actuator assembly with a simply-supported boundary condition. (d) Analogous 2D demonstration of beam deflection with a simply-supported boundary condition.

D. Prefabricated polyimide valve membrane

The valve membrane must provide a chemically inert surface, leak-free mating with the valve seat, sufficient flexibility for low force actuation and dust tolerance, and infrangibility for assembly and repeated uses. To meet all these requirements, several chemically inert and flexible membranes have been investigated. The surface profile of a fluorinated ethylene propylene (FEP) membrane (FEP 200C, DuPont, Wilmington, DE, USA) and a polyimide membrane (100HN, DuPont, Wilmington, DE, USA) have been shown in Fig. A.4. It can be seen that there are irregular scratches on the FEP membrane, of which R_z could reach ≈7 µm. This surface roughness can lead to significant leakage during valve closure. In contrast, the polyimide membrane demonstrated an ultra-low surface roughness, of which R_a is 17 nm. In addition, polyimide can be laminated with adhesive on each side to facilitate assembly process. Therefore, polyimide is selected as the prefabricated valve membrane because of its chemical resistance, ultra-low surface roughness, and ease of assembly.

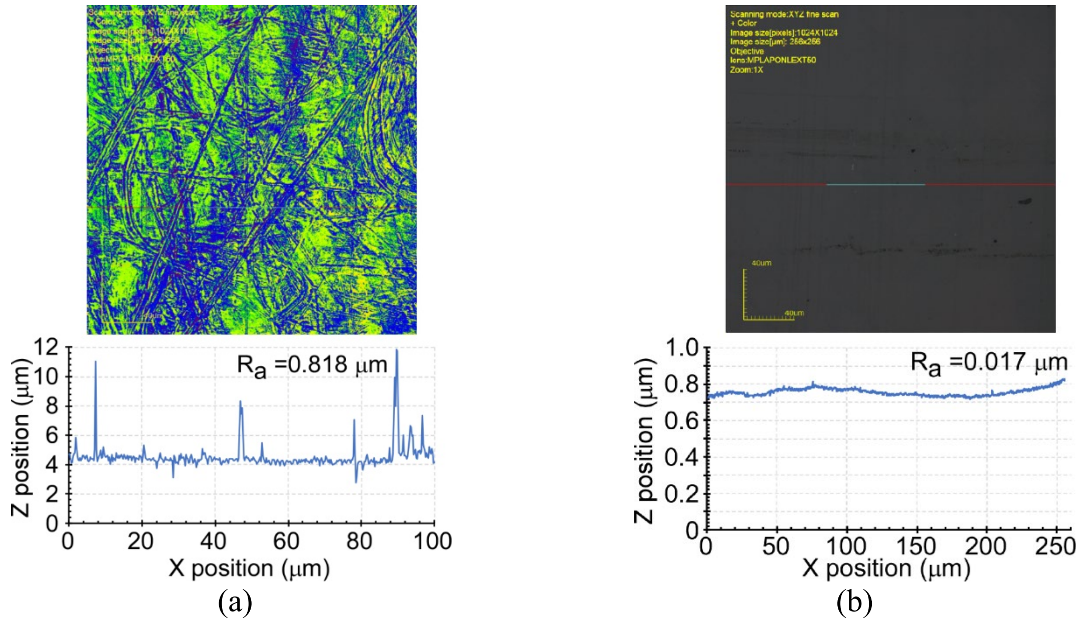

Fig. A.4: (a) Surface profile of FEP membrane. (b) Surface profile of polyimide membrane.

A.2 Fabrication and Assembly

The dies in the fluidic die stack are fabricated[6] on a 6-inch 675 μm-thick silicon wafer using the deep reactive ion etching (DRIE) process with two lithographic masks (Fig. A.5). The top-side DRIE creates 400 μm-deep channels, whereas the bottom-side DRIE creates through holes. A total of 18 dies can be fabricated on a 6-inch wafer.

The fluidic die stack is formed by bonding three silicon dies using a low-viscosity epoxy (Epotek 377, Epoxy Technology Inc., Billerica, MA, USA) (Fig. A.6a). Capillary tubes are attached to the ports using a high-viscosity epoxy (Stycast2850FT, Henkel, Düsseldorf, Germany).

During the assembly, the PTFE O-rings and piezoelectric bimorph actuators are assembled into the housing. Double-coated adhesive membranes are attached to the silicone post for adhesion to the actuators and the fluidic die stack. The size of the assembled device is 3 × 3 × 1.5 cm^3 (Fig. A.6b).

[6] Part of the valve fabrication was performed by Mr. Tsenguun Byambadorj.

(a) (b)

Fig. A.5: Fabrication steps of the silicon fluidic dies (a) Front-side DRIE. (b) Back-side DRIE.

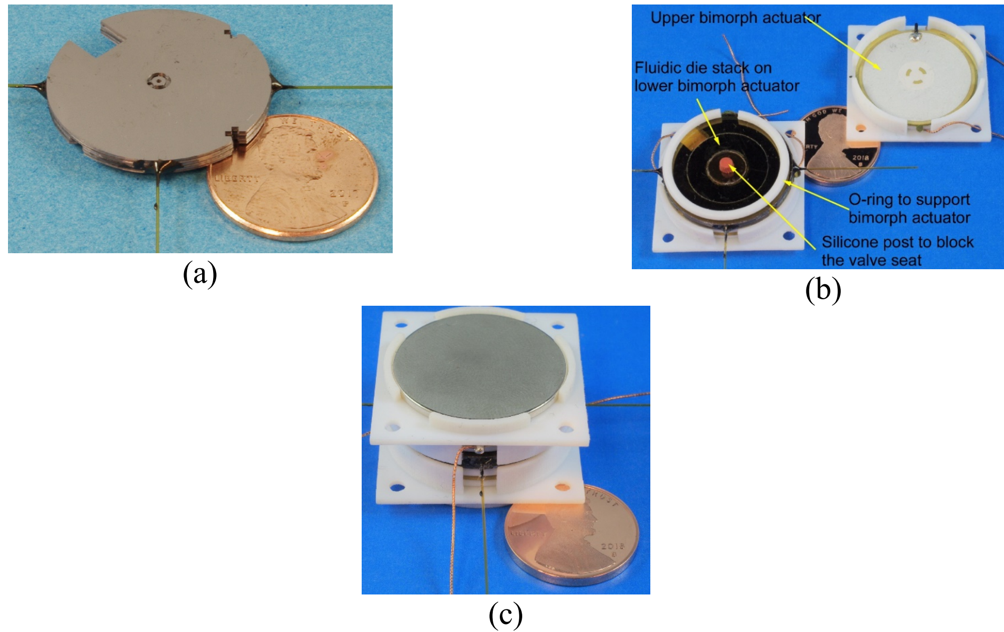

(a) (b) (c)

Fig. A.6: (a) The fluidic die stack is assembled from lithographically microfabricated silicon dies. (b) Partial assembly of the valve. (c) Final view of assembly.

A.3 Experimental Results

A. Flow conductance tests

The setup introduced in Chapter 2 was utilized to characterize the fluidic performance of the monolithic valve modules (Fig. A.7). The only difference was that the valve under test was changed from a two-way valve to a three-way valve.

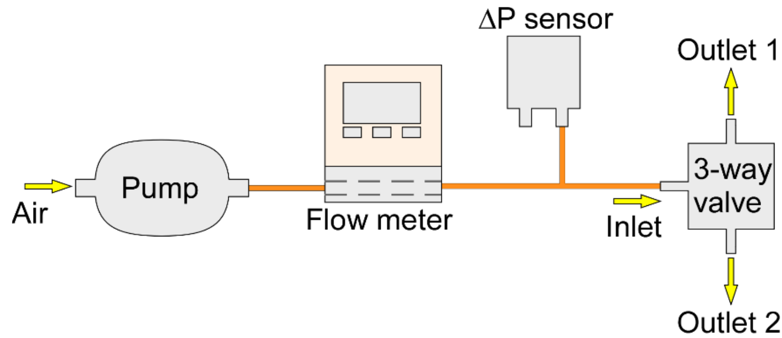

Fig. A.7: The test setup used to characterize the fluidic performance of the valve.

A customized printed circuit board (PCB) was used to provide direct current (DC) actuation voltages that can be tuned from -200 V to 200 V. The circuit schematic is shown in Fig. A.8. The input voltage, of which the range can be tuned from 0-12 V by a potentiometer, was supplied to an operational amplifier that served as a voltage follower (Fig. A.8). The DC-DC converter then boosted the input voltage from a range of 0 to12 V to a range of -200 to 200 V (*i.e.,* converted voltage). A voltage divider was used to create the center point of the converted voltage. One end of the piezoelectric actuator was connected to the center point of the converted voltage, whereas the other end of the piezoelectric actuator was connected to either the positive or negative converted voltage. Two stages of relays were used: the first stage relays (*i.e.,* Relay A1 and Relay A2) connect either the positive of the negative converted voltage to each valve, whereas the second stage relays (*i.e.,* Relay B1 and Relay B2) select between these two voltages. In this circuit, a maximum of 200 V or -200 V can be supplied to each piezoelectric actuator independently. All the relays were controlled by a data acquisition system (DAQ) (USB-6363 OEM, National Instruments, Austin, TX, USA). During the experiments, both piezoelectric actuators were applied with the same voltage magnitudes, whereas the voltage polarity was used to control the opening or closing of each flow path. In the preliminary reliability test, the valve was automatically

controlled by a LabVIEW® program while the flow rate was monitored over the whole testing period.

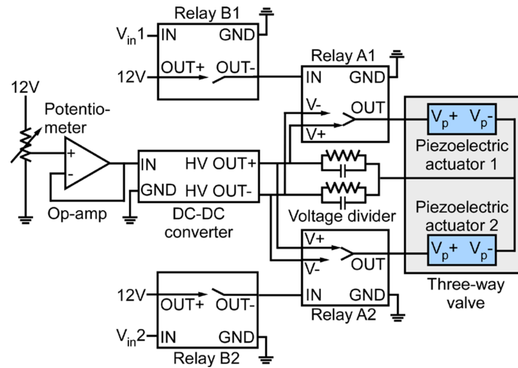

Fig. A.8: The circuit schematic for the control of the piezoelectric bimorph actuators.

With a given actuation voltage of 70 V, when one of the outlets was opened whereas the other was closed, the flow rate through the valve increased proportionally with the applied pressure drop over a tested range from -0.6 kPa to 1 kPa (Fig. A.9a). The flow conductance of the valve was 4.42 sccm/kPa, as indicated by the slope of the proportional relationship between the flow rate and the pressure drop. Both outlets showed similar flow conductance. With a given actuation voltage of 70 V, when both outlets were closed, the leakage flow rate was measured over a pressure drop range from -8.4 kPa to 10 kPa (Fig. A.9b). The leakage conductance was around 0.0012 sccm/kPa. The open-close ratio of flow conductance was 3.68×10^3.

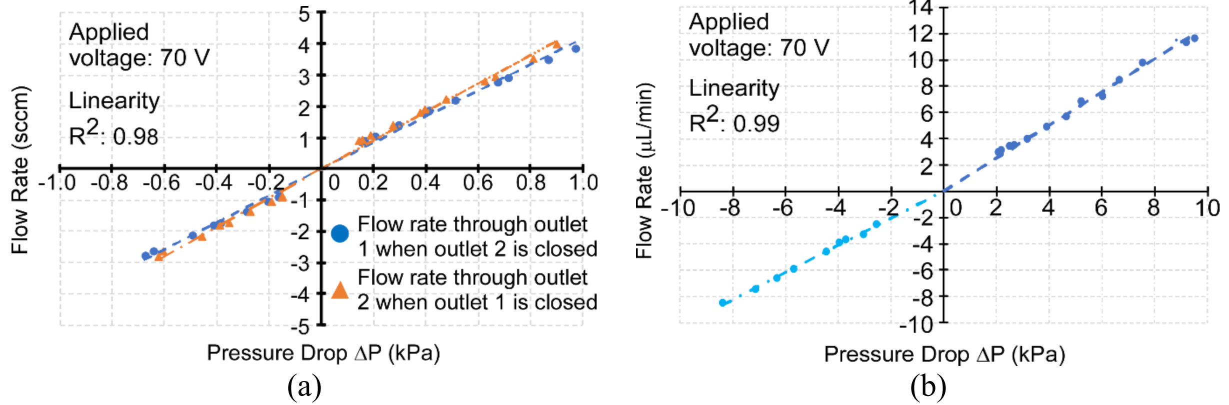

Fig. A.9: (a) Flow rates under various inlet pressure drops. The measurements were done for both outlets. While one port was tested, the other one remained closed. The actuated voltage was 70 V. (b) Leakage flow when the valve was fully closed. The valve was tested up to 10 kPa

The effect of actuation voltage on the flow rate was measured over a voltage range from -80 V to 80 V and a blocking pressure range of 0-8.5 kPa. (Fig. A.10a). The flow rate started decreasing at 20 V and dropped to zero at -20 V. The hysteresis phenomenon from the piezoelectric actuator was observed by cycling the actuation voltage between 80 V and -80 V. Typical hysteresis occurred between 0 V and 60 V (Fig. A.10b).

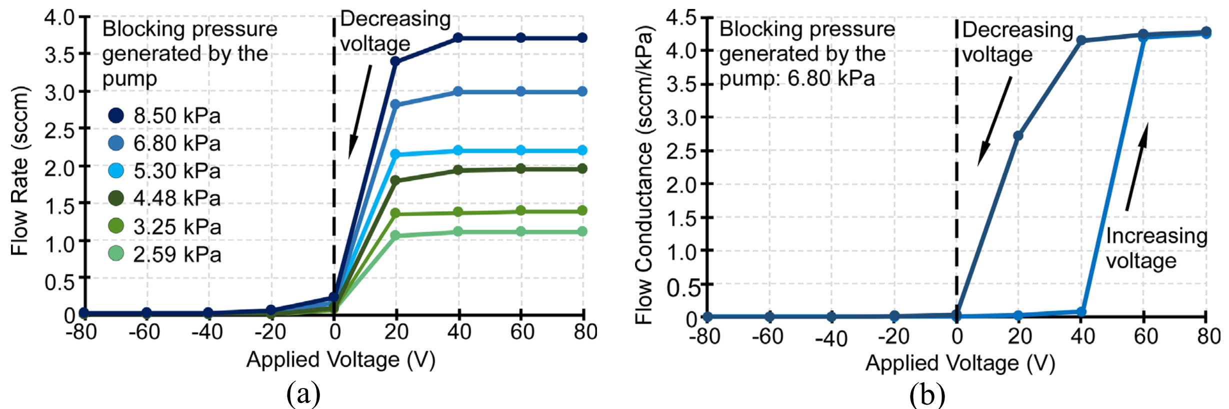

Fig. A.10: (a) The change of flow rate at different applied voltages. (b) Flow conductance as a function of voltage when tested at a blocking pressure of 6.80 kPa, illustrating hysteresis from the piezoelectric actuator.

In a preliminary reliability test, one outlet was constantly closed by a voltage of -80 V, whereas the other outlet was switched closed and open periodically between 80 V and -80 V, respectively. During each cycle, the valve was opened for 15 s and closed for 30 s. The valve was maintained at closure for a longer period to compensate the fluidic time constant of the test setup. The microvalve showed stable performance over 1900 switches that lasted more than 24 hours (Fig. A.11).

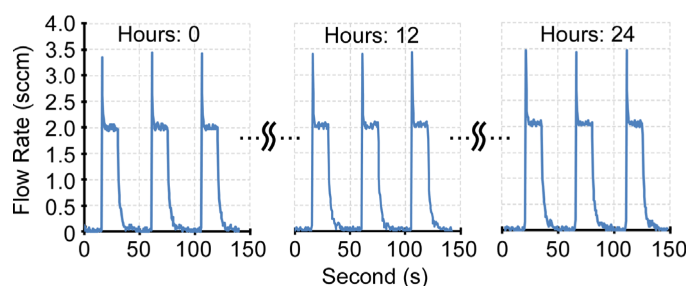

Fig. A.11: Continuous operation of the microvalve was tested by toggling one port at a period of 45 seconds while maintaining the other port to be closed. The actuation voltage was 80 V. The applied blocking pressure was 5.1 kPa.

B. Chemical injection tests

The impact of the valve on chromatographic peaks was evaluated using a similar test setup (Fig. 2.17) that is introduced in Chapter 2. Two modifications that were implemented on the test setup are: 1) a separation column with 1 m length, 250 µm inner diameter, and 0.1 µm thick OV-1 stationary phase coating (115-2501, Ohio Valley Specialty Company, Marietta, OH, USA) was selected due to its selectivity for the intended analytes, and 2) the valve under test was located outside the benchtop GC oven connected along the flow path, downstream of the inlet and upstream of the separation column and the FID at room temperature. The experiments included two test cases. In Case 1, the valve was connected in series with the separation column and the FID, whereas in Case 2, the valve was removed from the flow path. The resulting chromatograms

from both cases were generated and overlaid to evaluate the peak distortion effects caused by the valve.

In the overall chromatograms, no noticeable peak broadening effect or distortion were observed (Fig. A.12a). To compensate for the minor run-to-run variation in the test setup, the retention peaks in the raw chromatograms were normalized in the peak amplitude and aligned in the time axis for better comparison (Fig. A.12b). The shape of the normalized and shifted nonane peak remained nearly unaffected by the valve. The test results validated the chemical resistance and low dead volume of the valve.

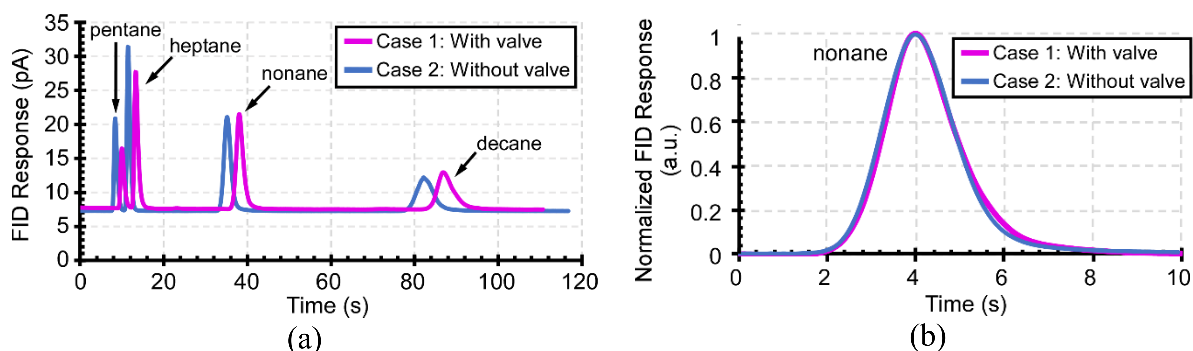

Fig. A.12: The chromatogram of non-polar chemical analytes. (a) An overall chromatogram of four non-polar chemical analytes under two test cases. (b) Normalized and shifted nonane peak.

A.4 Discussion and Conclusion

This chapter demonstrates a three-way microvalve with facile fabrication and assembly processes. The incorporation of micromachined fluidic die stack and prefabricated polyimide membranes simplifies manufacturing and provides high robustness. The microvalve provides a high open-close ratio of flow conductance of 3.68×10^3.

The microvalve is operated in the binary mode (*i.e.*, with each path switched between fully open and fully closed) to eliminate the impact of hysteresis from the piezoelectric actuator. The power consumption of the valve is about 0.78 mJ per switch, which is estimated using the

capacitance of the actuator and applied voltage. There is nearly no power consumption at the idle state. Moreover, unlike common three-way valves where the flow can only be toggled between two flow paths, the independent control for each flow path of this three-way valve enables additional application scenarios.

Chemical injection tests have also been performed to demonstrate the chemical resistance and low dead volume of the valve. In the overall chromatograms, the retention peaks remain nearly identical when the valve is fluidically connected.

The major challenge with the piezoelectric microvalve is the overall miniaturization of arrays of microvalves. The downsizing of the microvalve footprint is limited by the footprint of the commercial piezoelectric bimorph actuator. This can be solved by switching to a different actuation mechanism; however, the flow open-close ratio, chemical resistance, and low dead volume should still be maintained.

Appendix B:

Additional Thermal Modeling Results of Monolithic Microscale Gas Chromatography Components

The additional thermal modeling results of the MPCA1 chip are presented in Appendix B. The presented components include the carrier gas filter, Column2, and Column3.

Carrier gas filter

The heating ramp rates, current consumptions, and temperature distributions of the carrier gas filter are shown in Fig. B.1. The electrical and thermal characteristics are summarized in Table B.1. In 3 s of heating, the carrier gas filter demonstrates heating ramp rates of 69.2 °C/s in the MPCA1 chip, 76.4 °C/s in the MPCA2-A chip, and 51.0 °C/s in the MPCA2-B chip. When the filter is heated, the south edges of Column1 remain <25°C in the MPCA1 and MPCA2-A chips, whereas it reaches 57.1°C in the MPCA2-B chip. The temperature variation across the sorbent area is 73.9°C in the MPCA1 chip. After the heater revision, the temperature variations are reduced to 21.4°C and 14.5°C in the MPCA2-A and MPCA2-B chips, respectively.

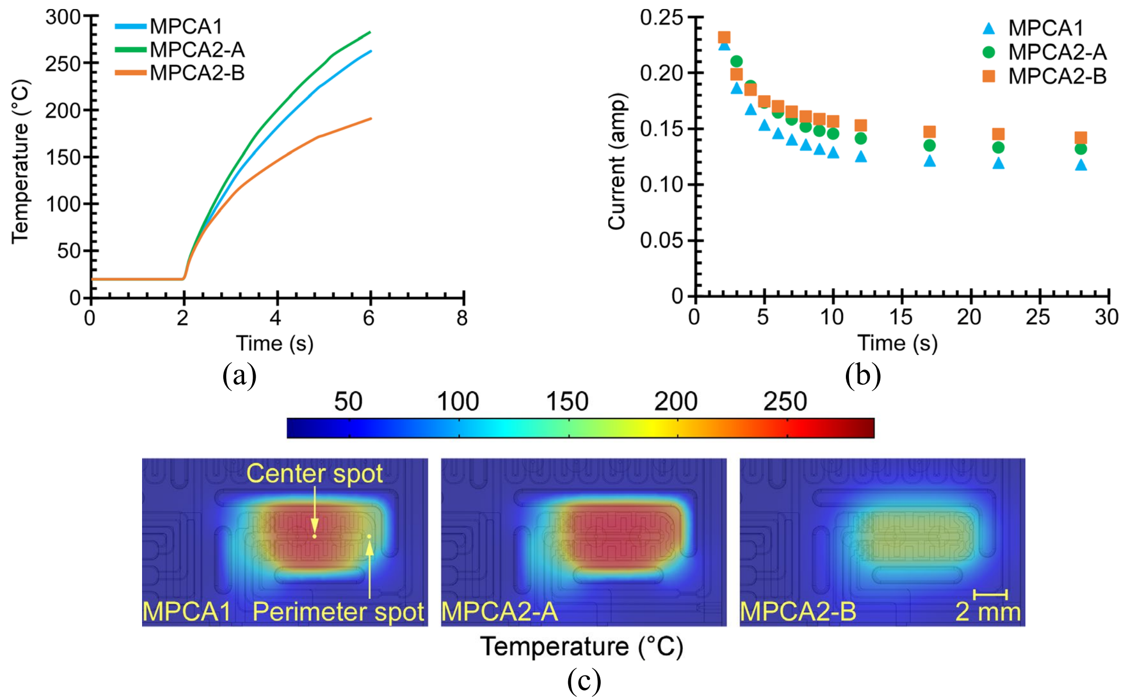

Fig. B.1: The simulated thermal characteristics of the carrier gas filter in three different designs. (a) The simulated transient responses. (b) The simulated current consumptions. (c) The simulated temperature distributions after 3 s of heating.

Table B.1: Heating power and thermal characteristics of the carrier gas filter in 3 s.

Chip Design	Power (W)	Ramp rate (°C)	σ (std. dev.) (°C)	σ (std. dev.) (%)	Cen. (°C)	Per. (°C)	Var. (°C)	Var. (%)
MPCA1	5.93	69.2	27.5	13.5	243.9	170	73.9	35.6
MPCA2-A	6.78	76.3	9.8	4.3	249.7	228.3	21.4	9.3
MPCA2-B	6.08	51.0	7.1	4.6	173.4	158.9	14.5	9.5

Column2

The current consumptions and temperature distributions of Column2 are shown in Fig. B.2. The electrical and thermal characteristics are summarized in Table B.2. In 50 s of heating, Column2 shows heating ramp rates of 0.84 °C/s in the MPCA1 chip, 1.24 °C/s in the MPCA2-A chip, and 0.92 °C/s in the MPCA2-B chip, respectively. Because Column2 has thermal isolation cutouts allocated at all four edges, the absence of thermal isolation cutouts (*i.e.,* the MPCA2-B chip) results in a large reduction in the heating ramp rates. The MPCA1 chip cannot reach 70°C because of the insufficient heating power; the MPCA2-B chip cannot reach 70°C because of the

absence of the cutouts. This proves that both higher heating power and thermal isolation cutouts are essential. For the temperature uniformity, the MPCA1 and MPCA2-A chips have temperature variations that are smaller than 3°C, whereas the MPCA2-B chip has a temperature variation of 9.3°C.

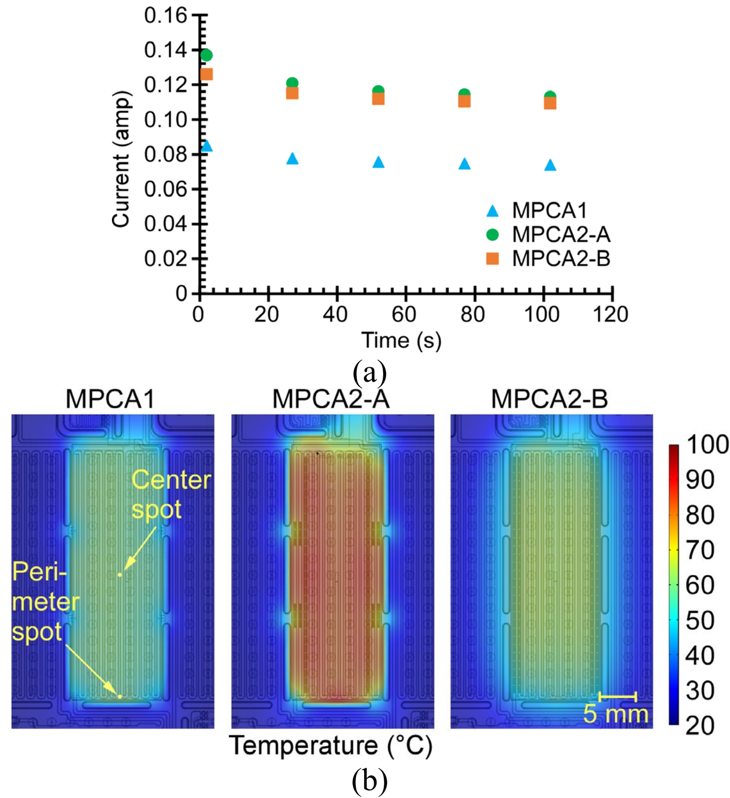

Fig. B.2: (a) The simulated current consumptions of Column2. (b) The simulated temperature distributions of Column2 after 50 s of heating.

Table B.2: Heating power and thermal characteristics of Column2 in 50 s.

Chip Design	Power (W)	Ramp rate (°C/s)	σ (std. dev.) (°C)	σ (std. dev.) (%)	Cen. (°C)	Per. (°C)	Var. (°C)	Var. (%)
MPCA1	2.04	0.84	4.8	12.5	63.2	61	2.2	5.3
MPCA2-A	3.29	1.24	6.2	10.3	82.8	83.9	1.1	1.8
MPCA2-B	3.03	0.92	4.7	10.8	66.2	56.9	9.3	20.3

Column3

The current consumptions and temperature distributions of Column3 are shown in Fig. B.3. The electrical and thermal characteristics are summarized in Table B.3. In 50 s of heating, Column3 has heating ramp rates of 0.78 °C/s in the MPCA1 chip, 1.18 °C/s in the MPCA2-A chip, and 1.04 °C/s in the MPCA2-B chip, respectively. The MPCA2-A chip has the highest heating ramping rate, followed by the MPCA1 chip, and the MPCA2-B chip. The MPCA1 chip cannot reach the targeted heating ramp rate of 1 °C/s because of the insufficient heating power. The temperature variations of the MPCA1 and MPCA2-A chips are smaller than 4°C, whereas the temperature variation of the MPCA2-B reaches 11.2°C.

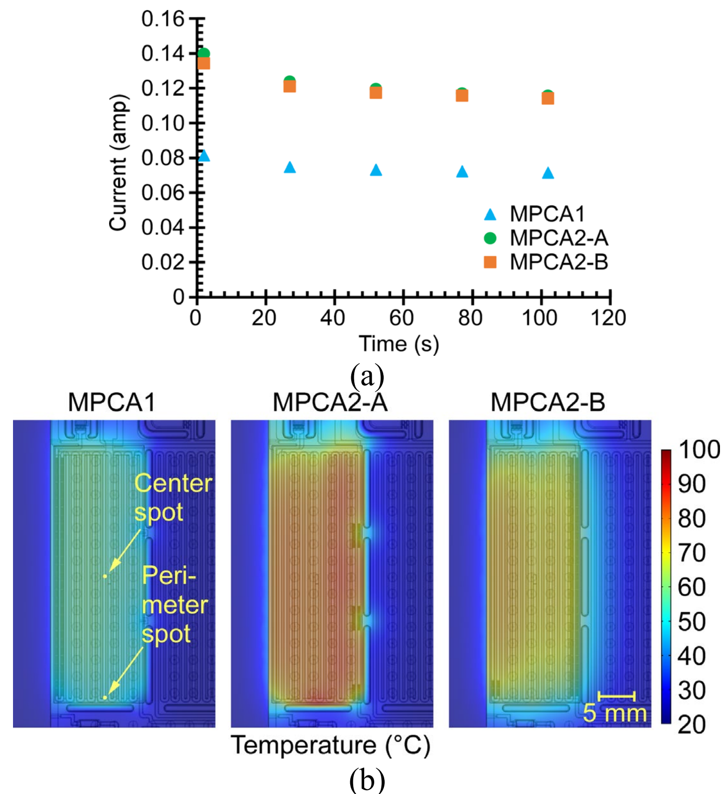

Fig. B.3: (a) The simulated current consumptions of Column3. (b) The simulated temperature distributions of Column3 after 50 s of heating.

Table B.3: Heating power and thermal characteristics of Column3 in 50 s.

Chip Design	Power (W)	Ramp rate (°C/s)	σ (std. dev.) (°C)	σ (std. dev.) (%)	Cen. (°C)	Per. (°C)	Var. (°C)	Var. (%)
MPCA1	1.96	0.78	4.0	10.8	60.2	56.2	4.0	10.2
MPCA2-A	3.37	1.18	6.4	11.4	80.1	83.4	3.3	5.6
MPCA2-B	3.24	1.04	5.5	11.5	72.6	61.4	11.2	21.5

References

[Aga05] M. Agah, J. A. Potkay, G. Lambertus, R. Sacks, and K. D. Wise, "High-performance temperature-programmed microfabricated gas chromatography columns," *Journal of Microelectromechanical Systems,* vol. 14, no. 5, pp. 1039-50, 2005.

[Akb15] M. Akbar, H. Shakeel, M. Agah, "GC-on-chip: integrated column and photoionization detector," *Lab on a Chip*, vol. 15, pp. 1748-1758, 2015.

[An15] S. An, Y. Qin and Y. B. Gianchandani, "A Monolithic High-Flow Knudsen Pump Using Vertical Al2O3 Channels in SOI," in *J. Microelectromech. Syst*, vol. 24, no. 5, pp. 1606-1615, Oct. 2015.

[Bae07] B. Bae, J. Han, R. I. Masel, M. Shannon, "A Bidirectional Electrostatic Microvalve With Microsecond Switching Performance," *J. Microelectromech. Syst*. vol. 16, no. 6, pp. 1461–1471, Dec. 2007.

[Bar12] J. Barth, C. Megnin and M. Kohl, "A Bistable Shape Memory Alloy Microvalve With Magnetostatic Latches," *J. Microelectromech. Syst*, vol. 21, no. 1, pp. 76–84, Feb. 2012.

[Ber95] P. L. Bergstrom, Jin Ji, Yu-Ning Liu, M. Kaviany and K. D. Wise, "Thermally driven phase-change microactuation," *J. Microelectromech. Syst*, vol. 4, no. 1, pp. 10–17, March 1995.

[Bir03] J. O. Bird, *Electrical Circuit Theory and Technology (Chapter 13), 2nd Version*, Newnes, 2001.

[Böh00] S. Böhm, G. J. Burger, M.T. Korthorst, and F. Roseboom, A micromachined silicon valve driven by a miniature bi-stable electro-magnet actuator," *Sensors and Actuators A: Physical,* vol. 80, no. 1, pp. 77–83, Mar. 2000.

[Bon08] U. Bonne, "Gas sensors," in *Comprehensive Microsystems*, vol. 2, Elsevier B.V., pp. 375–432, 2008.

[Bos93] D. Bosch, B. Heimhofer, G. Muck, H. Seidel, U. Thumser, W. Welser, "A silicon microvalve with combined electromagnetic/electrostatic actuation," *Sensors and Actuators A: Physical*, vol. 37–8, pp. 684–692, Jun. 1993

[Bro98] M. A. Brown, K. A. Brix, "Review of health consequences from high-, intermediate- and low-level exposure to organophosphorus nerve agents," *J. Appl. Toxicol*. Vol. 18, pp. 393–408, 1998

[Bru07] H. Bruss, "Hydraulic resistance and compliance," In *Theoretical Microfluidics*, Oxford University Press: Oxford, UK, pp. 71–91, 2007

[Cap00] M. Capanu, J. G. Boyd IV, and P. J. Hesketh, "Design, Fabrication, and Testing of a Bistable Electromagnetically Actuated Microvalve," *J. Microelectromech. Syst*., vol. 9, no. 2, pp.181–189, Jun. 2000.

[Che17] Q. Cheng, Y. Qin and Y. B. Gianchandani, "A bidirectional Knudsen pump with superior thermal management for micro-gas chromatography applications," *2017 IEEE 30th International Conference on Micro Electro Mechanical Systems (MEMS)*, Las Vegas, NV, 2017, pp. 167-170.

[Col14] W. R. Collin, G. Serrano, L. K. Wright, H. Chang, N. Nunovero, and E. T. Zellers, "Microfabricated gas chromatograph for rapid, trace-level determinations of gas-phase explosive marker compounds," *Anal. Chem*. vol. 86, no. 1, pp. 655–663, 2014.

[Col16] W. R. Collin, K. W. Scholten, X. Fan, D. Paul, K. Kurabayashi, E. T. Zellers, "Polymer-coated micro-optofluidic ring resonator detector for a comprehensive two-dimensional gas chromatographic microsystem: μGC × μGC- μOFRR," *Analyst*, vol. 141, pp. 261–269, 2016.

[Dun89] A. B. Duncan, G. P. Peterson, and F. S. Fletcher, "Effective Thermal Conductivity Within Packed Beds of Spherical Particles," *Journal of Heat Transfer*, vol. 111, no. 4, pp. 830-836, 1989.

[Erg52] S. Ergun, "Fluid flow through packed columns," *Chem. Eng. Prog*., pp. 48, 1952

[Esa89] M. Esashi, S. Shoji, and A. Nakano, "Normally closed valve microvalve and micropump fabricated on a silicon wafer," *Sensors and Actuators*, vol. 20, no. 1–2, pp. 163–169, Nov. 1989.

[Fol83] J. P. Foley, J. G. Dorsey, "Equations for calculation of chromatographic figures of merit for ideal and skewed peaks," *Anal. Chem.* vol. 55, no. 4, pp. 730–737, Apr. 1983.

[Fu03] C. Fu, Z. Rummler, W. Schomburg, "Magnetically driven micro ball valves fabricated by multilayer adhesive film bonding," *J. Micromech. Microeng*. vol. 13, no. 4, pp. S96–S102, Jul. 2003.

[Fur01] E. P. Furlani, *Permanent Magnet and Electromechanical Devices (Chapter 3)*, Elsevier Inc., 2001.

[Fas05] P. Fastyn, W. Kornacki, T. Gierczak, J. Gawłowski, J. Niedzielski, "Adsorption of water vapour from humid air by selected carbon adsorbents," *Journal of Chromatography A*, vol. 1078, pp. 7-12, 2005

[Gaw01] M. Gawryś, P. Fastyn, J. Gawlowski, T. Gierczak, J. Niedzielski, "Prevention of water vapour adsorption by carbon molecular sieves in sampling humid gases," *J. Chromatogr. A*, vol. 933, pp. 107–116, 2001.

[Ger09] J. M. Gere, B. J. Goodno, *Mechanics of Materials: 7th Edition (Chapter 9)*, CL Engineering, 2009.

[Gro08] W. H. Grover, M. G. von Muhlen, S. R. Manalis, "Teflon films for chemically-inert microfluidic valves and pumps," *Lab Chip*, vol. 8, pp. 913–918, 2008.

[Gro15] M. S. Groen, D. M. Brouwer, J. C. Lötters, R. J. Wiegerink, "Miniature proportional control valve with top mounted piezo bimorph actuator with millisecond response time," *J. Micromech. Microeng*. vol. 25, no. 10, 105008, Sep. 2015.

[Gar15] A. Garg, M. Akbar, E. Vejerano, S. Narayanan, L. Nazhandali, L. C. Marr, M. Agah, "Zebra GC: A mini gas chromatography system for trace-level determination of hazardous air pollutants," *Sensors Actuators B. Chemical,* vol. 212, pp. 145–154, 2015.

[Gor12] R. J. M. Gordenker, K. D. Wise, "A programmable palm-size gas analyzer for use in micro autonomous systems," *Proc. SPIE*, vol. 8373, 83731O, 2012.

[Hes04] P. J. Hesketh, J. S. Bintoro, and R. Luharuka, "Microvalve for Fuel Cells and Miniature Gas Chromatographic System," *Sensors Update*, vol. 13, pp. 233–302, Feb. 2004

[Inc07] F. P. Incropera, D. P. Dewitt, T. L. Bergmann, and A. S. Lavine, *Fundamentals of Heat and Mass Transfer: 6th Edition (Chapter 1, 3),* 2007.

[Jer94] H. Jerman, "Electrically activated normally closed diaphragm valves," *J. Micromech. Microeng*, vol. 4, n. 4, pp. 210–16, 1994.

[Ji91] J. Ji, J. Chaney, M. Kaviany, P. L. Bergstrom and K. D. Wise, "Microactuation based on thermally-driven phase-change," TRANSDUCERS '91: *1991 International Conference on Solid-State Sensors and Actuators*, Digest of Technical Papers, San Francisco, CA, USA, 1991, pp. 1037–1040.

[Kaa10] B.C. Kaanta, H. Chen, X. Zhang, "A monolithically fabricated gas chromatography separation column with an integrated high sensitivity thermal conductivity detector," *Journal of Micromechanics and Microengineering*, vol. 20, pp. 055016, 2010.

[Kim08] H. Kim and K. Najafi, "Electrostatic hydraulic three-way gas microvalve for high-pressure applications," *Proc. 12th Int. Conf on Miniaturized Systems for Chemistry and Life Sciences (uTAS '08)*, San Diego, California, USA, Oct. 12-16, 2008, pp. 369–371.

[Kim11] S. K. Kim, H. Chang, and E. T. Zellers, "Microfabricated gas chromatograph for the selective determination of trichloroethylene vapor at sub-parts-per-billion concentrations in complex mixtures," *Anal. Chem*. vol. 83, no. 18, pp. 7198–7206, 2011.

[Koh99] M. Kohl, K. D. Skrobanek, and S. Miyazaki, "Development of stress-optimised shape memory microvalves," *Sensors and Actuators A: Physical*, vol. A72, n. 3, pp. 243–50, 1999.

[Koh00] M. Kohl, D. Dittmann, E. Quandt, and B. Winzek, "Thin film shape memory microvalves with adjustable operation temperature," *Sensors and Actuators A: Physical*, vol. A83, n. 1–3, pp. 214–19, 2000.

[Lee16] J. Lee, M. Zhou, H. Zhu, R. Nidetz, K. Kurabayashi, and X. Fan, Fully Automated Portable Comprehensive 2-Dimensional Gas Chromatography Device," *Anal. Chem*. vol. 88, no. 20, pp. 10266–10274, 2016.

[Lef13] R. Lefevre, A. Salette, C. Agraffeil, J. Guillen, C. Déhan, P. Morfouli, and L. Montès, "Numerical study of bimetallic actuated micro-membrane with large deformations," *J. Micromech. Microeng.* vol. 23, no. 1, 2013.

[Lew06] P. R. Lewis, R. P. Manginell, D. R. Adkins, R. J. Kottenstette, D. R. Wheeler, S. S. Sokolowski, D. E. Trudell, J. E. Byrnes, M. Okandan, J. M. Bauer, R. G. Manley, G. C. Frye-Mason, "Recent Advancements in the Gas-Phase MicroChemLab," *IEEE Sensors Journal*, vol. 6, no. 3, pp. 784–795, 2006.

[Lia17] W. Liao, X. Zhao, H-T. Lu, Y. Qin, Y.B. Gianchandani, "Progressive Cellular Architecture in Gas Chromatograph for Broad Vapor Sensing," *Chemical and Biological Defense Science & Technology (CBD S&T) Conference*, Long Beach, CA, Nov. 2017.

[Lia21a] W. Liao, X. Zhao, H-T. Lu, T. Byambadorj, Y. Qin, Y.B. Gianchandani, "Progressive Cellular Architecture in Gas Chromatograph for Broad Vapor Chemical Analyse," *Sensors,* vol. 21, pp. 3089, 2021.

[Lia21b] W. Liao, H-T. Lu., I.L. Ibeas, X. Zhao, D. Winship, Q. Xu, T. Qian, Y. Qin, Y.B. Gianchandani, "Monolithic Integration of a 3-Cell µGC (Array) with in-Line Photoinoization Detectors," *manuscript in preparation*

[Lu18] H.-T. Lu; Y. Qin, Y.B. Gianchandani, "A Hybrid Three-Way Valve For Gas Chromatography Systems," *In Proceedings of the 2018 IEEE Sensors Conference*, New Delhi, India, 2018, pp. 1-4

[Lu21] H.-T. Lu; Y. Qin, Y.B. Gianchandani, "A Microvalve Module with High Chemical Inertness And Embedded Flow Heating for Microscale Gas Chromatography," *Sensors,* vol. 21, pp. 632, 2021.

[Luo11] X. Luo, W. Zhu, B. Mitra, J. Liu, T. Liu, X. Fan, Y. Gianchandani, "A Chemical Detector for Gas Chromatography Using Pulsed Discharge Emission Spectroscopy on a Microchip," *American Geophysical Union, Fall Meeting*, San Francisco, CA, Dec. 2011.

[Man11] R.P. Manginell, J.M. Bauer, M.W. Moorman, L.J. Sanchez, J.M. Anderson, J.J. Whiting, D.A. Porter, D. Copic, K.E. Achyuthan, "A monolithically-integrated µGC chemical sensor system," *Sensors*, vol. 11, pp. 6517-6532, 2011.

[Mes98] S. Messner, M. Muller, V. Burger, J. Schaible, H. Sandmaier, and R. Zengerle, "A normally–closed, bimetallically actuated 3-way microvalve for pneumatic applications," *Eleventh*

Annual International Workshop on Micro Electro Mechanical Systems. An Investigation of Micro Structures, Sensors, Actuators, Machines and Systems, pp. 40–4, 1998.

[Mls06] T. E. Mlsna, S. Cemalovic, M. Warburton, S. T. Hobson, D. A. Mlsna, S. V. Patel, "Chemicapacitive microsensors for chemical warfare agent and toxic industrial chemical detection," *Sensors and Actuators B: Chemical*, vol. 116, no. 1–2, pp. 192–201, Jul. 2006.

[Mit97] M. B. Mitchell, V. N. Sheinker, A. E. Mintz, "Adsorption and decomposition of dimethyl methylphosphonate on metal oxides," *J. Phys. Chem.,* vol. 101, pp. 11192–11203, 1997

[Mit08] B. Mitra and Y. B. Gianchandani, "The Detection of Chemical Vapors in Air Using Optical Emission Spectroscopy of Pulsed Microdischarges From Two- and Three- Electrode Microstructures," *IEEE Sensors Journal,* vol. 8, no. 8, pp. 1445-1454, 2008.

[Nar13] S. Narayanan, M. Agah, "Fabrication and characterization of a suspended TCD integrated with a gas separation column," *Journal of Microelectromechanical Systems*, vol. 22, no. 5, p. 1166-1173, 2013.

[Nav15] M. Navaei, A. Mahdavifar, J.-M.D. Dimandja, G. McMurray, P.J. Hesketh, "All silicon micro-GC column temperature programming using axial heating," *Micromachines*, vol. 6, pp. 865-878, 2015.

[Oh06] K.W. Oh, C.H. Ahn, "A review of microvalves," *J. Micromech. Microeng*. vol. 16, no. 5, pp. R13–R39, May. 2006.

[Par08] J.M. Park, R.P. Taylor, A.T. Evans, T.R. Brosten, G.F. Nellis, S.A. Klein, J.R. Feller, L. Salerno, Y.B. Gianchandani, "A piezoelectric microvalve for cryogenic applications," *J. Micromech. Microeng.* vol. 18, no. 1, pp. 015–023, Jan. 2008.

[Par09] J.M. Park, A.T. Evans, K. Rasmussen, T.R. Brosten, G.F. Nellis, S.A. Klein, Y. B. Gianchandani, "A microvalve with integrated sensors and customization normal state for low-temperature environment," *J. Microelectromech. Syst*. vol.18, no. 4, pp. 868–877, Aug. 2009.

[Pop09] S. Popiel, Z. Witkiewicz, "Chemical warfare agents: GC analysis," In *Encyclopedia of Chromatography*, *3rd Edition*., CRC Press, 2009.

[Pot05] J. A. Potkay and K. D. Wise, "An electrostatically latching thermopneumatic microvalve with closed-loop position sensing," *18th IEEE International Conference on Micro Electro Mechanical Systems*, pp. 415–18, 2005.

[Pot12] J. A. Potkay and K. D. Wise, "A hybrid thermopneumatic and electrostatic microvalve with integrated position sensing," *Micromachines*, vol. 3, no. 2, pp. 379–395, 2012.

[Pri16] P. J. Pritchard, W. M. John, and C. L. John, *Fox and McDonald's Introduction to Fluid Mechanics (Chapter 8), 9th Version*, John Wiley & Sons, 2016.

[Qin14a] Y. Qin and Y. B. Gianchandani, "*iGC1*: An Integrated Fluidic System for Gas Preconcentrator, Column, and Detector Microfabricated by a Three-Mask Process," *J. Microelectromech. Syst*. vol. 23, no. 4, pp. 980-90, 2014.

[Qin14b] Y. Qin and Y. B. Gianchandani, "*iGC2*: An architecture for micro gas chromatographs utilizing integrated bi-directional pumps and multi-stage preconcentrators," *J. Micromech. Microeng*. vol. 24, no. 6, p. 065011 (10 pp.) 2014.

[Qin15a] Y. Qin, S. An, and Y. B. Gianchandani, "Arrayed architectures for multi-stage Si-micromachined high-flow Knudsen pumps," *J. Micromech. Microeng*., vol. 25, no. 11, Oct., 2015.

[Qin15b] Y. Qin and Y. B. Gianchandani, "An All Electronic, Fully Microfabricated Micro Gas Chromatograph," *IEEE International Conference on Solid-State Sensors, Actuators and Microsystems (Transducers)*, Anchorage, AK, June 21–25, 2015. pp. 626–629.

[Qin16] Y. Qin and Y. B. Gianchandani, "A fully electronic microfabricated gas chromatograph with complementary capacitive detectors for indoor pollutants," *Microsystems Nanoeng.*, vol. 2, p. 15049, 2016.

[Rad08] A. D. Radadia, R. I. Masel, M.A. Shannon, J.P. Jerrell, K.R. Cadwallader, "Micromachined GC columns for fast separation of organophosphonate and organosulfur compounds," *Anal. Chem*, vol. 80, pp. 4087-4094, 2008.

[Red13] K. Reddy, J. Liu, M. K. K. Oo, X. Fan, " Integrated separation columns and Fabry-Perot sensors for microgas chromatography systems," *Journal of Microelectromechanical Systems*, vol. 22, no. 5, pp. 1174-1179, 2013.

[Reg18] B.P. Regmi, M. Agah, “Micro gas chromatography: an overview of critical components and their integration,” *Analytical Chemistry*, vol. 90, pp. 13113-13150, 2018.

[Ric03] C. A. Rich and K. D. Wise, "A high-flow thermopneumatic microvalve with improved efficiency and integrated state sensing," *J. Microelectromech. Syst*, vol. 12, no. 2, pp. 201-208, April 2003.

[Rob03] D. C. Roberts, H. Li, J. L. Steyn, O. Yaglioglu, S. M. Spearing, M. A. Schmidt, N. W. Hagood, "A Piezoelectric Microvalve for Compact High-Frequency, High-Differential Pressure Hydraulic Micropumping Systems" *J. Microelectromech. Syst*. vol. 12, no. 1, pp. 81–92, Feb. 2003.

[Rob94] J. K. Robertson and K. D. Wise, "A nested electrostatically-actuated microvalve for an integrated microflow controller," *Proceedings IEEE Micro Electro Mechanical Systems An Investigation of Micro Structures, Sensors, Actuators, Machines and Robotic Systems*, Oiso, Japan, 1994, pp. 7–12.

[Rob98] J. K. Robertson, K. D. Wise, "A low pressure micromachined flow modulator," *Sensors and Actuators A: Physical,* vol. 71, no. 1–2, pp. 98–106, Nov. 1998.

[San03] J. M. Sanchez, R. D. Sacks, "GC Analysis of Human Breath with A Series-Coupled Column Ensemble and A Multibed Sorption Trap," *Anal. Chem*. vol. 75, no. 10, pp. 2231–2236, 2003.

[San16] A. Sandoughsaz, K. Najafi and L. P. Bernal, "A 2kPa per stage and 1.3sccm flow rate modular two-stage electrostatic gas micropump with stiffened drive electrodes," *2016 IEEE SENSORS*, Orlando, FL, 2016, pp. 1-3.

[Sat94] K. Sato and M. Shikida, "An electrostatically actuated gas valve with an S-shaped film element," *Journal of Micromechanics and Microengineering*, vol. 4, n. 4, pp. 205–9, 1994.

[See07] J. V. Seeley, N. J. Micyus, S. V. Bandurski, S. K. Seeley, J. D. McCurry, "Microfluidic Deans Switch for Comprehensive Two-Dimensional Gas Chromatography," *Anal. Chem*. vol. 79, no. 5, pp. 1840–1847, 2007.

[Seo12] J. H. Seo, S. K. Kim, E. T. Zellers, and K. Kurabayashi, "Microfabricated passive vapor preconcentrator/injector designed for microscale gas chromatography," *Lab on a Chip,* vol. 12, no. 4, pp. 717-724, 2012.

[Shi97] Y. Shinozawa, T. Abe, T. Kondo, "A proportional microvalve using a bi-stable magnetic actuator," *in Proc. IEEE 10th Annu. Int. Workshop Micro Electro Mech. Syst.—An Investigation of Micro Structures, Sensors, Actuators, Machines and Robots*, Jan. 26–30, 1997, pp. 233–237.

[Sho91] S. Shoji, B. V. D. Schoot, N. D. Rooij, and M. Esashi, "Smallest dead volume microvalves for integrated chemical analyzing systems" *in IEEE Int. Conf. on Solid-State Sensors and Actuators (Transducers '91)*, San Francisco, CA, USA, 24–27 June. 1991. pp 1052–5.

[Ste11] W. H. Steinecker, S. K. Kim, F. I. Bohrer, L. Farina, C. Kurdak, and E. T. Zellers, "Electron-Beam Patterned Monolayer-Protected Gold Nanoparticle Interface Layers on a Chemiresistor Vapor Sensor Array," *IEEE Sensors Journal,* vol. 11, no. 2, pp. 469-80, 2011.

[Sub06] B. G. Subramani and P. R. Selvaganapathy, "A versatile microreactor platform featuring a chemical-resistant microvalve," *J. Micromech. Microeng.* vol. 16, no. 8, pp. 1433-1443, Aug. 2006.

[Suk11] T. Sukaew, H. Chang, G. Serranoab, E. T. Zellers, "Multi-stage preconcentrator/focuser module designed to enable trace level determinations of trichloroethylene in indoor air with a microfabricated gas chromatograph," *Analyst,* vol. 136, pp. 1664, 2011

[Ter79] S. C. Terry, J. H. Herman, and J. B. Angell, "A Gas Chromatographic Air Analyzer Fabricated on a Silicon Wafer," *IEEE Trans. Electron Devices*, vol. 26, no. 12, pp. 1880–1886, 1979.

[Tia05] W.-C. Tian, H. K. L. Chan, C.-J. Lu, S. W. Pang, and E. T. Zellers, "Multiple-stage microfabricated preconcentrator-focuser for micro gas chromatography system," *Journal of Microelectromechanical Systems,* vol. 14, no. 3, pp. 498-507, 2005.

[Tic13] J. D. Tice, J. B. Rosheck, C. D. Hamlin, C. A. Apblett and P. J. A. Kenis, "Normally-Closed Electrostatic Microvalve Fabricated Using Exclusively Soft-Lithographic Techniques and Operated With Portable Electronics," *J. Microelectromech. Syst.*, vol. 22, no. 6, pp. 1251–1253, Dec. 2013.

[Tic14] J. D. Tice, A. V. Desai, T. A. Bassett, C. A. Apblett, J. A. Kenis, "Control of pressure-driven components in integrated micro fluidic devices using an on-chip electrostatic microvalve," *RSC Adv*. vol. 4, no. 93, pp. 51593–51602, 2014.

[Wan05] J. Wang, Z. Chen, M. Mauk, K.-S. Hong, M. Li, S. Yang, H.H. Bau, "Self-actuated, thermo-responsive hydrogel valves for lab on a chip," *Biomed. Microdevices* 2005, 7, pp. 313–322.

[Wan18] J. Wang, J. Bryant-Genevier, N. Nuñovero, C. Zhang, B. Kraay, C. Zhan, K. Scholten, R. Nidetz, S. Buggaveeti, E.T. Zellers, "Compact prototype microfabricated gas chromatographic analyzer for autonomous determinations of VOC mixtures at typical workplace concentrations," *Microsystems & Nanoengineering*, vol. 4, no. 17101, 2018.

[Yan04] X. Yang, A. Holke, S. A. Jacobson, J. H. Lang, M. A. Schmidt, S.D. Umans, "An Electrostatic, On/Off Microvalve Designed for Gas Fuel Delivery for the MIT Microengine," *J. Microelectromech. Syst*. vol. 13, no. 4, pp. 660-668, Aug. 2004.

[Zam09] S. Zampolli, I. Elmi, F. Mancarella, P. Betti, E.Dalcanale, G. C. Cardinali, M. Severi, "Real-time monitoring of sub-ppb concentrations of aromatic volatiles with a MEMS-enabled miniaturized gas-chromatograph," *Sensors and Actuators B: Chemical,* vol. 141, no. 1, pp. 322–328, 2009.

[Zha19] C. Zhan, M. Akbar, R. Hower, J. Wang, N. Nuñovero, J.A. Potkay, E.T. Zellers, "Integrated multi-vapor microcollector-injector (μCOIN) for μGC," *IEEE International Conference on Solid-State Sensors*, *Actuators and Microsystems (Transducers)*, Berlin Germany, Jun. 2019, pp. 29-32.

[Zho16] M. Zhou, J. Lee, H. Zhu, R. Nidetz, K. Kurabayashi, X. Fan, "A fully automated portable gas chromatography system for sensitive and rapid quantification of volatile organic compounds in water," *RSC Adv*., vol. 6, pp. 49416, 2016.